COMMUNICATIONS

Dear readers,

This issue of the Communications – Scientific Letters of the University of Zilina is mainly devoted to materials engineering.

Materials are one of the most perspective areas of scientific exploration in the 21st century. There is observation of relationships between structure, technology, properties and optimal usage of materials. The aims are the machine components and equipment with high technical parameters including requirements of high reliability, safety and endurance.

Trend growth of all technical discipline is dependent on development of materials. The prestige experimental workplaces of universities and research institutions, both national and international, deal with material research.

The editorial board addressed the institutions whose activities on the material research are significant. Let me thank all of them (Charles University Prague, Czech Technical University of Prague, SVUM, a. s., Prague, Brno University of Technology, University of Defence, Brno, Slovak University of Technology of Trnava, VSB – Technical University of Ostrava, Technical University of Kosice, University of Zilina) who contributed to the Communications – Scientific Letters of the University of Zilina, No. 1, 2009.

Otakar Bokuvka

Pavel Lukac – Zuzanka Trojanova *

DEFORMATION BEHAVIOUR OF MG-BASED MATRIX COMPOSITES

The influence of various reinforcements on mechanical properties and deformation behaviour of some magnesium alloys was studied. Strength and deformation behaviour were investigated over a wide temperature range. The reinforcement was in the form of short fibres or particles. The volume fraction of the reinforcement significantly influences the properties of a composite. The interface between the matrix and the reinforcement has a great deal of importance in determining the properties of the composite. Thermal stresses generated at the interface play a very important role.

1. Introduction

Magnesium, the lightest structural metallic element, and its alloys possess a great potential to be developed as structural materials provided that significant improvements in properties are achieved. Coarse grained Mg materials have some limitations such as low strength, low ductility and poor corrosion resistance. It can be shown that grain size refinement is an effective method for improving the strength of materials. According to the Hall-Petch relationship, magnesium alloys with ultrafine grains have high specific strength and specific stiffness. Grain refinement leads, in some cases, to a higher ductility of the magnesium alloys. On the other hand, Mg alloys exhibit poor plastic formability due to their hexagonal close packed structure.

Reinforcement of an alloy leads also to an increase in strength [1]. Magnesium alloys are attractive candidates for reinforcement with short ceramic fibres or particles. Reinforcement allows adapting more exactly the work piece material properties to requirements. Therefore, there is an increasing trend in industry branches to use the metallic matrix composites (MMC) for various parts. Thermal residual stresses are formed in MMCs due to differences in the coefficients of thermal expansion between the matrix and the reinforcement. The matrix/reinforcement interface is significant in determining mechanical properties. In general, composite properties strongly depend on the properties of the composite components. The interface region is the region where a discontinuity in some material parameters occurs.

The aim of this paper is to show the influence of temperature on the strength and deformation behaviour of some magnesium based MMCs.

2. Experimental procedure

The investigated AZ91 magnesium alloy reinforced with δ-Al_2O_3 short fibres (Saffil® with a mean diameter of 3 μm and a mean length about 87 μm) was prepared by squeeze casting technology. The preforms consisting of Al_2O_3 short fibres showing a planar isotropic distribution and a binder system (containing Al_2O_3 and starch) were preheated to a temperature (about 1000 °C) higher than the melt temperature of magnesium and then inserted into preheated die (290 to 360 °C). The pressure for forcing the melt into the die with the preform was applied in two steps (e.g. 50 MPa for 10 s and 130 MPa for 60 s; the values of the pressure depend on the alloy used). The second step closes pores and shrinkage cavities. During this short time of contact between the liquid metal and the fibres, only a slight reaction between the fibres and the matrix can occur.

The WE54 alloy reinforced with SiC particles (a volume fraction of 13%) was processed by a powder metallurgy method. Mixing of the matrix powders with various SiC particles was carried out first in an asymmetrically moved mixer with subsequent milling in a ball mill. The powder was capsulated in magnesium containers and extruded at 400 °C using a 400 t horizontal extrusion press. The composite samples were not thermally treated. The mean SiC particle size was found to be about 9 μm. The as-extruded bar appeared mainly constituted of very small equiaxed grains (about 3 μm) after accurate optical microscopy observations. No grain growth was observed during the deformation tests at elevated temperatures.

The mechanical properties of the composites were assessed through compression tests at temperatures between 20 and 300 °C.

* **Pavel Lukac, Zuzanka Trojanova**
Charles University, Department of Physics of Materials, Prague, Czech Republic,
E-mail: lukac@met.mff.cuni.cz

The specimens with dimensions 5×5×10 mm^3 were deformed using an Instron testing machine at a constant crosshead speed giving an initial strain rate $2.7x10^{-4}$ s^{-1}.

3. Experimental results and discussion

Short fibres in the composites were randomly arranged (a 2D random orientation), i.e. axes of the fibres lay in parallel planes. Specimens of AZ91 alloys reinforced with 23 vol.% short Saffil fibres were prepared with both the fibre planes parallel to and perpendicular to the specimen axis. The temperature dependences of the yield stress of both monolithic AZ91alloy and reinforced with 23 vol. % Saffil fibres with both fibre planes orientations are given in Fig. 1. The maximum stress for the same specimens as a function of the test temperature is given in Fig. 2.

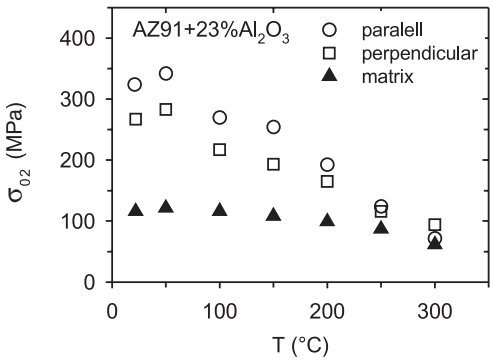

Fig. 1 Temperature dependence of yield stress for AZ91 and AZ91+Al_2O_3

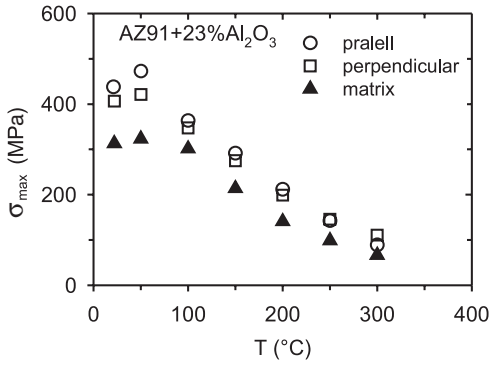

Fig. 2 Temperature dependence of maximum stress for AZ91 and AZ91+Al_2O_3

The yield stress and the maximum stress decrease very rapidly with increasing temperature. At and above 250 °C the values of the yield stress for the composite are very close to those for the monolithic alloy (matrix). It is clear the yield stress of the AZ91 composite at lower temperatures (below 200 °C) is higher than that of unreinforced alloy. The difference between the yield stress of the composite and that of monolithic alloy at room temperature is more than 200 MPa. On the other hand, the values of the maximum stress for the composites are very close to those for the unreinforced alloy. This may indicate that fibres influence significantly the yield and that dislocation motion is more important for strain hardening. It should be mentioned that the difference between the maximum stress and yield stress decreases with increasing temperature. This indicates a softening process at higher temperatures. The temperature dependences of the characteristic stresses of WE54+SiC composite, the yield stress σ_{02} and the maximum stress σ_{max}, are shown in Fig. 3.

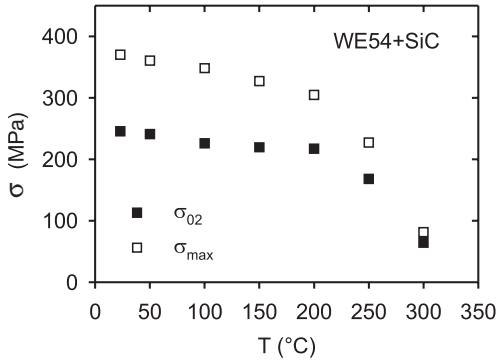

Fig. 3 Temperature dependence of yield stress and maximum stress for WE54+SiC

The influence of the temperature on strain hardening of the composite is well visible. The yield stress decreases with increasing temperature very slowly up to 200 °C, while the observed decrease of the maximum stress σmax is more rapid. For temperatures higher than 200 °C both stresses decrease substantially. It can be concluded that the thermal stability of the composite is very good up to 200 °C. TEM micrograph of the non-deformed WE54+SiC composite sample is shown in Fig. 4.

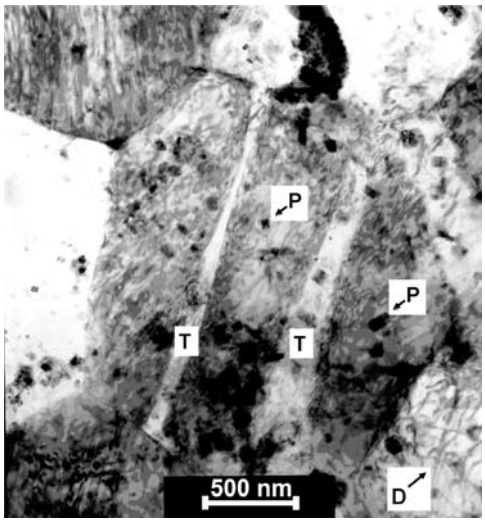

Fig. 4 TEM micrograph of WE54+SiC composite

TEM investigation revealed the presence of many twins (T) and precipitates (P). Tangled dislocations (D) in the right bottom corner are visible. The presence of twins is a common feature for both non-deformed as well as deformed composites. Grains in the as-received material are well visible in Fig. 4. Thin twins, within single grains, are parallel to each other and are quite narrow. Sometimes twins are extended trough the grain boundary, causing a grain boundary deflection.

It can be seen that addition of the reinforcing phase substantially increases the yield stress. Generally, fibres in the matrix act as obstacles for dislocation motion in the slip plane. Accordingly, the stress necessary for plastic deformation of composites should be higher than in the unreinforced matrix. The load transfer and enhanced dislocation density should be considered as significant factors influencing the value of the yield stress.

3.1. Yield stress

The load transfer from matrix to fibre is maintained by the interface. According to the shear lag theory the load transfer occurs between reinforcement with a high aspect ratio and the matrix by means of the shear stress at the fibre-matrix interface. In this mechanism, the fibre can act as a "reinforcement" to carry some of the load. A contribution to the yield stress due to load transfer $\Delta\sigma_{LT}$ is given, according to shear lag model [2], as

$$\Delta\sigma_{LT} = \sigma_m\left[1 + \frac{(L+t)A}{4L}\right]f + \sigma_m(1-f) \tag{1}$$

where σ_m is the yield stress of the matrix, L is the fibre size in the applied stress direction, t is the fibre size in the perpendicular direction and A is the fibre aspect ratio (L/t). For equiaxial particles, an increase in the yield stress due to load transfer $\Delta\sigma_{LT}$ may be given by

$$\Delta\sigma_{LT} = \sigma_m 0.5f \tag{2}$$

The strengthening component $\Delta\sigma_{LT}$, depends on the reinforcement volume fraction.

The strengthening component $\Delta\sigma_{LT}$ in AZ91 – 23 vol. % Saffil fibres, arising from the load transfer form matrix to fibres, has a value of 180 MPa in the case when all fibres are aligned in the specimen axis. Calculating the strength increase of 2D randomly oriented short fibres, one becomes $\Delta\sigma_{LT} = 108$ MPa.

Typically, there is a large difference in the values of thermal expansion coefficients (CTE) between the matrix and the fibres. During the fabrication process of a composite and/or during heat treatment, thermal stresses are generated owing to different thermal expansion of the matrix and the reinforcement. For a composite with short fibres, the thermal stresses σ_{TS} generated at the vicinity of the matrix-reinforcement interface can be calculated as [3, 4]

$$\sigma_{TS} = E_f E_M f\Delta\alpha\Delta T/[E_f f + E_M(1-f)]. \tag{3}$$

Here E_f and E_M are the values of Young's modulus for the fibres and the matrix, respectively, f is the volume fraction of fibres, $\Delta\alpha$ is the difference of the CTE values and ΔT is the temperature change from the free-stress state. With increasing distance from the fibres, the thermal stress is lower because it decreases with the distance r as $1/r^3$. Volume-averaged residual stresses reach in the matrix their maximum value [5]

$$\sigma_{m\max} = \frac{2}{3}\sigma_y \ln\left(\frac{1}{f}\right)\frac{f}{1-f}, \tag{4}$$

where σy is the yield stress in the matrix. The thermal stresses in the matrix may exceed the yield stress. Then plastic deformation occurs without any applied stress and new dislocations are formed at the interfaces. The dislocation density in the vicinity of the interfaces was found to be significantly higher than that elsewhere in the matrix. Plastic zones containing tangled dislocations generally result along the fibres [6]. The density of the newly created dislocations, $\Delta\rho$, is given as [4, 7]

$$\Delta\rho = \frac{Bf\Delta\alpha\Delta T}{b(1-f)}\frac{1}{t_f} \tag{5}$$

where t_f is the minimum size of the reinforcing phase, b is the magnitude of the Burgers vector of dislocations and B is a geometrical constant depending on the reinforcement shape.

The generation of thermally induced dislocations and the related dislocations density gradients increase also the yield stress of the composite. A contribution to the yield stress due to the increase in the dislocation density may be expressed as

$$\sigma_{CTE} = \alpha_1 \psi G b\left(\frac{Bf\Delta\alpha\Delta T}{(1-f)bt_f}\right)^{\frac{1}{2}}, \tag{6}$$

where α_1 is a constant, G the shear modulus and ψ is the Taylor factor. The density of the new dislocations formed during preparation process is approximately $\Delta\rho = 1.87\times1013\ \mathrm{m}^{-2}$ (if $B = 10$, $\Delta\alpha = 20\times10^{-6}\ \mathrm{K}^{-1}$). The stress contribution at room temperature $\Delta\sigma_{CTE}$ is about 49 MPa, if using (6) and taking $\alpha_1 = 0.35$ and Taylor factor $\psi = 6$ [8].

As another mechanism contributing to the yield stress one should consider the generation of geometrically necessary dislocations [9], the density of which is, in the yield stress vicinity, about $3.8\times1.012\ \mathrm{m}^{-2}$. The corresponding stress increase is about 22 MPa. Very probably this mechanism is not significant at the yield stress but the density of the geometrically necessary dislocations increases with increasing strain. However, it is important to note that the discontinuously reinforced composites (with particles) have very fine grains; smaller than their unreinforced matrixes. The contribution to the yield stress due to this effect can then be estimated using the Hall-Petch relation.

Fibres or particles in the matrix are obstacles for dislocation motion. Therefore, the stress necessary for the motion of dislocations in the composite is higher than in the matrix without fibres.

We may consider a similar mechanism as in the case of strengthening by incoherent particles, i.e. Orowan strengthening. It is caused by the resistance of closely spaced hard fibres to the passing of dislocations. Asides from fibres, dislocations overcome stresses from dislocation pile-ups in the vicinity of the fibres. For strengthening caused by this mechanism, one may use to the following equation [10]

$$\Delta\sigma_{OR} = \frac{Gb}{\Lambda} + \frac{5}{2\pi} Gf\varepsilon_p \qquad (7)$$

where Λ is the distance between fibres and ε_p is plastic deformation. It is widely accepted that Orowan strengthening is not significant for metal matrix composites because the reinforcements are coarse and the interfibre spacing is large. An increase of the yield stress due to the Orowan mechanisms is only some units of MPa.

The value obtained when all the contributions due to the presence of fibres are added to the yield stress of the matrix is very close to the yield stress of the composite observed experimentally. The sum of all individual contributions to strengthening for AZ91 composite with the parallel orientation of fibres gives 329 MPa, which is in good agreement with the experimental value for the parallel composite of 324 MPa. The main contributions to strengthening are the load transfer and increased dislocation density. Different situation is in the case of WE54+SiC composite. The main contribution to the strengthening is the small grain of the powder metallurgical material i.e. the Hall-Petch strengthening. The equiaxial relatively big particles contribute only lightly to the load transfer and the increased dislocation density. For the yield stress of the WE54+SiC composite at room temperature one obtains 278 MPa as compared to the experimental value of 246 MPa.

3.2. Strain hardening

The testing temperature affects the shape of the stress-strain curves of Mg based composites. The strain hardening rapidly decreases with temperature. At high temperatures (above about 200 – 250 °C), a steady state flow (little or no hardening) is attained after small strains. The elongation to fracture of composites increases with increasing temperature. But the composites exhibit lower ductility in comparison to monolithic alloys. The values of the elongation to fracture of the composites are almost an order of magnitude lower that those of the alloys. The lower ductility of composites can be attributed to void nucleation at the matrix-fibre interfaces.

The strain hardening rate is determined by the hardening and softening processes occurring during straining. Plastic deformation is a result of the movement, multiplication and annihilation of dislocations. The main obstacles for glide of dislocations are solute atoms, precipitates, grain boundaries, fibres and dislocations. Plastic zones are formed around fibres (particles). The dislocation density in the vicinity of fibres is higher than elsewhere in the matrix. Moving dislocations cannot pass through the fibres. Dislocation pile-ups are formed at fibres and grain boundaries and they can act as stress concentrators. A reduction of the free path of dislocations leads to hardening. On the other hand, the dislocation pile-ups (as stress concentrators) make possible that screw dislocation components may locally cross slip and after the cross slip, annihilation of dislocations may occur. With an increase in the testing temperature, double cross slip is easier leading to a decrease in the strain hardening rate and to an increase in the elongation to fracture, which is in agreement with experimental results. At higher temperatures the coarsening of precipitates may occur during the test. This leads to a reduction to the stress for the dislocation motion and therefore, to a decrease in the strain hardening rate. Annihilation of dislocation is the main softening mechanism.

The primary (dominant) deformation mechanism in Mg alloys is the basal slip. However, five independent slip systems are required for homogeneous deformation of polycrystals [11]. Hence, the activity of non-basal slip systems is required. For magnesium and its alloys, the critical resolved shear stresses (CRSS) of non-basal slip systems are much higher than for basal slip system at room temperature. The CRSS for non-basal slip systems decrease very rapidly with increasing temperature. It means the activity of non-basal slip systems increases with increasing temperature. In magnesium and its alloys, the glide of <*c* + *a*> dislocations in second-order pyramidal slip system is expected [12, 13]. Intensive activity of non-basal slip systems with <*c* + *a*> dislocations at higher temperatures provides explanation for the observed decrease of the flow stress and of strain hardening rate. During deformation the motion of dislocations in both the basal and the non-basal slip systems is assumed. The activity of the non-basal slip system increases with increasing temperature. The interaction between basal and non-basal dislocations may result to new obstacles or annihilation depending on the dislocation reaction. Dislocation reactions may produce sessile dislocation and an increase in the density of the forest dislocations. Then, additional obstacles for the dislocation movement are formed, which causes hardening. With increasing temperature, <*a*> dislocations may cross slip from the basal slip system through prismatic or first-order pyramidal planes to parallel basal planes, which causes an increase in the free path of dislocations and therefore softening. Screw components of <*c* + *a*> dislocations can also move to the parallel slip planes by double cross slip. Annihilation of dislocations can follow after cross slip. It means the density of dislocations decreases, the work hardening rate decreases and softening occurs. It is clear that both the glide of <*c* + *a*> dislocations on the second-order pyramidal slip planes and cross slip of <*a*> and <*c* + *a*> dislocation types are strongly thermally activated.

The observed increase in the elongation to fracture with increasing temperature may be also explained by increasing activity of non-basal slip systems with increasing temperature.

4. Conclusions

Ceramics fibres and particles influence significantly mechanical properties of composites with the AZ91 and WE54 matrix. Contribution of short fibres to strengthening of the composite is

higher than particles. This reinforcing phases impact decreases with increasing temperature. The main hardening mechanism in the AZ91 composite is probably the load transfer in which the part of the external load within the matrix is transferred to reinforcement. An increase in the dislocation density and residual thermal stresses play also important role.

The most important contributions to the yield stress in WE54+SiC composite are the small grain size of the matrix alloy and the stress increase due to precipitation hardening in the matrix. The reinforcing phase contributes to strengthening mainly through an increased dislocation density (arising from the thermal and geometrical mismatch). The load transfer from matrix to reinforcing particulates plays in this composite only a marginal role.

The test temperature influences significantly the deformation behaviour of Mg-based composites. The yield strength and the maximum flow stress decrease very rapidly with increasing temperature. The difference between the maximum flow stress and the yield stress decreases with increasing temperature. Therefore, the work hardening rate decreases also with an increase in the test temperature. From the dislocation theory point of view, it means that at higher temperatures there is a dynamic balance between hardening and softening processes. Hardening is a result of storage of dislocations and softening is caused by annihilation of dislocations. The activity of non-basal slip systems plays an important role in the deformation behaviour of magnesium based composites. The glide of $\langle c + a \rangle$ dislocations on the second order pyramidal slip planes and double cross slip of both $\langle a \rangle$ and $\langle c + a \rangle$ dislocations affect significantly the deformation behaviour of magnesium based composites.

Acknowledgements

The authors acknowledge financial support of the Grant Agency of the Czech Republic under grant 106/06/1354. The authors are grateful also for the support offered by the Czech and Slovak authorities under the Exchange Programme MEB 0808116.

References

[1] CLYNE, T.W, WITHERS, P.J.: *An Introduction to Metal Matrix Composites*, Cambridge, Cambridge Univ, Press 1993.
[2] AIKIN Jr, R.M., CHRISTODOULOU, L.: *Scripta Metall.* Mater., Vol. 25, 1991, p. 9.
[3] CHAWLA, K.K.: In: *Materials Science and Technology*, Vol. 13, Eds. Cahn R.W., Haasen P., Kramer E.J., Weinheim: VCH, 1993.
[4] URRETA, S.E., SCHALLER, R., CARENO-MORELLI, E., GABELLA, E.J.: *Physique IV*, 1996, p. C8-774.
[5] DELANNAY. F.: In: *Comprehensive Composite Materials*, Vol. 3, Ed. Clyne, T.W. Amsterdam, Elsevier, 2000, p. 341.
[6] DUNAND, D.C., MORTENSEN, A.: *Acta Metall.* Mater., Vol. 39, 1991, p. 127.
[7] ARSENAULT, J.R., SHI, N.: *Mater. Sci. Eng*., Vol. 81, 1986, p. 151.
[8] ARMSTRONG, R.W.: *Acta Metall.*, Vol. 16, 1968, p. 347.
[9] ASHBY. M.F.: *Phil. Mag.*, Vol. 21, 1970, p. 399.
[10] SCATTERGOOD. R.O., BACON. D.: *Phil. Mag.* A, Vol. 31, 1975, p. 179.
[11] TAYLOR, G.I: *J. Inst. Met.*, Vol. 62, 1938, p. 307.
[12] LUKAC, P.: *Czech. J. Phys. B,* Vol. 31, 1981, p. 135.
[13] BALIK, J., LUKAC, P., BOHLEN, J., KAINER, K.U.: *Metallic Materials,* Bratislava, Vol. 45, 2007, p. 135.

Z. Trojanova – Z. Szaraz – V. Gartnerova *

EFFECT OF SHORT SAFFIL FIBRES AND SiC PARTICLES ON MECHANICAL PROPERTIES OF MAGNESIUM ALLOYS

The high temperature mechanical behaviour of composites with the AZ91 and AS21 magnesium alloys matrix, reinforced with short Saffil fibres and SiC particles were investigated. Samples were deformed in compression in the temperature range from room temperature to 300 °C. The yield stress and the maximum stress of true stress-true strain curves decrease with increasing temperature. Light and electron microscopy were used for study of the microstructure of composites. Possible hardening and softening mechanisms are discussed. The increased dislocation density and the shear stress at reinforcing phase/matrix interfaces were found as the most important contributions to the strengthening.

Keywords: Magnesium alloys; Composites; Mechanical properties; Strengthening; Interface; Dislocation motion

1. Introduction

Several magnesium-based metal matrix composites (MMCs) have been developed over the last decade for potential use as lightweight high-performance materials [1]. It is well established that the microstructures and the mechanical properties of MMCs are strongly affected by the nature of the interfaces between the matrix and the reinforcement. Strengthening in metals and alloys reinforced by fibres or particles were analysed in many papers with the aim to find the correlation between mechanical properties and microstructural characteristics of composites. In spite of many attempts there is no generally accepted model for metal matrix composites strengthening. It is probably due to very complex character of the problem. Many factors and mechanisms play role and synergetic operation of these mechanisms has been not sufficiently studied. Investigations of mechanical and physical properties of MMC (among them magnesium alloys based composites) are important not only for applications but also for better understanding of the processes responsible for their behaviour.

In literature there are three types of models explaining mechanical properties of MMCs. Models resulting from the continuum mechanics are either numerical, typically finite element, models, or analytical effective medium schemes (for example [2–6]). Dislocation approach has a possibility to predict the interaction of individual dislocations with stress fields, solute atoms, and precipitates, grain boundaries and reinforcing phase fibres or particles. Continuum plasticity ignores the details of slip on an atomic level and uses constitutive equations to relate stress and strain (or strain rate) in the matrix. The properties of the reinforcing phase influence dislocation behaviour and the mechanical properties of composites. While the intrinsic mechanical and physical properties of the reinforcement (stiffness, strength, and thermal expansion) are dictated by its chemical nature, the geometric and topological parameters of the reinforcement (shape, size, volume fraction, spatial orientation, and distribution) can be altered during processing. Trojanová et al. [7] discussed various strengthening mechanisms in Mg alloys reinforced by short Saffil fibres. The most important contributions were found to be the load transfer from the matrix to the fibres and the influence of the increased dislocation density arising from internal thermal stresses. Other possible mechanisms do not influence the level of deformation stresses in a significant manner.

The objectives of the present paper are to study the deformation behaviour of the AZ91 and AS21 magnesium alloys based hybrid composites and to discuss possible contribution of Saffil ceramic fibres and SiC particles to strengthening as well as softening of these materials.

2. Experimental procedures

Commercial AZ91 (9Al-1-Zn-0.1Mn-balance Mg) and AS21 (2.2Al-1Si-0.1Mn-balance Mg-in wt%) alloy were used as the matrix material. The alloys were reinforced with δ-Al_2O_3 short fibres (Saffil) and equiaxial SiC particles. The preforms consisting of Al_2O_3 short fibres showing a planar isotropic fibre distribution, SiC particles and a binder system (containing Al_2O_3 and starch) were preheated to a temperature higher than the melt temperature of alloy and then inserted into a preheated die. The two-stage application of the pressure resulted in MMCs with a fibre volume fraction from approximately 5 vol. % of fibres and 15 vol.% of SiC. The mean fibre length and fibre diameter (measured after squeeze

* **Z. Trojanova, Z. Szaraz, V. Gartnerova**
Department of Physics of Materials, Faculty Mathematics and Physics, Charles University Prague, Czech Republic, E-mail: ztrojan@met.mff.cuni.cz

casting) were ~78 μm and ~3 μm, respectively. Sharply shaped SiC particles exhibited size of about 10 μm. Composites with the AZ91 matrix alloy (AZ91h) were thermally treated according to Polmear [8] (413 °C for 18 hours followed by quenching and artificial aging at 168 °C for 8 hours). Samples with AS21 matrix alloy (AS21h) were not thermally treated. Samples for compression tests were machined with dimensions of $5\times5\times10$ mm^3 with the plane of Saffil fibres oriented parallel to the stress axis. Compression tests were carried out in a universal INSTRON testing machine in displacement control at a nominal strain rate of 8.3×10^{-5} s^{-1} (AZ91h) and 2.7×10^{-4} s^{-1} (AS21h) at temperatures between room temperature and 300 °C. The temperature in the furnace was kept with an accuracy of ±1°C. The yield strength of the composites was determined by an offset method at 0.2% (σ_{02}) plastic strain. Sections of composite castings were polished and examined by the light microscope Olympus and substructure of composites by the transmission electron microscopy (TEM).

3. Results

Fig. 1 shows a microstructure of AZ91h composite after T6 heat treatment. The observed structure consists of solid solution of aluminium in magnesium (δ-phase), electron compound $Al_{12}Mg_{17}$ (γ-phase) and discontinuous precipitate (lamellae of γ+δ phase). Saffil fibres are distributed randomly in the planes parallel to the compression direction. From the micrograph it is to see that SiCp are distributed non-uniformly. Characteristic feature of the AS21 composite microstructure is Mg_2Si phase having a characteristic Chinese-script form [9]. Microstructure of the AS21h is introduced in Figure 2. Saffil fibres as well as SiC particles are visible. It is obvious that SiC particles are not uniformly distributed in the matrix; in many cases they form clusters.

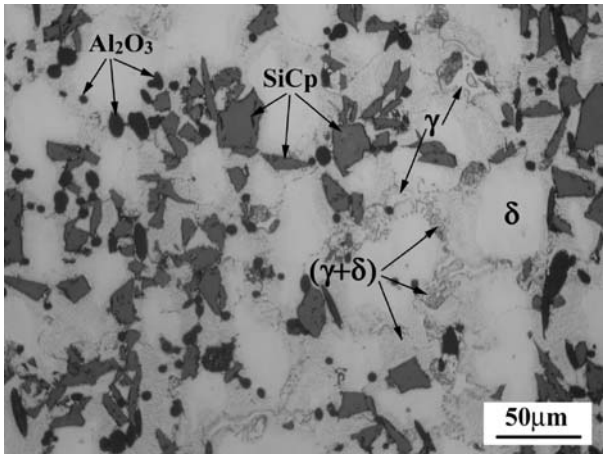

Fig. 1: Representative microstructure of AZ91 hybrid composite.

Fig. 3 shows the true stress-true strain curves obtained for AZ91h composite deformed at various temperatures. Samples were deformed either to fracture or at higher temperatures to predetermined strains. The fracture occurred up to 200 °C, however, at 250 °C and 300 °C the deformation was interrupted at about 0.25

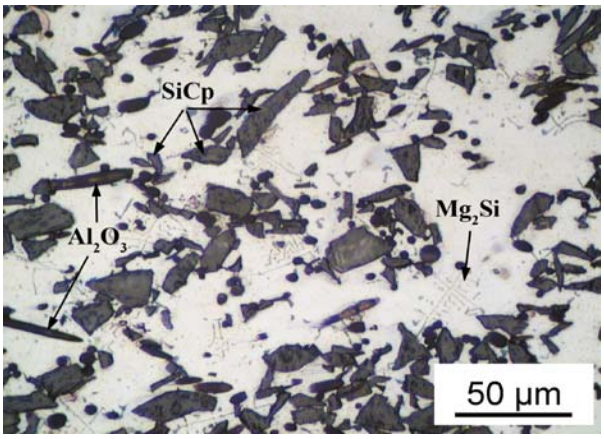

Fig. 2: Microstructure of hybrid composite with Saffil fibres and SiC particles. Small precipitates in the form of Chinese script are visible.

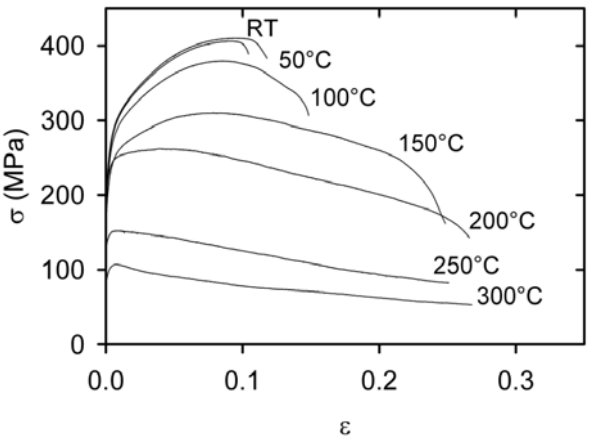

Fig. 3: Stress strain curves obtained for AZ91h and various temperatures.

of true strain. Both characteristic stresses (the yield stress σ_{02} and the maximum stress σ_{max}) are shown in Fig. 4. The yield stress σ_{02}

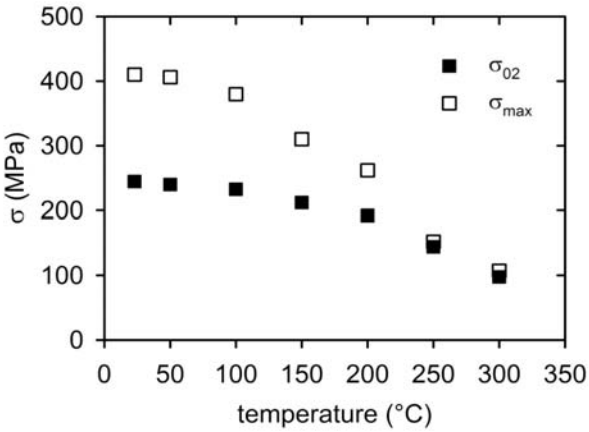

Fig. 4: Temperature dependence of the yield stress and the maximum stress obtained for AZ91h.

decreases slightly with temperature up to 150 °C and then, for higher temperatures the yield stress decreases more rapidly. The measured difference between the yield and maximum stress is at room temperature about 170 MPa and it decreases with increasing temperature to about 10 MPa at 300 °C. The small difference between the yield stress and the maximum stress reflects the flat character of the stress strain curves.

Similar stress-strain curves were obtained for AS21h composite as it as demonstrated in Fig. 5. Significant strain hardening was estimated at temperatures up to 150 °C. At temperatures higher than 150 °C observed curves have a steady state character. Ductility is about 10% at lower temperatures and it increases with increasing temperature. Temperature dependence of the yield stress as well as the maximum stress is introduced in Fig. 6. The yield stress exhibits a local maximum at 50 °C. Such small local maximum in

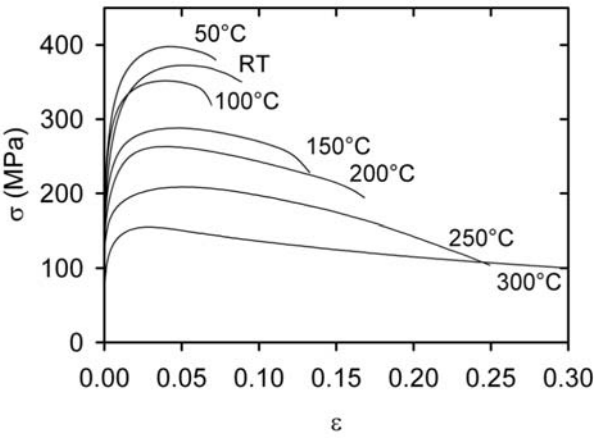

Fig. 5: Stress strain curves obtained for AS21h and various temperatures.

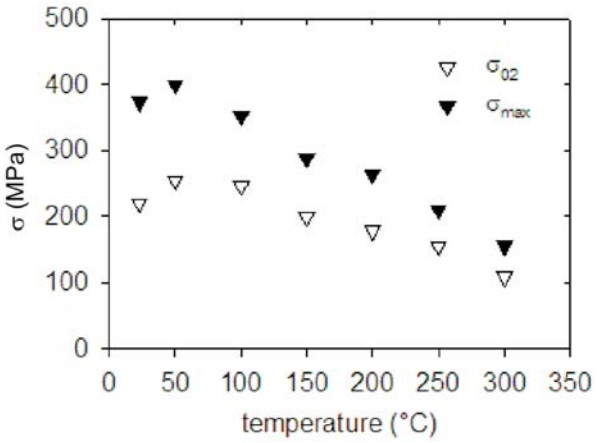

Fig. 6: Temperature dependence of the yield stress and the maximum stress obtained for AS21h.

the temperature dependence of the yield stress was observed also in other magnesium alloys (AZ91, LA45) [10–12]. This local maximum in the temperature dependence of the yield stress is very probably a result of the dynamic strain ageing phenomenon, where mobile solute atoms interact with dislocations.

The influence of the reinforcing phase (fibres and particles) on the yield stress is well apparent from Fig. 7 for AZ91h and in Fig. 8 for AS21h comparing with the unreinforced alloy. From both figures it can be seen the major effect of fibres and particles at room temperature and a decreasing influence of the reinforcing phase at temperatures higher.

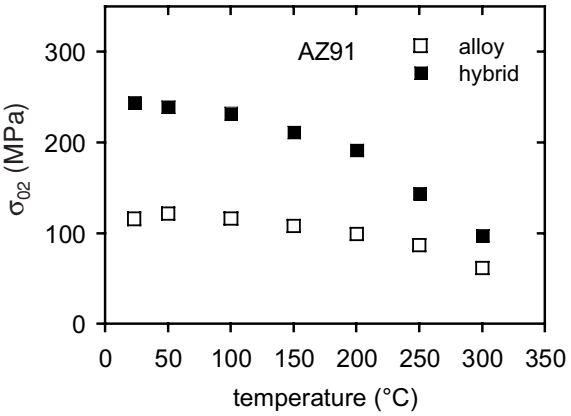

Fig. 7: Comparison of the yield stress of AZ91 composite and alloy.

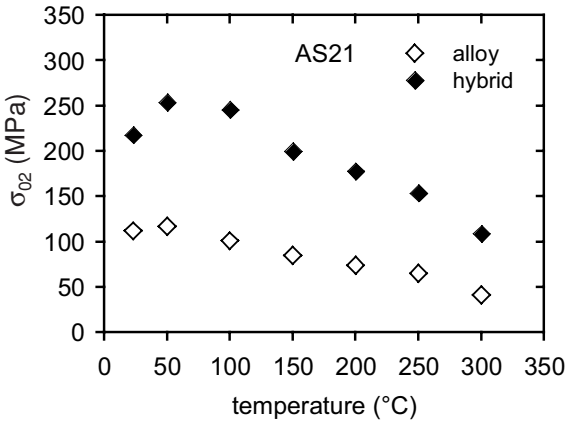

Fig. 8: Comparison of the yield stress of AS21 composite and alloy.

4. Discussion

4.1 Hardening mechanisms

Load transfer

The load transfer from matrix to fibres can be described by the shear lag theory, which assumes that the load transfer occurs between reinforcement and the matrix by means of shear stress at the interface between the reinforcing phase and matrix. According to this mechanism, the fibre can act as a “reinforcement” to carry

some of the load. Several authors [13–16] considered the shear lag model. The flow stress σ_{LT} necessary for composite deformation due to load transfer can be calculated as [17]:

$$\sigma_{LT} = \sigma_m\left[1 + \frac{(L+t)A}{4L}\right]f + \sigma_m(1-f), \quad (1)$$

where σ_m is the stress in the matrix, L is the fibre size in the direction of the applied stress, t is the fibre size in the perpendicular direction, A is the fibre aspect ratio (L/t) and f is the volume fraction of reinforcement (fibres). The model is based on the simplifying assumption of a uniform matrix deformation and therefore, yields a very simplified expression for stiffness and strength contribution. Except the stress transfer from the matrix to the reinforcing phase, fibres or particles, the shear lag model does not account for the contributions from effects, which are associated with the inhomogeneous matrix behaviour, resulting in enhanced dislocation density and residual thermal stresses. For equiaxial particles, an increase in the yield stress due to load transfer $\Delta\sigma_{LT}$ may be given by

$$\Delta\sigma_{LT} = \sigma_m 0.5f\,. \quad (2)$$

The strengthening component $\Delta\sigma_{LT}$, depends on the reinforcement volume fraction f.

Enhanced dislocation density.

Typical large difference between coefficients of thermal expansion (CTE) of the matrix and ceramic reinforcement $\Delta\alpha$ is a very important factor for the deformation behaviour of composites with a metallic matrix. CTE of a ceramic reinforcement is smaller than that of most metallic matrices. When a metal matrix composite is cooled from a higher temperature to room temperature, misfit strains occur because of differential thermal contraction at the interface. These strains induce thermal stresses that may be higher than the yield stress of the matrix. The thermal stresses may be sufficiently high to generate new dislocations at the interfaces between the matrix and the reinforcements. Therefore, after cooling the composite, the dislocation density in the matrix increases. The density of newly generated dislocations, near reinforcement fibres or particles, can be calculated as [18]:

$$\rho_T = \frac{Bf\Delta\alpha\Delta T}{b(1-f)}\frac{1}{t}, \quad (3)$$

where t is a minimum size of the reinforcing phase particles or fibres, b is the magnitude of the Burgers vector of the newly created dislocations, B is a geometrical constant (B=10 for fibres and (B=12 for particles), $\Delta\alpha\Delta T$ is the thermal strain. When the thermal stresses achieve the yield stress, plastic zones can be formed in the matrix near the interfaces, especially, in the vicinity of fibre ends. We assume that the higher dislocation density arises in composites during the fabrication procedure. Increased dislocation density was detected by the internal friction measurements [19] and also directly observed by the means of the TEM [20].

Plastic deformation is generation, movement and storage of dislocations. Dislocations are stored at obstacles arising due to dislocation interaction (statistical dislocations) or they are required for the compatible deformation of various parts of the crystal constrained within its surroundings. These dislocations that are stored due to incompatibility of deformation are dislocations geometrically necessary. The density of dislocations geometrically necessary can be linked to the average strain gradient present in the microstructure and may be expressed as [21]

$$\rho_G = \frac{f8\varepsilon_p}{bt}, \quad (4)$$

where ε_p is plastic strain. In the case of MMCs with the ceramic reinforcing phase, the incompatibility in deformation between the plastically deforming matrix and essentially rigid reinforcement leads to creation of strong strain gradients in the metallic matrix. The influence of the geometrically necessary dislocations increases with increasing strain.

Introducing reinforcing phase into the metal matrix influences not only the densities of the thermally formed and geometrically necessary dislocations, but also the dislocation stored at reinforcements during deformation. Considering these effects, the total dislocation density in composites can be written:

$$\rho_{total} = \rho_T + \rho_G + (\rho_S + \rho_a), \quad (5)$$

where ρ_S is the statistically stored dislocation density in the unreinforced matrix, ρ_a is the diminished part of the statistically stored dislocations due to the addition of reinforcing phase. The strengthening in the matrix alloy is attributed to the deformation resistance induced by the reinforcing phase. According to the Taylor relation, the contribution to the total stress due to the presence of dislocations in the matrix may be written:

$$\Delta\sigma_D = \alpha_1\psi Gb(\rho_T + \rho_G + \rho_S + \rho_a)^{1/2}, \quad (6)$$

where α_1 is a constant, ψ is the Taylor factor and G is the shear modulus. This higher matrix dislocation density as well as the reinforcement/matrix interfaces can provide high diffusivity paths in a composite. The higher dislocation density would also affect the precipitation kinetics in a precipitation hardenable matrix.

Orowan strengthening

The yield stress is characterised by the state when the matrix plastic flow is developed. Fibres in the matrix are obstacles for dislocation motion. Therefore, the stress necessary for motion of dislocations in the composite is higher than in the matrix without fibres. We consider a similar mechanism as in the case of strengthening by incoherent particles, i. e. Orowan strengthening. It is caused by the resistance of closely spaced hard fibres to the passing of dislocations. Asides from fibres, dislocations overcome stresses from dislocation pile-ups in the vicinity of the fibres. For strengthening caused by this mechanism, one may use the expression as a first approximation [22]

$$\Delta\sigma_{OR} = \left(\frac{Gb}{\Lambda} + \frac{5}{2\pi}Gf\varepsilon_p\right), \quad (7)$$

where Λ is the distance between fibres and ε_p is plastic deformation. It is widely accepted, however, that Orowan strengthening is

not significant for metal matrix composites because the reinforcements are coarse and the interfibre spacing is large. In our case, if Λ measures in units of μm, the increase of the yield stress $\Delta\sigma_{OR}$ is not significant.

Grain size refinement

Discontinuously reinforced composites usually have very fine grains, smaller than their unreinforced matrices [23]. The contribution to the yield stress can then be estimated using the Hall-Petch relation, which relates the yield stress enhancement to grain size

$$\Delta\sigma_{GS} = K_y\,(d_2^{-½} - d_1^{-½}), \tag{8}$$

where K_y is the Hall-Petch constant, d_1 and d_2 the grain sizes of the coarse and fine grained alloy or composite, respectively. Subgrains may contribute to the composite strengthening in the similar way as the grain boundaries. It should be mentioned that Arsenault and co-workers [24] observed smaller subgrain size in Al composites reinforced by SiC particles. They suggested other contribution to the strengthening due to a reduction of dislocation cell size.

Thermally induced plastic flow

Chmelík and co-workers [25–27] studied induced plastic strains in Mg alloy based composites using non-destructive methods. Acoustic emission was detected in situ during thermal cycling of composites between room temperature and increasing upper temperature of the thermal cycle in a dilatometer equipped with a radiant furnace. After each cycle the residual strain was measured. As a consequence of the fabrication at elevated temperatures, both components of the metal matrix composite i.e. matrix as well as reinforcement are in equilibrium only at the manufacturing temperature. They exhibit internal thermal stresses at room temperature whose magnitude should be close to a minimum stress necessary for matrix micro-strain. The matrix is under tensile stresses and the reinforcement is under compressive stresses. When a MMC is heated up, the internal tensile stress acting on the matrix decreases to zero and on further heating compressive stresses build up. On cooling the internal stresses will behave in an opposite manner.

Residual thermal stresses

At higher temperatures, stresses can achieve the yield stress and the composite is plastically deformed only owing to the temperature cycling. Thermal stresses directly near the matrix-fibre interphase may be calculated in the simple approximation [28] as

$$\sigma_{TS} = \frac{E_f E_M}{\left(E_f f + E_M(1-f)\right)} f\Delta\alpha\Delta T\,, \tag{9}$$

where E_f and E_M are Young's moduli of the reinforcing phase fibres or particles and the matrix, respectively. Relation (9) estimates thermal stresses directly at the interphase. In a certain distance from the fibre, the thermal stress is lower because it decreases with the distance. Volume-averaged residual stresses reach in the matrix their maximum value [28]

$$\langle\sigma_m\rangle_{\max} = \frac{2}{3}\sigma_{ym}\ln\left(\frac{1}{f}\right)\frac{f}{1-f}\,, \tag{10}$$

where σ_{ym} is the yield stress in the matrix.

Combination of strengthening terms

Several schemes have been proposed for addition of the various strengthening terms. The most commonly accepted are those reviewed by Lilholt [29] who differentiates between the range of magnitude of the strengthening mechanisms and their relative strength. In principle, computer models are required to sample statistically the different contributions. Clearly, stress contributions, which act more or less uniformly throughout the matrix must be superimposed linearly, whereas mechanisms of similar strengthening ability, which act unevenly throughout the matrix, are most suitably combined as the square root of the sum of the squares [30].

Comparison with experimental results

All individual contributions to the strengthening for both materials calculated using constants introduced in Table 2 are summarised in Table 1 together with the linear and quadratic sum. Comparison with the experimental values of the yield stress obtained for room temperature for both materials showed that the linear sum gave the higher values of the total stress necessary for the deformation of the hybrid composites while the quadratic sum is lower than the stress estimated experimentally. It is also necessary to note that models for each mechanism are constructed for the perfect bonding between the matrix and the reinforcing phase. If the bonding is not perfect the contribution to the strengthening is lower. From this point of view the linear sum seems to be more suitable for the estimation of the ceramic phase reinforcing effect. Non-uniform distribution of reinforcing phase (fibres and particles) must be also taken into account. As it follows from Table 1, the increased dislocation density is in the most important contribution to strengthening.

Contribution of various strengthening mechanisms to the yield stress of composites — Tab. 1

	AS21	AZ91
σ_{02} alloy (MPa)	112	116
$\Delta\sigma_{LT}$ (MPa)	28.7	30
$\Delta\sigma_{D}$ (MPa)	69	69
$\Delta\sigma_{OR}$ (MPa)	5	5
$\Delta\sigma_{GS}$ (MPa)	10	15
$\langle\sigma_m\rangle_{max}$ (MPa)	30	31
σ_{total} (MPa) (linear)	254.7	266
σ_{total} (MPa) (root of sum of squares)	193.3	198.9
$\sigma_{02experimental}$ (MPa)	218	244

Constants used for calculations in Table 1. Tab. 2

α(AZ91) (K^{-1})	α(AS21) (K^{-1})	α(Saffil) (K^{-1})	α(SiC) (K^{-1})	K_y (Mg) ($MPam^{-3/2}$)	α1 (hcp)	Taylor factor ψ	b (m)	G (GPa)
26	30	6×10^{-6}	6.6×10^{-6}	0.28	0.35	6	3.21×10^{-10}	17
[9]	[9]	[31]	[31]	[32]	[33]	[34]		

4.2 Recovery mechanisms

The observed steady state character of the stress strain curves obtained at elevated temperatures, where maximum stress was achieved already at lower strain and subsequent stress is constant or decreases, indicates an operating of some recovery mechanism/-s. Cross slip in prismatic or pyramidal planes is very probably the main recovery mechanism. The recovery mechanisms are strongly thermally activated. An increased activity of prismatic and pyramidal slip systems with <*c*> and <*c*+*a*> dislocations, respectively, at higher temperatures provides explanation for the observed decrease of the flow stress. Cross-slip as well as the subsequent annihilation of dislocations results in a decrease in the work hardening rate.

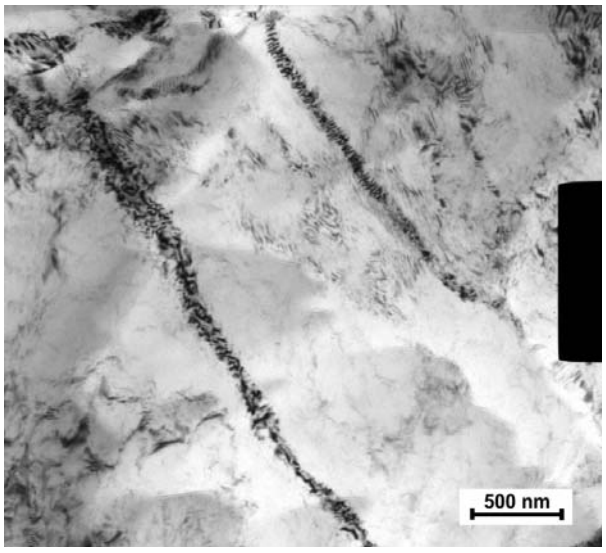

Fig. 9: Dislocation pile-ups in deformed AS21h composite.

Plastic deformation in a composite begins by developing the strain in the vicinity of fibres or particles, where dislocation density is higher than elsewhere in the matrix. Dislocations cannot pass through the reinforcing fibres or particles without leaving loops around fibres. This passing mechanism is similar to the Orowan mechanism and it is also athermal. Dislocations pile-ups formed can act as stress concentrators. The screw dislocation components locally cross slip, forming superjogs having a height of about fibre diameter. At higher temperatures, edge components are able to climb. In both cases, dislocations may then annihilate in neighbouring slip planes. Possible annihilation of dislocations may be also supported by the interfacial diffusion of vacancies in the thin layer at the matrix-fibre interface [35]. Dislocation pile-ups formed in the vicinity of reinforcing phase were observed by TEM in deformed composites as it is shown for the AS21h composite in Fig. 9.

5. Conclusions

Ceramics fibres and particles influence significantly mechanical properties of composites with the AS21 and AZ91 matrix. As it follows from the Table 1 the significant strengthening mechanisms in composites studied are increased dislocations density and the load transfer in which the part of the external load within the matrix is transferred to reinforcement. While the shear lag model used supposes a perfect bonding at the interface between matrix and reinforcing phase, the real values of this contribution are very probably lower. Different precipitates in the monolithic alloy and in the matrix of the hybrid composite contribute by different way to the precipitation hardening in the matrix. Higher thermal stability of Mg2Si precipitates is very probably reason for better high temperature properties of the AS21 hybrid composite.

Acknowledgements

The authors acknowledge financial support of the Grant Agency of the Czech Republic under grant 106/06/1354. The authors are grateful also for the support offered by the Czech and Slovak authorities under the Exchange Programme MEB 0808116.

References

[1] FRITZE, C., BEREK, H., KAINER, K.U., MIELKE, S., WIELAGE B. in: MORDIKE, B.L., KAINER, K. U. (Eds.): M*agnesium Alloys and their Applications*, Werkstoff-Informationsgesellschaft, Oberursel, 1998, 635.
[2] BAO, G., HUTCHINSON, J.W., McMEEKING, R.M.: *Acta Metall. Mater.* 1991, 39, 1871.
[3] CHRISTMAN, T., NEEDLEMAN, A., SURESH, S.: *Acta Metall.* 37, 1989, 3029.
[4] SHEN, Y.-L., FINOT, M., NEEDLEMAN, A., SURESH, S.: *Acta Metall. Mater.* 43, 1995, 1701.
[5] MUELLER, R., MORTENSEN, A.: *Acta Mater.* 54, 2006, 2145.
[6] TORQUATO, S.: *Random heterogeneous materials: microstructure and macroscopic properties.* New York, Springer, 2002.

[7] TROJANOVA, Z., GARTNEROVA, V., LUKAC, P., DROZD, Z.: *J. Alloys Comp.* 378, 2004, 19.
[8] POLMEAR, I.J., MORDIKE, B.L., HEHMANN, F. (Eds.) in: *Magnesium Alloys and Their Applications*, DGM, Oberursel, 1992, 201.
[9] ADVESIAN, M.M., BAKER, H. (Eds.): *Magnesium and Magnesium Alloys.* ASTM International Materials Park 2000.
[10] TROJANOVA, Z., SZARAZ, Z: *Mater. Sci. Forum* 482, 2005, 363.
[11] TROJANOVA, Z., LUKAC, P., GABOR, P., DROZD, Z., MATHIS, K.: *Kovove Mater.* 39, 2001, 368.
[12] DROZD, Z., TROJANOVA, Z., GÄRTNEROVA, V.: *Magnesium Alloys and Their Applications,* Ed. KAINER, K. U., DGM, Willey 2003, 122.
[13] FUKUDA, H., CHOU, T. W.: *J. Compos. Mater.* 15, 1981,79.
[14] NARDONE, V. C., PREWO, K. M.: *Scripta Metall.* 20, 1986, 43.
[15] CLYNE, T. W.: *Mater. Sci. Eng. A*, 122, 1989, 183.
[16] TAYA, M., ARSENAULT, R. J.: *Scripta Metall.* 21, 1987, 349.
[17] AIKIN JR., R. M., CHRISTODOULOU, L.: *Scripta Metal. Mater.* 25, 1991, 9.
[18] ARSENAULT, J.R., SHI, N.: *Mater. Sci. Engn.* 81, 1986, 853.
[19] TROJANOVA, Z., LUKAC, P., RUDAJEVOVA, A.: *Mater. Sci. Engn. A*, 370, 2004, 542.
[20] TROJANOVA, Z., SZARAZ, Z., LABAR, J., LUKAC, P.: *J. Mater. Process. Techn.* 162–163, 2005, 131.
[21] ASHBY, M.F.: *Phil Mag.* 21, 1970, 399.
[22] SCATTERGOOD, R. O., BACON, D.: *Phil. Mag.* A31, 1975, 179.
[23] MILLER W. S., HUMPHREYS F. J.: *Scripta Metall. Mater.* 25, 1991, 33.
[24] ARSENAULT, R. J., WANG, L., FENG, C. R.: *Acta Metall. Mater.* 39, 1991, 47.
[25] CHMELIK, F., LUKAC, P., KIEHN, J., MORDIKE, B. L., KAINER, K. U., LANGDON, T. G.: *Mater. Sci. Eng. A* 325, 2002, 320.
[26] CHMELIK, F., KIEHN, J., LUKAC, P., KAINER, K. U., MORDIKE, B. L.: *Scripta Mater.* 38, 1998, 81.
[27] CHMELIK, F., LUKAC, P., KUDELA, S., KIEHN, J., MORDIKE, B. L., KAINER, K. U.: *Magnesium Alloys and their Applications.* Ed. KAINER, K.U., Wiley-VCH Weinheim 2000, 229.
[28] DELANNAY, F.: *Comprehensive Composite Materials,* CLYNE, T.W. (Ed.), Vol. 3, Elsevier, Amsterdam, 2000, 341.
[29] LILHOLT, N.: *Deformation of Multi-Phase and Particle Containing Materials.* Eds. BILDE SORENSON, J. B., HANSEN, N., HORSEWELL, A., LEFFERS, T., LILHOLT, H., Riso Nat. Lab. 1983, Roskilde, 381.
[30] CLYNE, T., WHITHERS, J. P.: *An Introduction to Metal Matrix Composites,* Cambridge Press, Cambridge 1993, 94.
[31] Handbook of Chemistry and Physics. (Ed. D.R. Lide), 73rd edition. CRC Press, 1992/1993.
[32] MABUCHI, M., KUBOTA, K. HIGASHI, K.: *Mater. Trans.JIM* 36, 1995, 1249.
[33] LAVRENTEV, F. F., POKHIL, Y. A., ZOLOTUKHINA: I. N.: *Mater. Sci. Engn.* 32, 1978, 113.
[34] ARMSTRONG, R. W.: *Acta metall.* 16, 1968, 347.
[35] SHEWFELT, R. S. W., BROWN, L. M.: *Phil. Mag.* 35, 1977, 945.

Josef Zapletal – Stanislav Vechet – Jan Kohout – Petr Liskutin *

FATIGUE LIFETIME OF 7075 ALUMINIUM ALLOY FROM ULTIMATE TENSILE STRENGTH TO PERMANENT FATIGUE LIMIT

The aim of this paper is to study fatigue behaviour of 7075 aluminium alloy at room temperature for both important directions (longitudinal as well as transversal) with respect to the direction of forming. Smooth test bars were subjected to symmetrical push-pull loading at stresses which cover the whole range of lifetime from UTS to permanent fatigue limit. The results are presented above all as S-N curves fitted using suitable regression functions which lead to precise and reliable determination of fatigue limits.

1. Introduction

Age-hardened aluminium alloys containing Zn, Mg and Cu belong to structural aluminium alloys with the highest strength. They are usually applied for highly loaded structural details in aircraft, automotive and motorbike industry. These details cannot be welded because due to high predisposion to crackability at higher temperatures those alloys are considered to be unweldable. Studied aluminium alloy marked according to ASTM as 7075 is a typical representative of the mentioned alloys [1, 2]. Although the fatigue properties of 7075 alloy were already studied, e.g. [3–5], only rarely the tests were performed for a number of cycles to fracture higher than 10^6 [5]. The contribution of the present paper consists in a complete study covering the whole meaningful range of cycle numbers to fracture from UTS to more than 10^8 cycles.

2. Experimental

Test bars for tensile as well as for fatigue tests were made of 7075 aluminium alloy delivered as formed rectangular sections with cross-section of 70 × 16 mm by Alcan Decin Extrusion, limited company. Delivered sections were heat treated into T6 state, i.e. by artificial ageing during 4 to 6 hours at temperatures of 160 to 180 °C. Chemical composition determined by the corresponding standard is given in Table 1.

For tensile tests the bars of 6 mm in diameter and of 30 mm in nominal length were used, ended with threaded heads and loaded at a strain rate of $6 \times 10^{-4}\ s^{-1}$ at a PC controlled TiraTest 2300 testing device. Strain of bars was measured with an extensometer having a base length of 30 mm.

For fatigue loading the test bars of 6 mm in diameter and of 12.5 mm in nominal length with threaded heads were used for low-cycle as well as for high-cycle region. Strain was measured with an axial extensometer with a base length of 12.5 mm. All tests (tensile and also fatigue tests) were performed at room temperature.

All fatigue test bars were loaded in the regime of controlled force with sinusoidal symmetrical push-pull loading cycle (parameters of loading cycle asymmetry were $R = -1$, i.e. $P = 1$). For fatigue tests different devices and different frequencies were used. In a low-cycle region a servohydraulic PC controlled Instron 8801 machine was used at a loading frequency of 5 Hz for stress amplitudes of 300 MPa or higher and at a frequency of 30 Hz for stress amplitudes of 250 MPa or lower. In a high-cycle region a high-frequency Amsler HFP 1478 pulsator was used at loading frequency of 144 Hz. While the servohydraulic machine can work at any chosen frequency lower than the limit frequency of the machine, the frequency of the resonant pulsator as the natural frequency of

Prescribed chemical composition of studied aluminium alloy — Table 1.

Element	Zn	Mg	Cu	Si	Mn	Cr	Ti	Al
[wt. %]	5.1 ÷ 6.1	2.1 ÷ 2.9	1.2 ÷ 2.0	max. 0.4	max. 0.3	0.18 ÷ 0.28	max. 0.2	rest

* **Josef Zapletal[1], Stanislav Vechet[1], Jan Kohout[2], Petr Liskutin[1]**
[1]Institute of Materials Science and Engineering, Faculty of Mechanical Engineering, Brno University of Technology, Brno, Czech Republic,
*E-mail: Pepa.Sanguis@centrum.cz
[2]Department of Mathematics and Physics, Faculty of Military Technology, University of Defence, Brno, Czech Republic

an oscillating system is fully determined by the stiffness of the test bar.

3. Results

3.1 Static tensile tests

The results of static tensile tests (proof stress $R_{p0.2}$, UTS R_m, elongation to fracture A_5 and reduction of area Z) are given in Table 2 for both the directions: longitudinal (L) as well as transversal (T). Also Young's modulus values E are added. Each presented value is an average of three values corresponding to three tested bars.

Static mechanical properties of studied alloy together with Young's modulus — Table 2.

Direction	$R_{p0.2}$ [MPa]	R_m [MPa]	A_5 [%]	Z [%]	E [GPa]
L	558	627	12.1	18.2	72.3
T	540	612	10.6	16.5	71.6

The results for different directions with respect to the direction of forming are nearly the same. The smallest relative difference (cca 1 %) is between the values of Young's modulus, nevertheless even so small difference in the quantity describing elastic strain behaviour can mean observable anisotropy of alloy microstructure.

3.2 Fatigue results

The studies started by fatigue behaviour for L direction, which was studied up to now more deeply than for T direction, therefore basic considerations will be done for L direction. The first crucial question of all the studies consisted in the fact if not only fatigue tests performed at different frequencies but even using different devices with different incurrence of loading forces (servohydraulic vs. resonant machines) could give well comparable results which, moreover, should be consistent in a very low cycle region also with the values of UTS (which is considered to correspond to one quarter of a loading cycle). A clear graphical answer is given in Fig. 1; the all experimental results seem to lie on one smooth curve without any discontinuity or discrepancy. Therefore, there is no reason to infirm the regularity of fatigue tests performance.

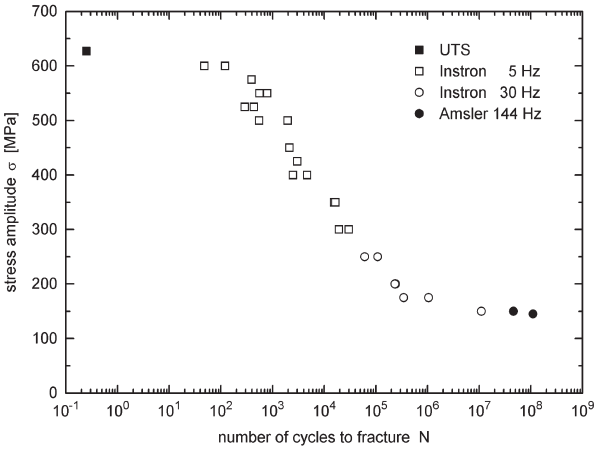

Fig. 1 Results of tensile and fatigue tests performed at different conditions lying on one smooth curve without any discontinuity.

3.3 Fit of S-N curves

For the fit of S-N curves covering the whole range of the number of cycles to fracture from UTS to permanent fatigue limit (so called gigacycle fatigue is not considered here because no results for 10^9 and more cycles to fracture were available) only two regression functions are suitable: the Palmgren function [6]

$$\sigma(N) = a(N + B)^b + \sigma_\infty \tag{1}$$

or the Kohout and Vechet function [7]

$$\sigma(N) = \sigma_\infty \left(\frac{N + B}{N + C}\right)^b \tag{2}$$

where a, b, B, C and σ_∞ are parameters determined in regression calculations. Some of them represent a geometrical characteristic of the regression curve or have a clear physical meaning. Parameter b is the slope of the curve in the inflexion point if log N–log σ fit is used, parameters B and C describe the positions of the points with the maximum curvatures of S-N curve and σ_∞ represents limit value of stress amplitude for infinite number of cycles to fracture. The fits using both the regression functions are compared in Fig. 2. The values of regression parameters of both the functions together with the sums S of squares of deviations are presented in Table 3, together with fatigue limit values σ_C for 10^8 cycles (in contrast to ferrous alloys the fatigue stress of aluminium alloys is decreasing with increasing number of cycles to fracture even above 10^7 cycles, therefore not 10^7 cycles as for ferrous alloys but 10^8 cycles create the base for the determination of fatigue limit of aluminium alloys).

Values of regression parameters, fatigue limit values σ_C and sums S for S-N curve of test bars oriented in L direction — Table 3.

Function	a [MPa]	b [-]	B [-]	C [-]	σ_∞ [MPa]	σ_C [MPa]	S [MPa2]
Palmgren (1)	32 967	−0.2862	782.0	-	118.1	135.1	12 848.38
K + V (2)	-	−0.1787	480.5	1 532 411.8	145.2	145.6	11 440.89

The choice of a better regression function is neither simple nor unambiguous: the Palmgren function represents a worse fit (its sum of squares of deviations is 12.3 % higher than that for the Kohout and Vechet function) but, on the other hand, it better takes into account decreasing fatigue stress in the range of number of cycles to fracture above 10^7.

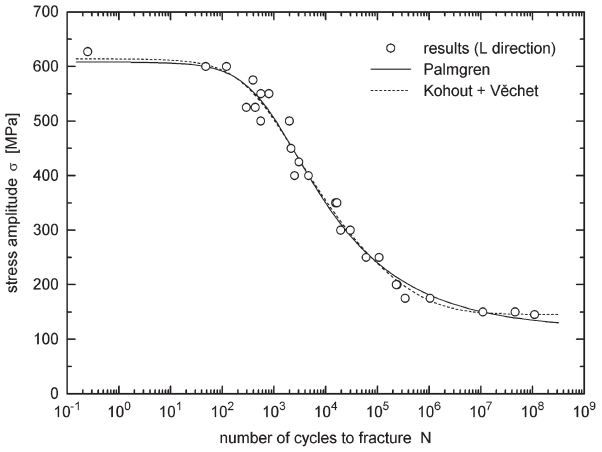

Fig. 2 Comparison of fits using the Palmgren (1) and the Kohout and Vechet (2) regression functions for test bars oriented in L direction.

Up to now the fatigue tests for T direction were performed only using Instron 8801 machine, only up to 10^7 cycles to fracture. Also their results were fitted using the Palmgren (1) as well as the Kohout and Vechet function (2), see Fig. 3. The values of regression parameters of both the functions together with the sums S of squares of deviations and with fatigue limit values σ_C for 108 cycles are presented in Table 4.

The problem to decide which regression function is better is here similar as in previous case of L orientation: a better fit using Kohout and Vechet function (for the Palmgren function the sum of squares of deviations is even 23.9 % higher than for the mentioned one) and a better description of decreasing fatigue stress in a very high cycle region using the Palmgren function.

Finally, the comparison of the results corresponding to different orientations of test bars to the direction of forming is presented in Fig. 4, namely using the Palmgren function. As the figure shows, the difference of both curves is convincingly lower than the dispersion of the results of fatigue tests. Therefore, the difference of fatigue properties in L and T directions is not important. However, the dispersion of results corresponding to T direction is substantially lower than that corresponding to L direction, see nearly one order lower corresponding sums of squares of deviations.

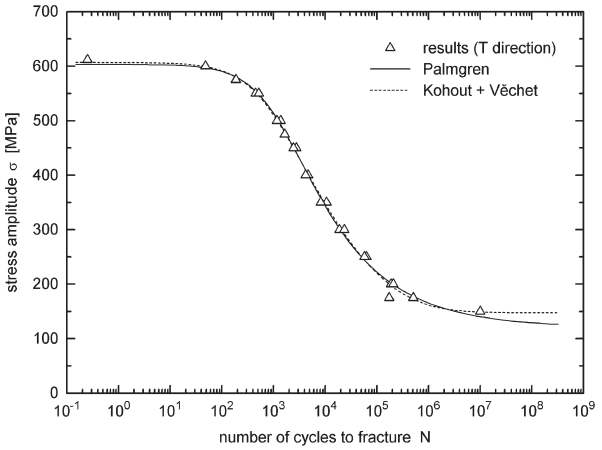

Fig. 3 Comparison of fits using the Palmgren (1) and the Kohout and Vechet (2) regression functions for test bars oriented in T direction.

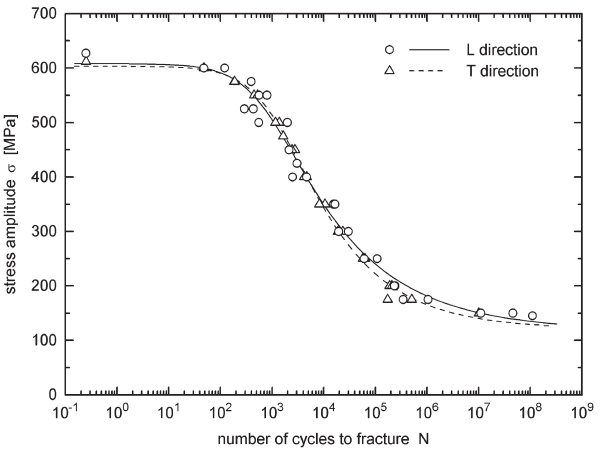

Fig. 4 Comparison of fits using the Palmgren regression function (1) for test bars oriented in both L and T directions.

3.4 Static vs. cyclic curve

The stress-strain hysteresis loops of 17 test bars oriented in L direction were observed at stress amplitudes between 300 and 600

Values of regression parameters, fatigue limit values σ_C and sums S for S-N curve of test bars oriented in T direction Table 4.

Function	a [MPa]	b [-]	B [-]	C [-]	σ_∞ [MPa]	σ_C [MPa]	S [MPa2]
Palmgren (1)	6 209	-0.3568	1 285.9	-	120.6	140.3	1 824.56
K + V (2)	-	-0.2193	833.0	533 084.8	147.1	148.8	1 472.88

MPa to the state of saturation. Chosen stress levels with saturated values of strain define a so called cyclic deformation curve, see Fig. 5. The points corresponding to single bars are fitted using the Ramberg and Osgood relationship [8] representing the total strain as the sum of elastic strain (proportional to stress according to Hook's law) and plastic stress (power function of stress)

$$\varepsilon(\sigma) = \frac{\sigma}{E} + K\left(\frac{\sigma}{E}\right)^{n} \tag{3}$$

where ε is strain, σ is stress, E is Young's modulus, K and n are constants that depend on the material being considered. As the values of parameter K are usually extremely high, the original relationship is often modified into the relation [9]

$$\varepsilon(\sigma) = \frac{\sigma}{E} + \left(\frac{\sigma}{\sigma_0}\right)^{n} \tag{4}$$

which was used also in this case. The values of parameters are presented in Table 5.

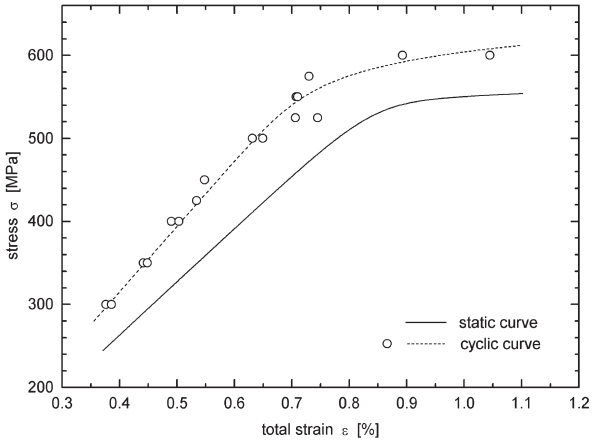

Fig. 5 Comparison of static stress-strain curve with cyclic deformation curve presenting cyclic hardening of studied alloy loaded in L direction.

Parameters of the Ramberg and Osgood relationship for cyclic deformation curve. Table 5.

Parameter	E [GPa]	σ_0 [MPa]	n [-]
Value	78.8	769.9	25.0

The cyclic curve situated higher than the static curve shows that the fatigue loading leads to cyclic hardening of the studied alloy. Also the value of *cyclic* Young's modulus about 10 % higher than the values of *static* Young's modulus (cf. Tables 2 and 5) denotes cyclic hardening.

All regression calculations were made in MS Excel using supplement *Solver* with suitably chosen parameters and tools which take into account a higher degree of non-linearity of used regression functions. All calculations ran without any complication, only some difficulties appeared during regression of the cyclic deformation curve because the region of strain above the bend of the curve is covered with two points only.

4. Discussion

Nearly the same 7075-T651 aluminium alloy was studied by Zhao and Jiang [3] using nearly the same servohydraulic machine (Instron 8800) but only up to 10^6 cycles to fracture. It is surely no surprise that our and their results of fatigue tests are not (with respect to the dispersion of experimental data) distinguishable. A markedly higher fatigue limit is presented for 7075-T6 alloy by Wang et al. [5], but the higher value can be explained by a higher-order frequency of loading cycles in the ultrasonic region (19.5 kHz).

The results show nearly no difference between different orientation of test bars with respect to the direction of forming, see Table 2 dealing with static behaviour in tension and Fig. 4 dealing with fatigue behaviour. On the other hand, certain deviations can be observed: substantially different dispersion of fatigue results and slightly different values of Young's modulus which is not usually too sensitive to microstructure. First metallographic studies show certain, but not substantial difference, in the arrangement of strengthening precipitates. It seems that the tools of statistics would be useful for the description of small differences in microstructure. This aspect is going to be studied.

The resulting fatigue limits σ_C determined as the values of fitted curves for 10^8 cycles to fracture depend on the type of regression function. Their values are lower for the Palmgren function (1) and higher for the Kohout and Vechet function (2), see Tables 3 and 4. As the former gives too conservative values and the latter too progressive values, the intervals between them seem to be quite representative approximations of fatigue limit values, i.e. (140 ± 5) MPa for L direction and (144 ± 4) MPa for T direction. Also overlapping intervals of the fatigue limit values are evidence of unsubstantial difference in fatigue behaviour in both mentioned directions.

In the paper the term *permanent fatigue limit* is several time used (also in the title) similarly as for ferrous metals although the fatigue stress of aluminium alloys decreases even above 10^7 cycles to fracture. It means that this term is not too suitable for those alloys. Just this decreasing fatigue stress is the reason why the Kohout and Vechet function with surely better fit is not unambiguously preferred and the Palmgren fit giving more conservative values of fatigue limit is slightly favoured. The decision between both the mentioned regression functions needs a substantially larger set of fatigue results of aluminium alloys.

Generally said, cyclic hardening is typical for the metals with lower level of stress properties and cyclic softening is observed at fatigue loading of hardened metals, e.g. deeply formed or quenched steels. In age-hardened alloys only precipitation strengthening is

exploited, increasing dislocation density during fatigue loading and interactions among dislocations and precipitates lead to additional hardening. These mechanisms were confirmed by profound study of the mechanisms of cyclic deformation [10] as well as by finite element prediction [11]. Cyclic hardening following after age-hardening represents a substantial advantage of these types of structural materials leading to their wide applicability in many branches of industry.

5. Conclusions

1. The studied 7075 alloy reaches a very high level of strength and deformability as a result of optimized age-hardening.
2. No discontinuity or discrepancy was found among the results of fatigue tests performed using different frequencies of fatigue loading and even different testing devices (all results lie on one smooth S-N curve).
3. Fatigue loading of the studied age-hardened alloy leads to further cyclic hardening.
4. Mechanical properties of the test bars oriented longitudinally and transversally to the direction of forming are only negligibly different.
5. The fit of S-N curves from UTS to permanent fatigue limit can be made using the Palmgren or the Kohout and Vechet regression function. The Palmgren function takes better into account the fact of decreasing fatigue stress in a very high cycle region leading to more conservative and, thereby, safer values of fatigue limit, the Kohout and Vechet function gives substantially better fit of experimental data. The decision between both the mentioned functions needs further extensive studies.

Acknowledgement

Financial support of the Ministry of Education, Youth and Sports of the Czech Republic within the research project 1M2560471601 Eco-Centre for Applied Research of Non-Ferrous Metals is gratefully acknowledged.

References

[1] SEDLACEK, V.: *Fatigue of Aluminium and Titanium Alloys (in Czech),* Praha: SNTL, 1989.
[2] MICHNA, S. et al.: *Encyclopaedia of Aluminium (in Czech),* Presov: Adin, 2005.
[3] ZHAO, T., JIANG, Z.: *Fatigue of 7075-T651 Aluminium Alloy,* International Journal of Fatigue, 11/2008, pp. 834–849.
[4] BOLLER, CHR., SEEGER, T. (eds): *Materials Data for Cyclic Loading. Part D: Aluminium and titanium alloys.* New York, Elsevier, 1987.
[5] WANG, QY., KAWAGOISHI, N., CHEN, Q.: *Fatigue and Fracture Behaviour of Structural Al-alloys up to Very Long Life Regimes,* International Journal of Fatigue, 11/2006, pp. 1572–1576.
[6] WEIBULL, W.: *Fatigue Testing and Analysis of Results,* Oxford: Pergamon Press, 1961.
[7] KOHOUT, J., VECHET, S.: *A New Function for Description of Fatigue Curves and Its Multiple Merits,* International Journal of Fatigue, 2/2001, pp. 175–183.
[8] RAMBERG, W., OSGOOD, W. R.: *Description of Stress-Strain Curves by Three Parameters,* Technical Note No. 902, Washington DC: National Advisory Committee for Aeronautics, 1943.
[9] BLUMENAUER, H., PUSCH, G.: *Technische Bruchmechanik,* Leipzig: Deutscher Verlag fur Grundstoffindustrie, 1982 (1st edition).
[10] KASCHNER, G. C., GIBELING, J. C.: *A Study of the Mechanisms of Cyclic Deformation in F.C.C. Metals Using Strain Rate Change Tests,* Materials Science and Engineering A, 1–2/2002, pp. 170–176.
[11] BAXTER, W. J., WANG, P-C.: *Finite Element Prediction of High Cycle Fatigue Life of Aluminium Alloys,* Metallurgical and Materials Transactions A, 4/1990, pp. 1151–1159.

Ivo Cerny – Dagmar Mikulova *

FATIGUE RESISTANCE OF HIGH-THICKNESS AL-ALLOY SHEETS AFTER WATER JET CUTTING

Water jet cutting is a useful advanced technology of separating materials with a great industrial potential due to high cutting speed, precision, shape repeatability and possibilities to be performed automatically with a computer control. It is well known, however, that fatigue properties are particularly strongly affected by surface conditions and quality of surface layer. Water jet cutting was applied to Al-alloy sheets of fairly high thickness, namely 50.8 mm. Fatigue resistance of water cut specimens and failure mechanisms were investigated and compared with those studied using a reference batch of specimens manufactured by fine milling. Character of surface damage caused by water jet cutting resulted in a considerable reduction of fatigue strength in comparison with milled surface. The results are discussed considering microscopic analysis of surface and subsurface conditions of fatigue crack initiation.

1. Introduction

Water jet machining (WJM) is an advanced promising technology, which can be used for cutting either metals or other non-metallic materials like glass reinforced composites, ceramics or even glass plates [1]. This technology, or abrasive water jet machining as its modification, is advantageously used particularly for cutting a variety of difficult-to-machine materials. Since water jet machining systems are quite expensive, new methodologies are being developed to enable to use advantages of water jet machining in small and medium enterprises [2]. Surface and kerf quality after water jet machining always has to be evaluated for specific applications from the point of view of both material and technological parameters, because existing knowledge about water-jet cutting and machining is still ambiguous [3]. WJM is usually connected with surface unevenness, with typical texture marks called striations [4], whose character depends on water jet parameters. Generally, striations arise for three reasons, namely the nature of the step formation inherent to a jet cutting process, the dynamic characteristics of the water jet, and the vibration of the machining system [5]. As an example, in case of abrasive WJM, formation of striations and surface quality depends on distribution of particles in the water jet [6]. Surface quality after WJM and kerf parameters are strongly affected by nozzle diameter and also by number of waves in water flow [1].

It is known that surface quality and roughness generally significantly affects fatigue behaviour, as fatigue crack initiation process is mostly located in material surface layers [7, 8]. A specific effect of the surface quality is, however, connected with numerous other parameters like surface strength, microstructure, material notch sensitivity, surface and subsurface residual stresses etc. Though computer models for an evaluation of effects of surface roughness on fatigue resistance have been recently developed [9], actual effects are usually investigated and have to be verified using experimental methods. In most cases, increased surface roughness reduces fatigue limit and fatigue strength. However, it can have only negligible effect, if the roughness is not too big and other fatigue crack initiation mechanisms occur [10].

The work presented in this paper was performed in the context of the knowledge presented in the literature. It was aimed at an experimental investigation of an effect of water jet cutting with specific parameters applied to an Al-alloy sheet of quite big thickness on fatigue behaviour and resistance.

2. Experiments

The experimental material was quite thick sheet of Al-alloy 2124 T851 of the thickness 50.8 mm. Water jet contained abrasive particles. Cutting speed was 81 mm/min. Besides specimens machined by the water jet technology, reference specimens manufactured by classical mechanical machining, by fine milling, were prepared and tested to compare the two methods.

Fatigue tests were performed on SCHENCK PHG 3000 N machine under three point bending (3PB) with load asymmetry $R = 0.1$, test span 62 mm, load frequency 40 Hz (Fig. 1). The specimens were of square cross section 7×7 mm. To exclude possible effects of the position in the thick sheet, three groups of specimens were tested, namely those taken from the top near-surface layer, from the center and from the bottom layer.

* **Ivo Cerny, Dagmar Mikulova**
SVUM a.s., Areal VU 565, CZ-19011 Praha 9, Czech Republic, E-mail: Ivo.Cerny@seznam.cz

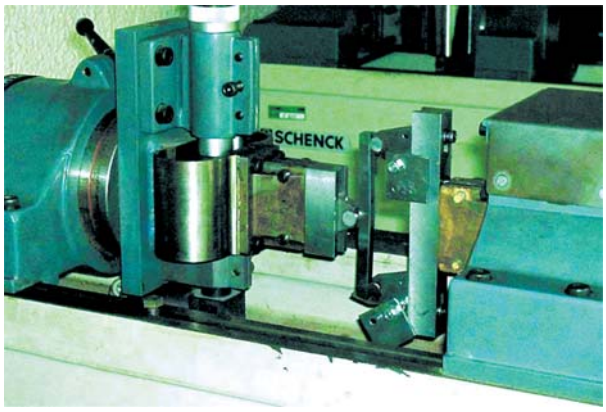

Fig.1 Three-point-bend specimen on the SCHENCK machine

Microstructure analyses were performed using optical microscopes Olympus and Neophot 21, respectively, both with computer digital image processing. Additionally, fractographical and some other analyses were performed using scanning electron microscope JEOL JSM-35, also equipped with digital image processing.

3. Results and discussion

3.1. Cutting surface quality

As regards character of surface area of the thick sheet examined by visual check, the striation phenomenon could be distinctly observed. In Fig. 2, where water jet direction was from bottom to top, there are almost no striations in the bottom area, i.e. in the area of water jet input, unlike distinct striation relief in the top area. A similar relief also was described in [11] – superior surface quality in the jet input region and rough surface in the jet outlet zone. However, it will be shown later that the coarse striation relief was not the most important phenomenon affecting fatigue behaviour.

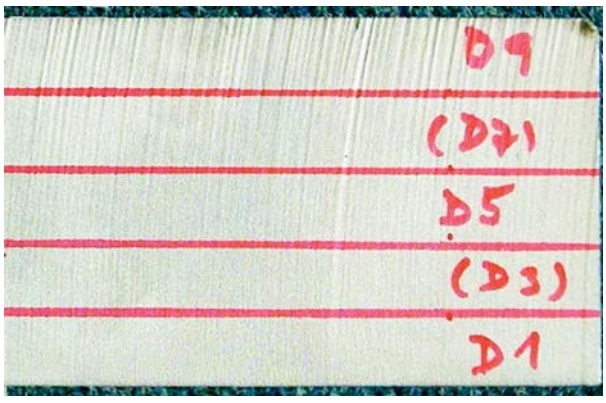

Fig. 2 Visual check of water jet cutting surface with distinct striations in the jet outlet area – the top

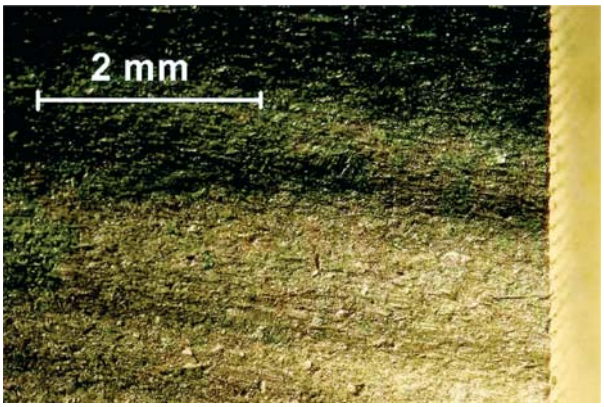

Fig. 3 Macroscopic view of water jet cutting surface with large striations and microscopic roughness

From the macroscopic and microscopic points of view, quite significant differences between machining and water jet cutting were observed. Typical character of water jet cutting surface is shown in Fig. 3. Even the macroscopic analysis indicated that besides the rough striations observable by eye without magnification (Fig. 2), with a typical mutual distance of individual unevenness peaks between 1 – 1.5 mm, the water jet cutting surface was characteristic by another type of roughness, more microscopic, which could be described like "secondary roughness". Fine milling of the specimens taken from the thick sheet was connected with a distinct macroscopic surface relief, but without the microscopic "secondary roughness". The mutual distance of roughness peaks was approximately 0.2 mm – Fig. 4.

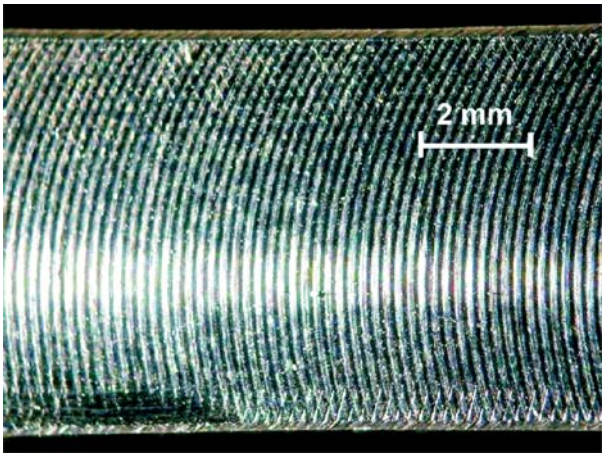

Fig. 4 Character of milled surface

Microscopic analysis was carried out on longitudinal cuts of the specimens. In case of water jet cutting surface, it was shown that the microscopic surface roughness was connected with an unfavourable feature as regards fatigue resistance: an existence of microcracks and sharp micronotches – Fig. 5. In the contrary, notches caused by fine milling were just shallow, without sharp

edges. The character of milled surface analysed on longitudinal cut is in Fig. 6. Another factor, which was found to be important as regards fatigue resistance and mechanisms of initiation of fatigue cracks, was a presence of quite large particles of intermetallic phases, which is for this type of Al-alloy quite typical.

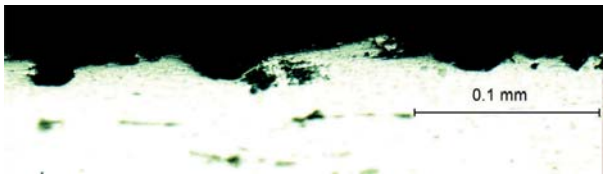

Fig. 5 Microscopic character of water jet cutting surface on longitudinal cut

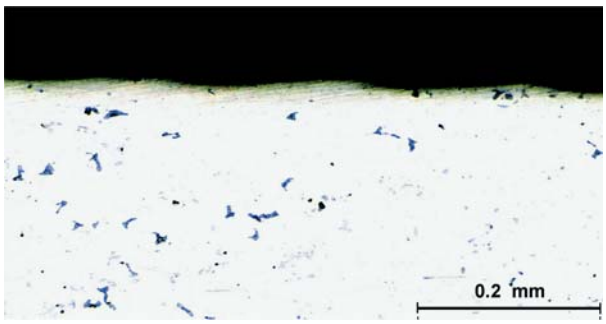

Fig. 6 Milled surface documented on longitudinal cut, showing just shallow notches and quite dense occurrence of large intermetallic particles

3.2. Results of fatigue tests

Results of fatigue tests of specimens with milled surface are in Fig. 7. Individual specimens are marked with letters and figures, the letters indicating position in the sheet (H – top, S – center, D – bottom). Since no distinct dependence of fatigue resistance on this position was ascertained, all the experimental points were plotted together. Fatigue limit of machined specimens was almost 300 MPa, which is quite a high value considering the fact that the surface only was milled with no further improvement like grinding. Statistical analysis showed no significant effects of the position in the sheet, either near two surfaces or in the sheet center, fatigue properties of the sheet along the thickness were homogenous. Therefore, all the points were plotted in the same diagram with the same symbol. Individual points in Fig. 7 were amended with corresponding specimen marking to enable further more detailed analysis of fatigue life and crack initiation mechanisms.

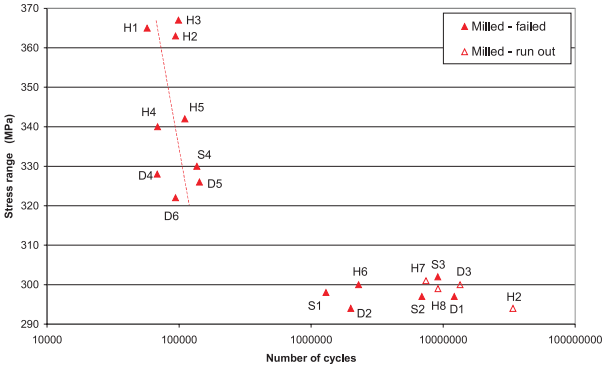

Fig. 7 Fatigue S-N curve of specimens with milled surface

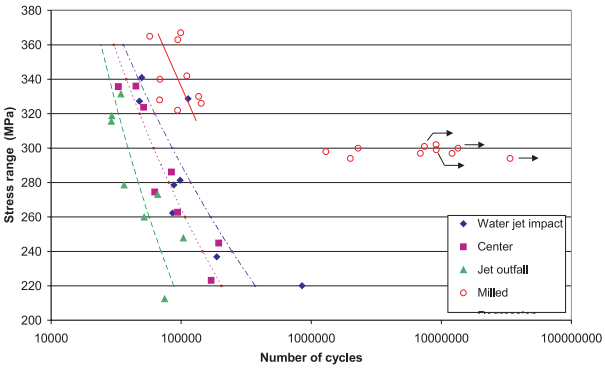

Fig. 8 Results of fatigue tests of specimens with water jet cutting surface in comparison with milled specimens

Fatigue S-N curve of specimens with water jet cutting surface is documented in Fig. 8. Water jet cutting deteriorated fatigue resistance very significantly. In general, fatigue strength corresponded to just about 65% of fatigue strength of milled specimens. Analysing the results more in detail, further characteristic features of the S-N curve were found. The unfavourable effect of water jet cutting was observed not only with stress range near the fatigue limit of milled specimens, 300 MPa, but also in the area of high amplitudes and limited fatigue life. Moreover, there was distinct and statistically significant dependence of fatigue life on the position of specimen in the sheet from the viewpoint of water jet input or outlet: Specimens near the jet outlet, i.e. those taken from the area of rough water jet striations, had the poorest fatigue resistance, whereas these differences were more distinct in the region of lower stress amplitudes.

3.3. Analyses of fatigue cracking mechanisms

Differences between individual points of fatigue life of milled specimens as well as reasons of the unfavourable effect of water jet cutting applied to the thick sheet were evaluated analysing fracture surface, particularly by scanning electron microscopy (SEM).

Looking at the area of limited fatigue life of milled specimens in Fig. 7, some scatter can be seen. Fractographical analysis of crack initiation sites was performed with two different specimens, namely H3 with higher-average fatigue life and H4 with bellow-average life. Figs. 9 and 10 indicate reasons of the different fatigue

resistance. Character of crack initiation areas is quite different. In Fig. 9, specimen H3, fatigue crack was initiated on the surface of maximum stress amplitude, on just a small intermetallic particle. Fig. 10 shows that in specimen H4 with the bellow-average fatigue resistance, fatigue crack initiation occurred at the specimen edge and it was caused by local cumulation of intermetallic particles in this area causing a local reduction of fatigue resistance and fairly premature crack initiation.

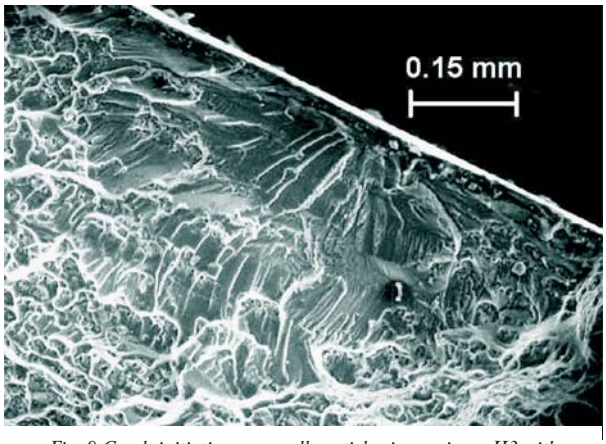

Fig. 9 Crack initiation on small particles in specimen H3 with above-average fatigue life

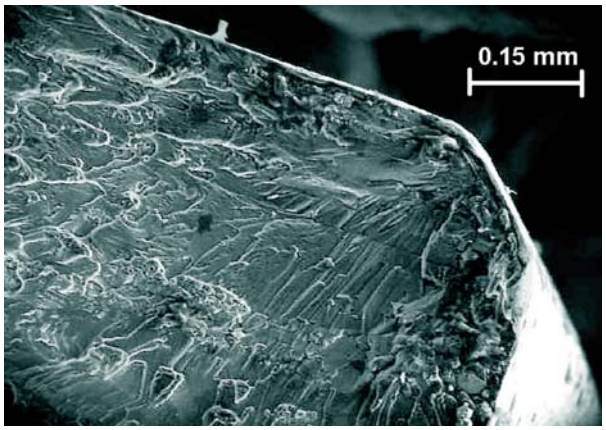

Fig. 10 Crack initiation near edge supported by cumulation of particles in vicinity – specimen H4

Quite a lot of specimens were tested at stress range 300 MPa, close to fatigue limit – Fig. 7. Six of them failed whilst the other four did not. Fractographical analysis of specimen H6, failed after more than 2 million cycles, indicated failure mechanism – Fig. 11. Fatigue crack was initiated in the subsurface area near specimen edge on cumulation of intermetallic particles. The initiation site was located approximately 0.15 mm under the surface. The subsurface initiation mechanism likely affected the retarded failure, after more than 2 million cycles. Retarded failure is quite a typical phenomenon for subsurface crack initiation [12].

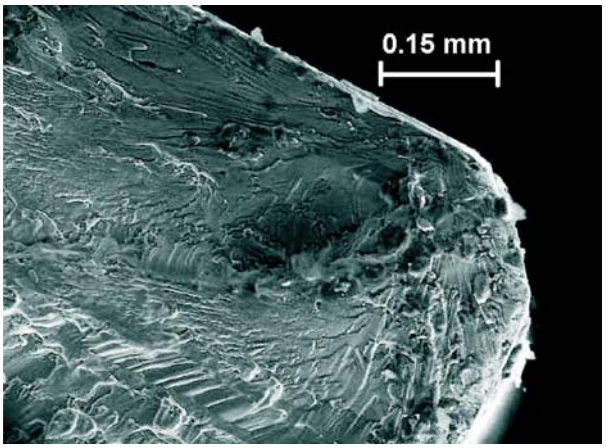

Fig. 11 Subsurface crack initiation in specimen H6 failed during test at stress range near fatigue limit

Analysing the surface of water jet cut specimens with fairly high magnifications, it could be observed that the rough surface (the "secondary roughness" mentioned above) actually contained a lot of sharp notches or surface microcracks, which became initiation sites of fatigue cracks. An initiation site of a main crack with the damaged surface area close to the site is in Fig.12. The initiation area is marked with the arrow. The surface sharp notches and microcracks accelerated the fatigue crack initiation process so strongly that multiple fatigue cracking could be observed. It follows from the diagram in Fig. 8 that the macroscopic surface striation phenomenon, mentioned in the literature as an important type of damage caused by water jet machining [11] and observed also in this work, only had a minor effect on fatigue strength in comparison with the microscopic surface damage by the sharp notches and microcracks.

Considering failure mechanisms, when fatigue crack initiation was either caused or supported by intermetallic particles or by their surface or subsurface cumulation, it could be concluded

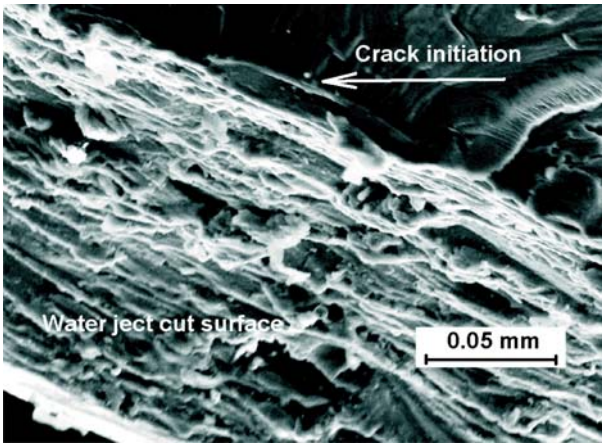

Fig. 12 Characteristic crack initiation site in one of numerous sharp micropits and micronotches caused by water jet cutting

that fatigue resistance in the specific studied case is dependent more on the material resistance against growth of physically short fatigue crack than on the resistance against crack initiation [13].

4. Conclusions

An experimental investigation of an effect of abrasive water jet cutting with specific parameters applied to an Al-alloy 2124 T851 sheet of the thickness 50.8 mm on fatigue resistance was carried out. Reference specimens manufactured by classical mechanical machining, namely fine milling, were tested to compare the two methods. The most important results can be summarised as follows:

- The milling operation resulted in a characteristic surface relief created by shallow notches without further microscopic roughness. Fatigue cracks were initiated mostly on surface or subsurface particles of intermetallic phases. Fatigue life was lower in case of crack initiation on large particles or cumulation of particles in comparison with the initiation on smooth surface or just small particles. Subsurface initiation on cumulation of particles in specimens tested at stress amplitude close to fatigue limit was connected with retarded failure, even more than 107 cycles.
- The abrasive water jet cutting resulted in a rough cutting surface of the sheet. Besides striations visible by eye, numerous microscopic sharp notches and micropits of a big density could be observed on the surface.
- The water jet cutting technology applied to the thick sheet resulted in a significant reduction of fatigue strength, by about 35%. Fatigue cracks initiated in some of the numerous surface sharp notches and microcracks, whereas multiple fatigue crack initiation was observed.

The results showed that for this type of sheet, water jet cutting cannot be used as a final technology operation without further surface treatment, if the component or part will be exposed to considerably variable stress. The actual fatigue resistance looks to be affected more by resistance of the material against growth of physically short cracks or by notch sensitivity, respectively, than by resistance against fatigue crack initiation on smooth surface.

Acknowledgement

The work has been carried out within the project supported by the Czech Ministry of Education, Youth and Sport under grant MSM 2579700001.

References

[1] ZHU, H. T., HUANG, C. Z., WANG, J., LU, X. Z., FENG, Z. X.*: Mach Inability of Glass by Abrasive Water Jet,* Int. J. of Materials and Product Technology, Vol. 31, 1/2007, pp.106–112

[2] GEREN, N., BAYRAMOGLU, M., ESME, U.: *Improvement of a Low-Cost Water Jet Machining Intensifier Using Reverse Engineering and Redesign Methodology,* J. of Engineering Design, Vol. 18, 1/2007, pp. 13–37

[3] JOU M.: *Analysis of The Stability of Water-Jet Cutting With Linear Theory,* J. of Materials Processing Technology, Vol. 104, 1/2000, pp. 17–20

[4] CHEN, F. L., SIORES, E.: *The Effect of Cutting Jet Variation on Surface Striation Formation in Abrasive Water Jet Cutting,* J. of Materials Processing Technology, Vol. 135, 1/2003, pp. 1–5

[5] CHEN, F. L., WANG, J., LEMMA E., SIORES, E.: *Striation Formation Mechanisms on The Jet Cutting Surface*, J. of Materials Processing Technology, Vol. 141, 2/2003, pp. 213–218.

[6] CHEN, F. L., SIORES, E.: *The Effect of Cutting Jet Variation on Striation Formation in Abrasive Water Jet Cutting.* Int. J. of Machine Tools and Manufacture, Vol. 41, 10/2001, pp. 1479–1486

[7] KLESNIL, M., LUKAS, P.: *Fatigue of Metallic Materials under Mechanical Loading,* 1st ed., 224 p., 1975, Praha, Academia [in Czech].

[8] POLAK, J.: *Cyclic Plastic response and fatigue Life of Materials,* Key Engng. Materials, Vol. 348–349, 2007, pp. 113–116

[9] YUUTA, A., HIROSHI, N.: *Fatigue Limit Reliability of Axisymmetric Complex Surface,* Int. J. of Fracture, Vol. 131, 1/2005, pp. 59–78

[10] ITOGA, H., TOKAJI, K., NAKAJIMA, M., KO, H.-N.: *Effect of Surface Roughness on Step-Wise S-N Characteristics in High Strength Steel,* Int. J. of Fatigue, Vol. 25, 5/2003, pp. 379–385

[11] LEBAR, A., JUNKAR, M.: *Simulation of Abrasive Water Jet Cutting Process: Part 1. Unit event approach,* Modelling and Simulation in Materials Science and Engineering, Vol. 12, 6/2004, pp. 1159–1170

[12] NOVY, F., CINCALA, M., KOPAS, P., BOKUVKA, O.: *Mechanisms of High-Strength Structural Materials Fatigue Failure in Ultra-Wide Life Region*, Materials Science and Engineering, Vol. A 462, 2007, p. 189–192

[13] BOKUVKA, O., NOVY, F., CINCALA, M., KUNZ, L.: *Gigacycle Fatigue of Structural Materials (in Slovak)*, Acta Mechanica Slovaca, Vol. 10, 1/2006, pp. 53–58

Marian Bursak – Otakar Bokuvka *

FATIGUE PROPERTIES OF STEEL WITH INCREASED ATMOSPHERIC CORROSION RESISTANCE

The paper deals with the influence of cyclic loading (tension-compression, bending and torsion) on the course of the fatigue life and the fatigue limit of advanced low-alloyed strip steel with increased atmospheric corrosion resistance. The tested steel shows, besides very good mechanical properties ($R_e > 380$ MPa, $A_5 > 30\%$), also very good fatigue resistance and its fatigue limit/ultimate tensile strength ratio is above 0.5. These properties are provided by a favourable fine-grained structure of the tested steel.

1. Introduction

Low-carbon low-alloyed Cu-Cr-Ni-P steels serve as qualitatively higher substitution for classic structural materials able to form, under suitable atmospheric conditions, a coherent and very adhesive, aesthetic layer of corrosion products on its surface, which retards the corrosion process [1, 2]. For the effective utilization of these steels, the endeavour is to increase their utility properties by optimizing their chemical composition, as well as the strip production technology [3].

For the application of these steels, their resistance to cyclic loading – fatigue – is one of substantial requirements. The fatigue process is influenced by internal, as well as external factors. The internal factors are the function of the internal material structure. The external factors are related to the operational conditions of equipment. The environment has a significant influence, since corrosion accelerates the fatigue process even in case of steels with increased atmospheric corrosion resistance, although to a less extent than in case of classic steels [4].

The type of cyclic loading also significantly influences the fatigue process. Literature presents relationships between the fatigue limits of three basic types of cyclic loading (tension-compression, bending, torsion), which can generally be defined using the following equation

$$\sigma_{Co} = a \,.\, \sigma_C = b \,.\, \tau_C \qquad (1)$$

where σ_{Co}, σ_C, τ_C are bending, tension-compression and torsion fatigue limits. The a, b parameters are, besides the loading type, dependent on the internal material structure, but also on the test conditions. It generally applies that $\sigma_{Co} > \sigma_C > \tau_C$. For steels, $a = 1.3$ and $b = 1.75$ [5]. The stress distribution on the sample cross-section is different for different cyclic loading types and therefore the material non-homogenity (different structures on the surface and inside the part, residual stress, notch effects of the surface, etc.) influences the relationships between σ_{Co}, σ_C, τ_C [6].

The paper is focused on the assessment of the influence of the cyclic loading type on the fatigue life of sheets made of low-carbon low-alloyed steel with increased atmospheric corrosion resistance with higher utility properties. These sheets are used, among others, for products that are loaded in various ways during operation (e.g. ship transport containers).

2. Test material and methods

The fatigue tests were carried out on sheets made of low-carbon (C = 0.08%), low-alloyed (Al = 0.04%, Cu = 0.4%, Cr = 0.5% a Ni = 0.15%) steel with increased atmospheric corrosion resistance. The methods of determination of the chemical composi-

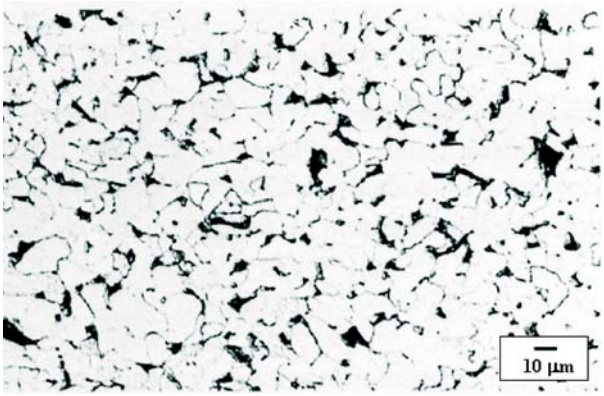

Fig. 1 Microstructure of tested steel

* **Marian Bursak[1], Otakar Bokuvka[2]**
[1]Department of Material Science, Technical University of Kosice, Slovakia, E-mail: Marian.Bursak@tuke.sk
[2]Department of Materials Engineering, University of Zilina, Slovakia

tion are described in [9]. As a result of controlled hot rolling, the structure observed using light microscopy is fine-grained, polygonal, ferrite-pearlite, with the occurrence of cementite mainly at the grain boundaries, Fig. 1.

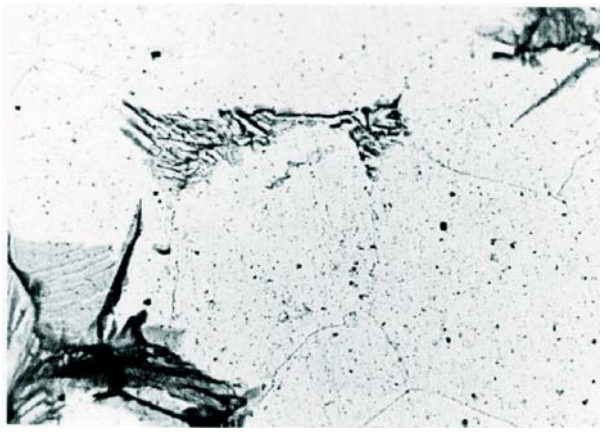

Fig. 2 Distribution of dispersed precipitate. Magnitude: 3000x

The mean ferrite grain size is approx. 10.5 μm and the pearlite share in the structure is approx. 10%. The precipitate is distributed relatively uniformly in the ferrite matrix, Fig. 2. This structure of the tested steel makes it possible to achieve very good mechanical, as well as fatigue properties. The basic mechanical properties of the tested sheets were determined using the tensile test and are listed in Tab. 1.

Basic mechanical properties of the tested steel — Table 1.

Sampling direction	R_e [MPa]	R_m [MPa]	A_5 [%]	Z [%]
L	384	501	31.8	71.5
T	390	498	28.7	63.3

As it results from Tab. 1, only deformation properties (A_5, Z) are reasonably influenced by the rolling direction – they are higher in the rolling direction (L).

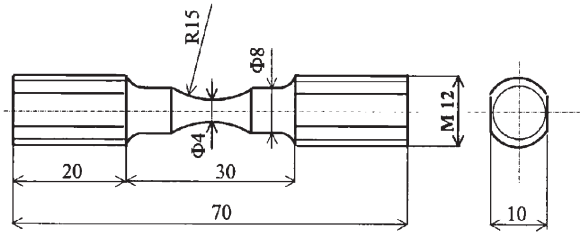

Fig. 3a Fatigue test bar for symmetric alternate tension-compression cyclic loading tests

Samples were taken from the tested strips in the rolling direction (L) and the transversal direction (T) and fatigue test bars were made for symmetric alternate tension-compression cycle tests (Fig. 3a), symmetric alternate torsion cycle tests (Fig. 3b) and symmetric in-plane bending tests (Fig. 4).

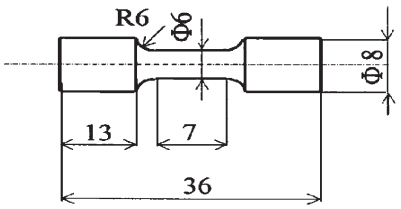

Fig. 3b Fatigue test bar for symmetric alternate torsion cyclic loading tests

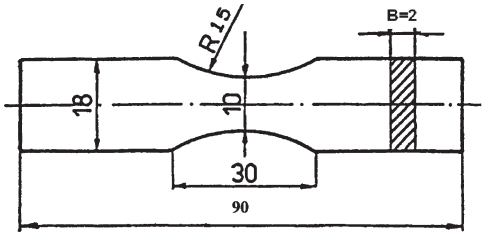

Fig. 4 Fatigue test bar for in-plane bending loading tests

The tension-compression fatigue tests were performed using a standardized performed procedure on the INSTRON 8511 pulsator at the frequency of approx. 27 Hz with the symmetric alternate cycle ($R = -1$), and the torsion and in-plane bending tests were executed on the PWOG fatigue machine with the symmetric alternate torsion and bending cycles ($R = -1$) at the frequency of 35 Hz. The limit number of cycles was $N_C = 10^7$ cycles, in accordance with the standard.

3. Test results and analysis

The fatigue test results were processed as the relationship between the upper stress σh and the number of cycles to failure N. For illustration, Fig. 5 shows the Wöhler curve of the tested steel for the L direction with the symmetric alternate tension-compression cycle and Fig. 6 shows this for the alternate torsion cycle.

The fatigue limits were determined from the horizontal line of the experimentally determined Wöhler curves and the results from the inclined line were statistically processed in the form of a regression relationship, $\log N = a + b.\sigma_h$, or $\log N = a + b.\tau_h$. The time fatigue limit with 50% probability of survival for the required number of cycles $N_p < 2.10^6$ can be calculated from these equations. Tab. 2 documents the measured fatigue characteristics of the tested steel.

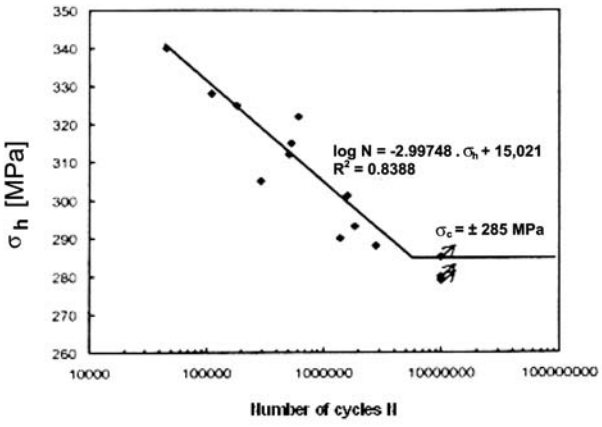

Fig. 5 Wöhler curve for symmetric tension-compression loading in the L direction

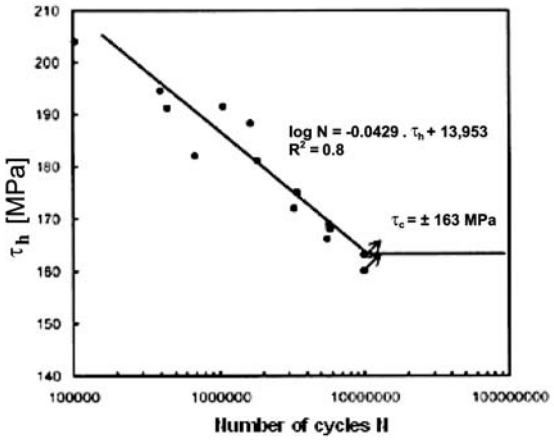

Fig. 6 Wöhler curve for alternate torsion loading in the L direction

Fatigue characteristics of the tested steel — Table 2.

Loading method	Sampling direction	*a*	*b*	σ_C [MPa]	τ_C [MPa]	σ_{Co} [MPa]	$\sigma_C(\sigma_{Co})/R_e$ τ_C/R_e	$\sigma_C(\sigma_{Co})/R_m$ τ_C/R_m
Tension-compression ($R=-1$)	L	−2.9975	15.021	± 285	–	–	0.7441	0.569
	T	−0.0222	12.218	± 275			0.7270	0.560
Torsion ($R=-1$)	L	−0.0429	13.953	–	± 163	–	0.4256	0.325
	T	−0.0295	11.642		± 162		0.4222	0.325
In-plane bending ($R=-1$)	T	–	–	–	–	261	0.7560	0.513

Tab. 2 shows that the σ_C/R_m ratio is more than 0.5, which indicates the above-standard utilization of the strength properties of the tested steel during fatigue tension loading. The favourable fatigue properties are the result of the structure of the tested steel, especially its fine grain, which, besides increasing the strength properties, significantly increased its elongation. The high σ_C/R_e ratio (0.72) also indicates good resistance of the tested steel in the low-cycle fatigue area.

The tested sheet was rolled in a unidirectional, controlled way, which was mainly reflected in the anisotropy of plastic properties. In the transversal direction, the elongation A_5 and the reduction of area Z were 10% lower than in the rolling direction. Since the fatigue failure resistance is an integral strength and plasticity property, the anisotropy of properties is also reflected on the fatigue limit value. The tension fatigue limit with the symmetric cycle in the *T* direction is approx. 3.5% lower than in the *L* direction. This anisotropy of plastic properties also influences the behaviour of material when the loading type is changed. The measured results brought the following relationship between the fatigue limits at the symmetric tension-compression, in-plane bending and torsion cycles:

$$\sigma_C = 1.05.\ \sigma_{Co} = 1.69 \cdot \tau_C\ . \qquad (2)$$

The σ_C/σ_{Co} ratio is influenced, among others, by various thicknesses of the input material, but also by the test bar shape (Fig. 4). The flat test bar edges are often the initiators of fatigue crack formation. On flat test bars, the fatigue properties are also significantly influenced by residual stress [4, 7]. Theoretically, the stress size and course at the symmetric tension-compression cycle and at the surface layers of the test bar at the symmetric in-plane bending can be considered as identical. Then the σ_C/σ_{Co} ratio will be dependent on whether the shape and the surface of the flat test bar or the lower tension stress under the surface during in-plane bending has a more significant effect.

The σ_C/τ_C ratio, because of different stress courses during tension and torsion, is influenced more significantly by the anisotropy of properties of unidirectionally rolled sheets. The effect of the loading method on the fatigue limit values is, among others, based on the strength properties of material and the σ_C/τ_C (σ_{Co}) ratio cannot be considered as a constant [8]. If we compare the fatigue limit values at the symmetric cycle in in-plane bending and torsion, which were tested on the same equipment, then $\sigma_{Co}/\tau_C = 1.6$. This ratio is in accordance with the mean ratios applicable to structural steels.

The tested strip steel with increased atmospheric corrosion resistance has, when compared with classic ferrite-pearlite COR-

TEN steels, higher strength and plastic properties, which were achieved through suitable production technology. The increased strength properties are the result of contributions from grain refinement and precipitation hardening, while fine grains eliminated the adverse effect of precipitation hardening on plasticity. These properties also provided an above-standard fatigue limit/ultimate tensile strength ratio, even when the cyclic loading type is changed. The tested steel has favourable fatigue properties even after long-term exposure to atmospheric corrosion [4].

4. Conclusion

The paper analyses the fatigue properties of fine-grained strip steel with increased atmospheric corrosion resistance at three basic loading types – tension, torsion and bending. Based on the experiments and their analysis, the following can be stated:

- The favourable mechanical properties (R_e, R_m, A_5, Z) of the tested steel, achieved mainly through grain refinement and precipitation hardening, are also reflected on their above-standard σ_C/R_m ratio.
- The favourable fatigue limit/ultimate tensile strength ratio is maintained also when the cyclic loading type is changed.
- The ratio between the fatigue limits at the above-mentioned cyclic loading types does not significantly differ from the values stated for structural steels. The results show that this ratio is also influenced (besides the material characteristics) by the shape of the used test bars.

References

[1] SEVCIKOVA, J. TITKOVA, K., SEVCIK, A.: *Corrosion and Prevention of Material,* vol. 44, 4/2000, p. 82
[2] KOCICH, J., SEVCIKOVA, J.: *Basic Problems of Steel Type COR-TEN Application*, Metal, vol. 99, Ostrava, 1999, p. 110
[3] KOLLAR, J., SIMON, A.: *Steel Sheets,* vol. 23, 1/1996, p. 19
[4] BURSAK, M., MICHEL, J.: Communications – Scientific Letters of the University Zilina, 4/2006, p. 38
[5] VECHET, S., KOHOUT, J., BOKUVKA, O.: *Fatigue Properties of Nodular Cast Iron (in Czech)*, Edicne stredisko Zilina, University of Zilina, 2002
[6] BURSAK, M., BOKUVKA, O.: Communications – Scientific Letters of the University of Zilina, 4/2006, p. 34
[7] MIHALIKOVA, M., KOVALOVA, K., MICHEL, J.: *Materials Engineering*, vol. 11, 3/2004, p. 13
[8] TOUSCHER, H.: *Dauerfestigkeit von Stahle und Gusseisen,* VEB Fachbuchverlag Leipzig, 1982
[9] RUZICKOVA, S.: *An Indian Journal*, vol. 6, 1/2007, pp. 17–26.

Jozef Janovec *

SIMILARITY BETWEEN EFFECTS OF LAVES PHASE AND M_6C IN ALLOY STEELS

The aim of this work is to summarize the experimental result obtained within the last two decades about the effects of Laves phase and M_6C during long-term thermal exposures of alloy steels. The intergranular Laves phase (12CrMoV steel) and/or M_6C (3CrMoV steel) particles were found to evoke the anomaly in the kinetic dependence of phosphorus grain boundary concentration. In comparison to other phases usually present in Cr-Mo alloy steels, Laves phase and M_6C precipitate after longer periods of annealing and dissolve non-metallic elements such as phosphorus or silicon. A partitioning of originally segregated phosphorus between the matrix and the newly precipitated Laves phase and/or M_6C particles led to the decrease in the phosphorus grain boundary concentration.

1. Introduction

In this paper some experimental results obtained within the last two decades are summarized and related to the role of Laves phase and M_6C in processes of phosphorus segregation in alloy steels on long-term thermal exposures. In the investigations coordinated by the author of this paper, light microscopy (LM), transmission electron microscopy (TEM), energy-dispersive X-ray spectroscopy (EDX), electron diffraction, and Auger electron spectroscopy (AES) were used.

2. Laves phase and M6C

The formula Fe_2Mo is usually used to characterize the Laves phase present in Cr-Mo alloy steels. This phase exhibiting hexagonal crystal structure [1] is isostructural with $MgZn_2$ (Table 1). It precipitates mostly in the form of discrete particles inside the δ-ferrite grains [2, 3] or in the form of foils along the boundaries of prior austenite grains in ferrite [4,5]. Particles of Laves phase precipitated in 12CrMoV steel (Table 2) after annealing at 773 K for times exceeding 10 000 h contain besides iron and molybdenum also chromium, silicon and phosphorus as illustrated by EDX-spectrum in Fig. 1. Laves phase was not identified in 12CrMoV steel after annealing for shorter times than 10 000 h at 773 K [6].

Parameters characterising crystal structures of Laves phase and M6C[1] Table 1

Parameter	Laves phase	M_6C
Pearson symbol	hP12	cF112
Strukturbericht designation	C14	$E9_3$
Space group	$P6_3/mmc$	Fd3m
Number of space group	194	227
Prototype	$MgZn_2$	Fe_3W_3C
Type (this work)	**Fe_2Mo**	**$(Fe,Mo)_6C$**

Parameters characterizing the crystal structure of M_6C are also given in Table 1. This carbide precipitates mostly in molybdenum and/or tungsten containing steels after long-term annealing [7]. The higher the bulk contents of molybdenum and/or tungsten the shorter the time preceding the M_6C precipitation [8]. M_6C forms mostly bulky foil-shape particles along the boundaries of prior austenite grains. The chemical composition of M_6C in Cr-Mo steels is very similar to that of Laves phase. As follows from EDX-spectrum in Fig. 2 [6], M_6C in 3CrMoV steel (Table 2) annealed at 853 K for 5 000 h contains silicon and phosphorus next to iron and molybdenum (dominant elements), as well as chromium and vanadium (minor elements). For identification of M_6C, electron

Mass contents of elements in investigated steels in %. Table 2

Steel	C	Mn	Si	Cr	V	Mo	Ni	P	S	N
12CrMoV	0.22	0.63	0.14	11.80	0.27	0.93	0.74	0.06	0.014	0.035
3CrMoV	0.13	0.32	0.22	2.49	0.25	0.41	-	0.04	0.004	0.005

* **Jozef Janovec**
Institute of Materials Science, Faculty of Materials Science and Technology, Slovak University of Technology, Trnava, Slovakia,
E-mail: jozef.janovec@stuba.sk

diffraction was used. M_6C was not found in the steels after annealing at 853 K for 1 000 h or for shorter times [6].

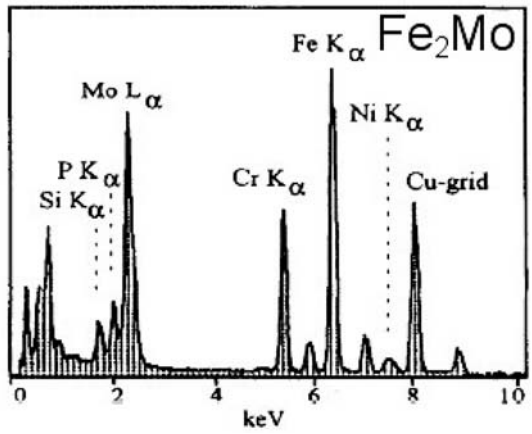

Fig. 1 EDX-spectrum of Fe2Mo particle present in 12CrMoV steel after annealing for 22 000 h at 773 K [5]

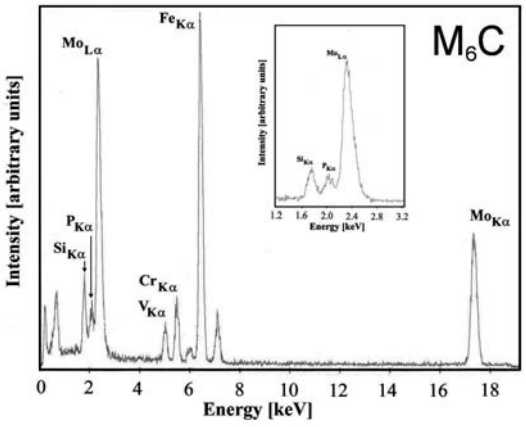

Fig. 2 EDX-spectrum of M6C particle present in 3CrMoV steel after annealing for 5 000 h at 853 K [6]

Both Laves phase identified in 12CrMoV steel [5] and M_6C identified in 3CrMoV steels [6] have some identical properties:

- they start to precipitate after longer annealing periods (Laves phase in 12CrMoV steel after 10 000 h at 773 K and M6C in 3CrMoV steels after 5 000 h at 853 K),
- molybdenum and iron dominate in chemical compositions of both phases,
- both the phases are able to dissolve silicon and phosphorus.

2. Segregation induced grain boundary precipitation of Laves phase and M6C

Laves phase and M_6C as Mo-rich phases in Cr-Mo alloy steels nucleate preferencially in areas with enhanced molybdenum concentration. Such areas are also grain boundaries, because molybdenum shows tendency to segregate in Fe-base materials [9]. The grain boundary segregation of molybdenum however can be strengthened by the phosphorus-molybdenum co-segregation when phosphorus is present in Cr-Mo steels. For 3CrMoV steel, the segregation enthalpy of molybdenum and the P-Mo interaction coefficient are -21 and -23 kJ.mol^{-1}[10], respectively. This gives evidence about a strong attractive interaction between phosphorus and molybdenum [11] and reduces a long incubation period exceeding the Laves phase and M_6C precipitation.

3. Reduction of phosphorus enrichment at grain boundaries due to the Laves phase and M6C precipitation

The appearance of the Laves phase and/or M_6C particles at the grain boundaries evokes the redistribution of originally segregated phosphorus between the matrix and the newly formed particles. It is because of the particle ability to dissolve phosphorus and silicon. Consequently, the grain boundary concentration of phosphorus starts to decrease because phosphorus entering Laves phase and/or M_6C particles diffuse intensively into the particle interior. Driving force of this process is effort of phosphorus to be distributed even across the particle [6]. After precipitation of Laves phase in 12CrMoV and M_6C in 3CrMoV steels, the grain boundary concentration of phosphorus starts to decrease. This is illustrated in Figs. 3 (for 12CrMoV steel) and 4 (for 3CrMoV steel).

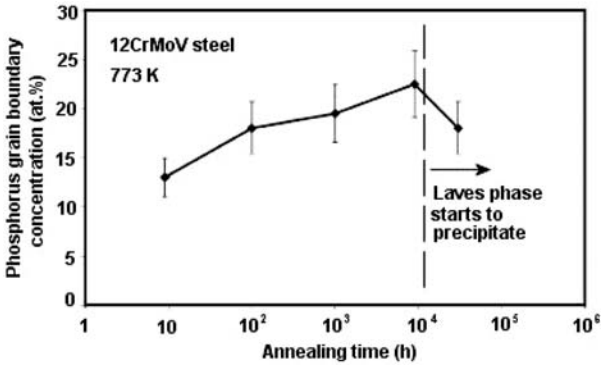

Fig. 3 Dependence of phosphorus grain boundary concentration on annealing time for 12CrMoV steel. Annealing was done at 773 K. Position of the maximum (10 000 h) correlates with start of the Laves phase precipitation.

Processes taking part in the investigated steels during annealing contribute to the anomaly in the kinetic dependence of the phosphorus grain boundary concentration. The anomaly, even if it appeared in different kinds of steels, shows the same nature and can be attributed to the same mechanism. The decisive assumption for applicability of this mechanism resides in the similarity of Fe_2Mo and M_6C phases. Specific behaviour of these phases in influencing the phosphorus grain boundary segregation in alloy

steels seems also to be interesting from the practical point of view. Changes in phosphorus concentration evoked by precipitation of the Fe_2Mo and/or M_6C phases should also show a direct impact on the steel intergranular brittleness. A study of the relationship between the phosphorus enrichment at grain boundaries and fracture toughness of alloy steels containing M_6C or Laves phase is therefore highly topical [12].

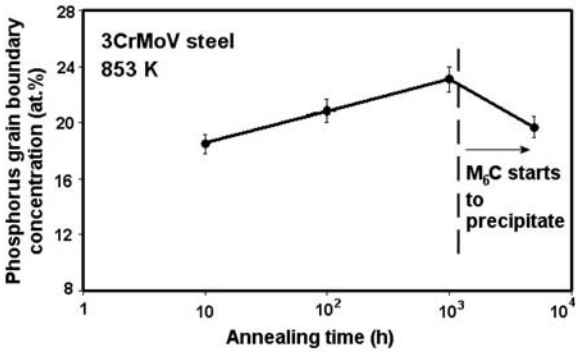

Fig. 4 Dependence of phosphorus grain boundary concentration on annealing time for 3CrMoV steel. Annealing was done at 853 K. Position of the maximum (1 000 h) correlates with probable start of the M6C precipitation.

4. Conclusions

It has been shown that the Laves phase and/or M_6C particles precipitating along the boundaries of prior austenite grains can evoke the anomaly in the kinetic dependence of phosphorus grain boundary concentration. This is due to the ability of both phases to dissolve non-metallic elements such as phosphorus or silicon. In comparison to other phases usually present in Cr-Mo alloy steels, Laves phases and M_6C precipitate after longer periods of annealing. A subsequent partitioning of originally segregated phosphorus between the matrix and the newly precipitated particles of Laves phase and/or M_6C leads to the decrease in the phosphorus grain boundary concentration.

References

[1] http://cst-www.nrl.navy.mil/lattice/index.html
[2] JANOVEC, J., SUSTARSIC, B., MEDVED, J., JENKO, M.: *Materiali in Tehnologije*, 37, 2003, 307–312
[3] PADILHA, A. F., ESCRIBA, D. M., MATERNA-MORRIS, E., RIETH, M., KLIMENKOV, M.: *J. Nuclear Mater.*, 362, 2007, 132–138
[4] JANOVEC, J.: *Nature of Alloy Steel Intergranular Embrittlement*, VEDA, Bratislava 1999
[5] JANOVEC, J., RICHARZ, B., GRABKE, H. J.: *Scripta Metall. Mater.*, 33, 1995, 295–300
[6] JANOVEC, J., VYROSTKOVA, A., SEVC, P., ROBINSON, J. S., SVOBODA, M., KRESTANKOVA, J., GRABKE, H. J.: *Acta Mater.,* 51, 2003, 4025–4032
[7] VYROSTKOVA, A., KROUPA, A., JANOVEC, J., SVOBODA, M.: *Acta Mater.*, 46, 1998, 31–38
[8] JANOVEC J., SVOBODA, M., VYROSTKOVA, A., KROUPA, A.: *Mater. Sci. Engn.,* A402, 2005, 288–293
[9] SEVC, P., JANOVEC, J., KATANA, V.: *Scripta Metall. Mater.*, 31, 1994, 1673–1678
[10] JANOVEC, J., GRMAN, D., MAGULA, V., PATSCHEIDER, J., LEJCEK, P., ŠEVC, P., BLACH, J.: *Journal of Surf. Anal., 5*, 1999, 294–297
[11] SEVC, P., JANOVEC, J., KOUTNIK, M., VYROSTKOVA, A.: *Acta Metall. Mater.*, 41, 1995, 251–258
[12] JANOVEC, J., JENKO, M., POKLUDA, J., VLACH, B., LEJCEK, P., SVOBODA, M., SANDERA, P.: *Mater. Sci. Forum*, 482, 2005, 191–194

Zdenek Jonsta – Petr Jonsta – Karel Mazanec *

MICROSTRUCTURAL MATERIAL ANALYSIS OF SUPERALLOY INCONEL 792-5A AFTER HIGH TEMPERATURE EXPOSITION

Aerospace industry often uses nickel superalloys for blades of jet engine turbines. The reason is that this material can satisfy numerous extreme requirements, such e.g. strength even at very high temperatures, resistance to fatigue damage, resistance to fatigue effect of combustion gases, etc. Long-term service life and material reliability is directly linked to its microstructure, or with its stability at long-term exploitation. Presented article deals with analysis microstructural material characteristics of cast variants nickel superalloy of INCONEL 792-5A type. Several strengthening mechanisms are applied in this type of superalloy. Principal mechanism is precipitation strengthening by coherent precipitates of intermetallic phase Ni_3Ti, or $Ni_3(Ti,Al)$.The analysis as such is based on evaluation of microstructural parameters by application of electron microscopy and chemical microanalysis.

1. Introduction

The paper is oriented on structural material analysis of cast nickel superalloy of the INCONEL 792-5A type after long-term annealing at temperature of 900 °C. From the viewpoint of practical exploitation this represents the upper limit of efficient use. Importance of solution consists in the fact that a higher level of alloying this type of superalloy has a higher level of segregation activity. At exploitation this fact can lead to the development of specific microsegregation processes related to a precipitation process and with formation either of carbidic phases, or some variants of intermetallic phases, e.g. of the γ′ type – (Ni3Ti, Al). In our case we applied annealing at the temperature 900 °C for 10^3 and 10^4 hours. For all practical purposes this represents conditions which have undoubtedly response from a technological practice viewpoint and can contribute both to a more objective evaluation of service life of relevant castings and also to the overall evaluation of microstructural stability [6, 8]

2. Experimental equipment

The testing material was after heat treatment to appropriate quality by the mode: 1120 °C/2h/air + 845 °C/24h/air long-term annealed at temperature of 900 °C for 1000 and 10 000 hours. Chemical composition of investigated material IN 792-5A is given in the following Table I.

For an objective evaluation of stability of this alloy it is necessary to know also the concentration of vacations $\bar{N}_v$ on a 3d sphere, which is in the given case 2.38. This value represents the level, which will apparently significantly participate in restriction of precipitation of intermetallic σ – phase.

Investigation of properties of evaluated samples was made on a microanalyser JCXA 733, which was equipped with an energy-dispersive analyser EDAX. Evaluation of microstructural characteristics was made in the mode of secondary electrons and bounced electrons (COMPO contrast). Individual coexisting phases were identified by quantitative EDX analysis. It must be, however, noted in this context that semi-quantitative X-ray microanalysis was performed only in case of particles larger than 1 μm, when results are not distorted significantly by X-ray signal from the surrounding matrix.

Microstructure of investigated samples was formed by a γ matrix, in which particles of intermediary phase γ′ precipitated [5, 7]. It is known from the existing results of analyses of investi-

Chemical composition of IN 792-5A (wt. %) Table 1

C	Mn(max)	Si(max)	Cr	Ti	Al	Fe(max)	B
0.06–0.10	0.15	0.20	12.0–16.0	3.75–4.20	3.15–3.60	0.50	0.010–0.020

Nb	Ta	Mo	W	Cu(max)	Co(max)	P(max)	S(max)	Zr	Ni
0.50	3.85–4.50	1.65–2.15	3.85–4.50	0.50	8.50–9.50	0.015	0.015	0.01–0.05	rest

* **Zdenek Jonsta, Petr Jonsta, Karel Mazanec**
VSB-TU Ostrava, Czech Republic, E-mail: zdenek.jonsta@vsb.cz

gated variants of heat treatment of high-alloyed Ni-superalloys that in case of application of two-stage heat treatment a bi-modal size distribution of particles of γ′ phase is detected. It was observed during a subsequent long-term exposition at temperature of 900 °C that this type of distribution is gradually eliminated. As for the above mentioned discussion and determination of the limit value $\bar{N}_v$, it is necessary to take into account the fact that during the long-term exposition a concentration of precipitates is being modified. The consequence is that even at the formal value $\bar{N}_v \approx 2.3$ the value $\bar{N}_v$ can be changed up to the level, for example, 2.5 and 2.6 at a formal constriction of the matrix.

Chemical composition of the γ′ phase with its certain variability corresponds to the intermetallics Ni_3(Ti, Al), whereas this phase dissolves a certain voluminal portion of Ta. Due to a higher segregation activity of Ni-superalloys it is also necessary to take into account the fact that there is a certain difference in the chemical composition of matrix in the area of dendrites and in inter-dendritic space. This means that the chemical constitution of intermetallic phase γ′ will be changing. It is worthwhile to remind that the preferential existence of Ni_3(Ti, Al) is to a certain extent linked to a compressibility of the matrix – a higher concentration of electrons in the 3d sphere and fulfilment of the requirement for low compressibility realisation as it corresponds to the condition for formation of the phase γ′ [9]. If the concentration of vacancies is higher due to addition of elements with a lower concentration of electrons it is possible to expect, as a result of development of possible compressibility, a formation of the phase with a higher range of specific volume in comparison with the inter-metallic phase γ′ (around 1%), namely formation of another type of intermetallic phase η, characterised as Ni_3X. This phase can be classified into the category of intermetallics γ″.

3. Basic microstructural analysis

Development of segregation processes during solidification of investigated nickel superalloy is accompanied by a formation of areas of a matrix with distinctly different chemical composition, which leads logically to a certain scatter in the finally formed microstructure. In this case a different variant of eutectics is formed in inter-dendritic areas, which is formed by a mixture of γ+γ′. In the areas of eutectics, which solidified as last ones, coarse particles of γ′ were formed. Fine shrinkage porosities were present in some cases in the neighbourhood of eutectic formations. Numerous carbides of the type MX, rich in Ta and Ti, precipitated in inter-dendritic areas. These particles often decorated the boundaries of γ grains. It is known that carbides of the type MX are unstable in nickel alloys and at higher exposition temperatures they gradually decay, which is accompanied by formation of the particles $M_{23}C_6$ and the phase γ′ [1]. MX particles were in investigated samples "wrapped" by a film of the phase γ′, the thickness of which increases with duration of annealing. Particles of Cr–Mo–W phase or formations of the phase, which is hexagonal phase of the type Ni_3X containing mainly Ti, Ta and Al, were present in proximity of some eutectic formations. Combination of elements in the phase rich in chromium (Cr-Mo-W) is typical for the phase M_6C, however, in the work [2] the particles of similar composition were identified by electron diffraction as borides of the type M_3B_2, or M_5B_3.

Occurrence of discontinuous netting of particles of the carbide MX and $M_{23}C_6$ was detected at the boundaries of γ – grains, which was surrounded by a film formed of the γ′ phase. Particles of the phase rich in Cr, or η – phases were observed at the grain boundaries only in very limited quantity. Positive is the fact that occurrence of phases such as σ – phase, μ – phase, *R* – phase, was not discovered in any variants of evaluated heat treatment [6, 10]. Very important is the fact that at superposed annealing at temperature 900 °C no reprecipitation occurred, consisting in dissolution of the old and formation of the new phase, nor any dissolution of some minority phases. Only processes of growth and coarsening of particles of the phases present in the structure already after duration of annealing of 10^3 hours were running. Apart from the above mentioned facts the particles of $M_{23}C_6$ after exposition at temperature of 900 °C for 10^4 hours precipitated in the form of inconherent chains in coarse particles γ′ in eutectics.

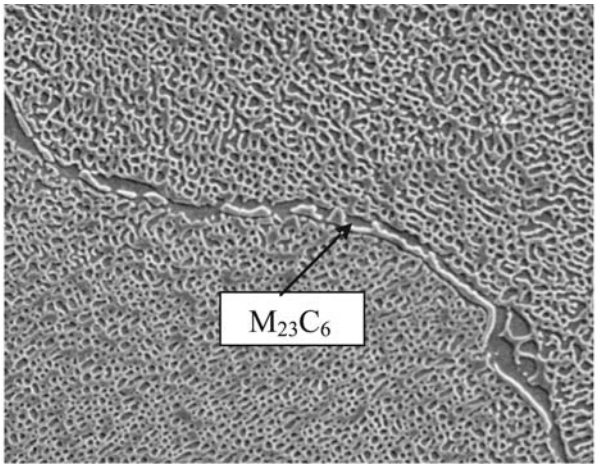

Fig. 1 Precipitation of $M_{23}C_6$ along grain boundaries surrounded by a film of the phase γ′, magn. 1800x

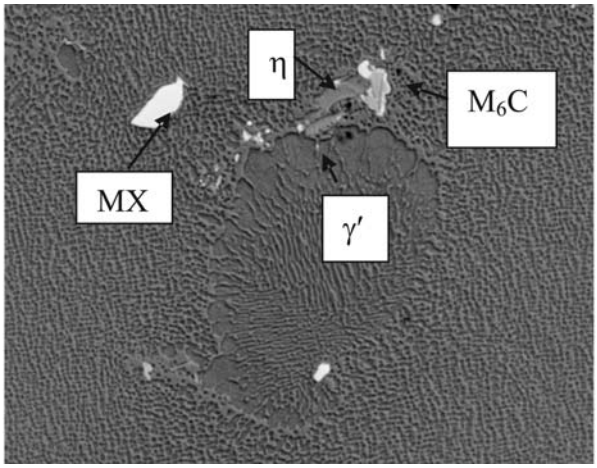

Fig. 2 Eutectics, MX, M_6C, of η phase, SEI, magn. 1700x

Examples of distribution of minority phases along grain boundaries and in proximity of the eutectics γ+γ′ are given in Figs. 1 and 2.

Precipitation is in most cases intergranular or it occurs on the grain boundary γ+γ′, which means a certain risk of initiation of degradation process [3, 4, 11]. Typical EDX spectra of individual minority phases are shown in Figs. 3–8.

4. Microstructural characteristics after various durations of exposition

On the basis of results of microstructural analysis of the investigated nickel superalloy after the relevant exposition durations of isothermal annealing, namely 900 °C/1000 hours and 900 °C/10000 hours, it can be stated that microstructure shows in many cases a specific behaviour. This is manifested by occurrence of various morphologically different variants of minority phases. In the men both in the mode of secondary electrons (SEI), as well as in the mode of bounced electrons (BEI). Two sets of measurement were realised for each variant.

In case of the first variant of heat treatment after 1000 hours of exposition precipitation of γ′ – phase on the boundaries of γ – grains or at the phase interface was mostly detected (see Figs. 9 and 10).

Moreover precipitated phases were evaluated by EDX analysis, namely the phases MX, phases rich in Cr, γ′ (Ni_3Ti, Al) and chemical composition of matrix was determined. In case of the analysis of chemical constitution of the phase MX a big difference

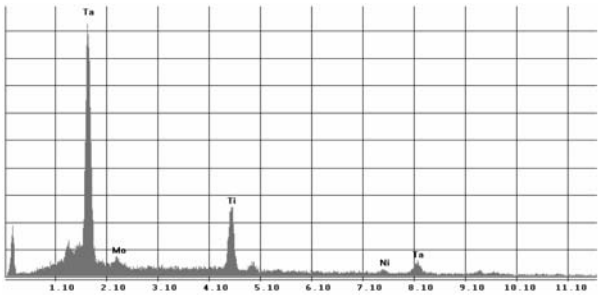

Fig. 3 EDX spectrum of the MX phase

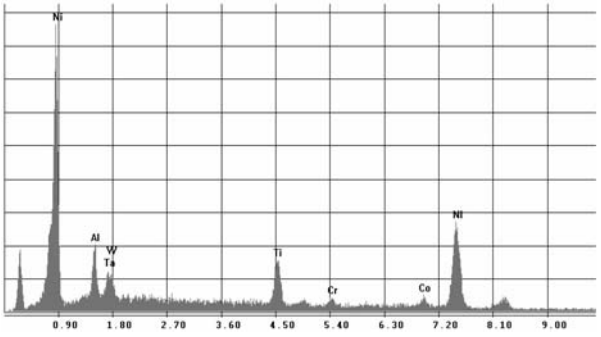

Fig. 4 EDX spectrum of the phase $Ni_3(Al,Ti)$

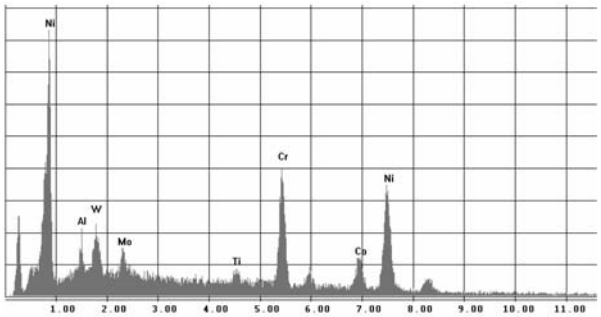

Fig. 5 EDX matrix spectrum

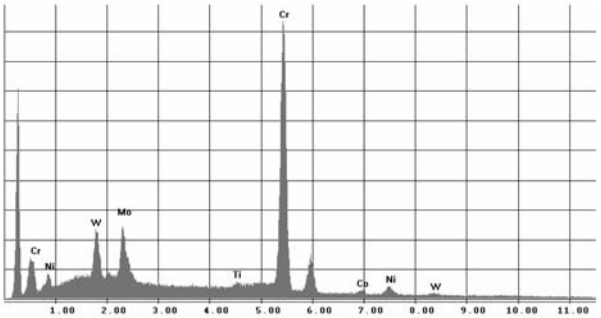

Fig. 6 EDX spectrum of the phase $M_{23}C_6$

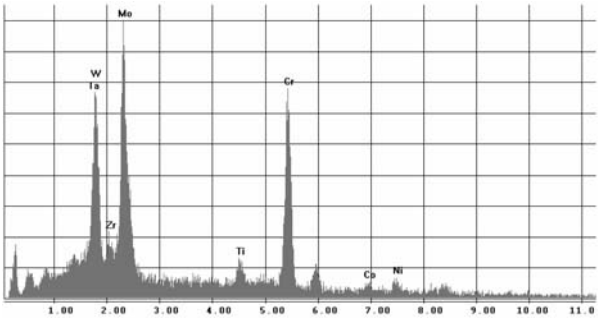

Fig. 7 EDX spectrum of the phase rich in Cr

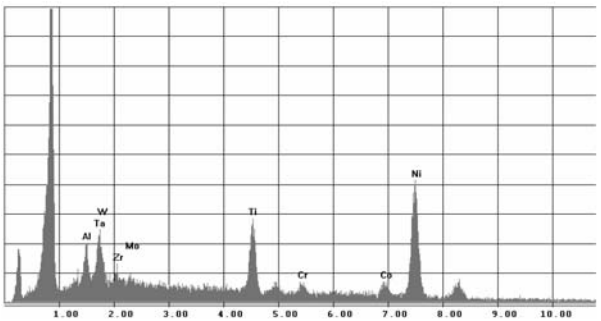

Fig. 8 EDX spectrum of the phase Ni_3Ti

in contents of Ta and Ti was detected. In one case the average contents of Ta was around 75 %, while in the second case it was around 48 %, which is approx. 60 % of the contents determined in the first case. Similar relation was observed also in the case of Ti, which usually acts together with Ta within their coexistence. In the first set of measurements the content of Ti was around 20%, in the second set it was around 45 %. This means that at higher content of Ta the content of Ti was lower. In the second set of measurements the relation of content of these two elements in the phase MX was inverse.

Selected cases of precipitation after the second variant of heat treatment by the mode 900 °C/10000 hours are presented in Figs. 11 and 12.

Special attention was paid also to a chemical analysis – mapping of distribution of individual elements forming the material constitution. In these context distributions of Ni, Ta, Cr, Al, Ti and Mo were investigated. In our opinion intensity of selectively evaluated precipitates slightly increased. The matrix is characterised by a very favourable level of uniform distribution of majority of investigated alloying elements. In connection with solution of microstructural response of the matrix a secondary precipitation was observed of the carbide $M_{23}C_6$ decorating the grain boundaries of the matrix. Results of the MX phase evaluation show a distinct mutual substitutability of Ta and Ti. Reduction of Ta leads to an increase of Ti in this phase and vice versa. It can be generally stated that sum of the content of Ta and Ti gives the overall level of the content of these two elements of approx. 90 %. Chemical composition of the phase Ni_3 (Ti, Al) is of a conventional character. It is only appropriate to mention that in case of the lower sum of Ti and Al in this phase a slightly higher content of Ta was observed. In investigated cases the same level of the sum of Ti, Al and Ta was observed, namely approx. 25 %, which can be considered as a certain

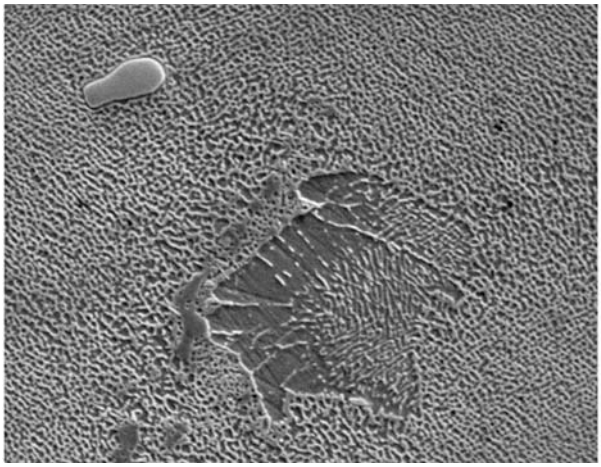

Fig. 9 Precipitation of γ′ – phase on the boudaries γ – grains after 1000 hours exposition, SEI, magn. 2200x

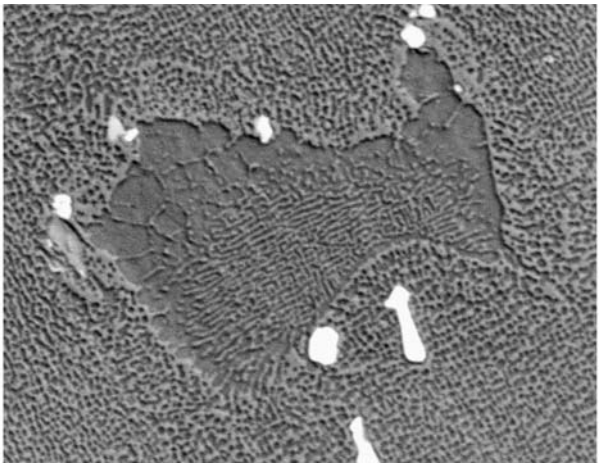

Fig. 10 Precipitation of γ′ -- phase at the phase interface after 1000 hours exposition, BEI, magn. 1800x

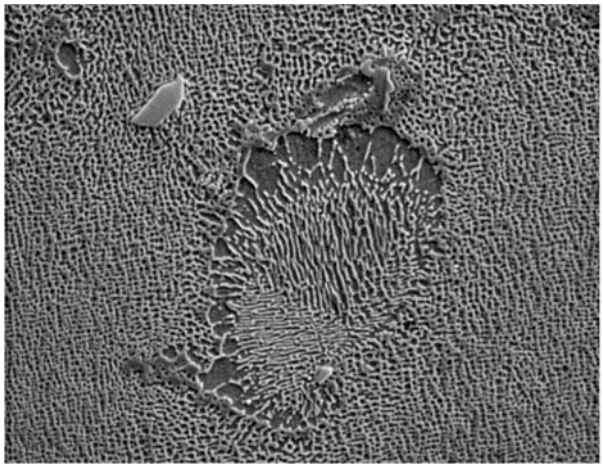

Fig. 11 Precipitation of minority phases after 10000 hours exposition, SEI, magn. 2200x

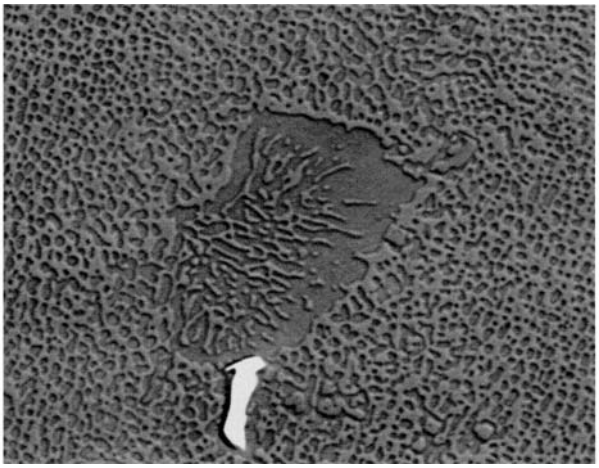

Fig. 12 Precipitation of minority phases after 10000 hours exposition, BEI, magn. 1700x

orientational criterion. The data about chemical composition of the matrix are comparatively surprising, since in one case the content of Ta was determined to be approx. 10 %, while in the second case it was much lower, namely approx. 3.3 – 3.4 %. In this case also a phase rich in Cr was detected, whereas the most important role in chemism of this phase is played by a mutual relation between Cr, W and Mo. Mo content was in both investigated cases detected essentially as constant, specifically around 25–29 %. In case of a higher content of W in this phase the content of Cr was lower, on average around 25 %, while at a lower content of W (around 8 %) the Cr content achieved the value of approx. 40%. As for mutual relation between Ta and Ti, a certain substitutability was discovered in this case too, although obviously at a lower level than in case of MX particles.

5. Conclusion

The paper summarises basic data about structural-phase characteristics of complex alloyed Ni-superalloy INCONEL 792-5A after high temperature exposition at temperature of 900 °C for 10^3 and 10^4 hours. Apart from the basic microstructural characteristics and monitoring of potential places for formation of a minority phase, an EDX analysis of the possible chemism of precipitated minority phases was performed as well.

Redistribution of atoms of alloying elements in the formed coexisting phases was also analysed. In many instances certain mutual substitutability of alloying elements was observed, which represents an important technical parameter and physical engineering basis for estimation of the type of precipitating phases, as well as for estimation of possible stability of the given Ni-superalloy.

Acknowledgement

This work was realized the support of research projects No. FI-IM5/001, No. FT-TA3/072 (Ministry of Industry and Trade) and project No. MSM 619890013 (Ministry of Education of Czech Republic).

References

[1] ROSS, E. W., SIMS, C. T.: *Superalloy II*, John Wiley and Sons, 1987, 97.
[2] SEO, S. M. et. al.: *Met. and Mat.* Transactions, 38A, 2007, 883.
[3] KOIZUMI, Y., KOBAYASHI, T. et. al.: *High Temp. Mat. for Power Eng.,* P.II, Liege,1998.
[4] SAUNDERS, N. et. al.: *Modeling the Material Properties and Behaviour of Ni-based Superalloys,* Superalloys 2004.Ed.Green et.al., TMS, Warendale,2004, 849.
[5] HERNAS, A., JONSTA, Z.: *Heat resisting steels and alloys (in Czech)*, ZUSI Zilina, 2002, 392 s.
[6] VODAREK, V.: *Physical Metallurgy of Modifications (9–12)% Cr Steels (in Czech)*, VSB – TU Ostrava, 2003, 163 s.
[7] GOLDSCHMIDT, D.: *Proc. Conf. Mat. For Advanced Power Eng.*, P.I., Liege, 1994.
[8] SHAO, CH., LI, J., ZHAO, M., LI, W., WU, J., KONG, S.: *In: Mater. for Advanced Power Eng.,* Vol. 53, Part I, Liege, 2006, pp. 555–560.
[9] LI, Y.L., YUAN, C., GUO, J.T., HOU, J. S.: *In: Mater. for Advanced Power Eng.,* Vol. 53, Part I, Liege, 2006, pp. 339–401.
[10] CHEN, Q.Z., JONES, C.N., KNOWLES, D. N.: *Mat. Sci. Eng.* A385, 2004, pp. 402–418.
[11] CONNOLLEY, T., REED, P.A.S., STARINK, M. J.: *Met. Sci. Eng.* A 343, 2003, pp. 139–154.

J. Kunz – K. Dalikova – V. Cihal *

BASIS FOR OPTIMAL CHOICE OF HIGH ALLOYED STRUCTURAL MATERIALS USED IN CHEMICAL AND POWER INDUSTRY

Six types of high alloyed structural materials widely used especially in power and chemical industry were under study. The experimental programme was focused on the research of materials resistivity against high aggressive media and time variable loading. The paper summarizes results of slow-strain rate test, electrochemical measurements (by means of potentiodynamic method, electrochemical noise measurement and electrochemical impedance spectroscopy) and fatigue test. The investigation was completed by fractographic analysis of failed test specimens. Detailed photo-documentation of specimen fractures was obtained by means of scanning electron microscopy.

Keywords: stainless steels, nickel alloys, corrosion and fatigue testing, SCC.

1. Introduction

Corrosion causes the economy of all countries huge claims every year. These losses are especially due to the extraordinary costs of anticorrosive protection and its maintenance, repairs of early cracked facilities, etc. Also the subsequent losses are very essential, e.g., energy loss, materials loss caused by uneconomical applications or as a result of poor knowledge of corrosion. The corrosion losses re-counted as a share of the gross national product are around 4 % [1]. These days, the metal corrosion losses of the Czech Republic can be estimated up to 100 billion CZK per year. Besides the economic losses, it is necessary to emphasize the ecological consequences (e.g., the endangering of the environment due to the aggressive medium escape out of the rusted pipeline), health threat, and endangering the human lives as well. In many cases, the fact that the corrosion is the primary cause of the accident remains undetected.

The experimental programme, the results of which are summarized in the paper, was focused on six types of very noble high alloyed materials: two duplex stainless steels, two austenitic stainless steels, and two nickel alloys. These alloys are often used in power, chemical, and food-processing industries. The aim of the study is to verify the most important characteristics quantifying corrosion resistivity especially in media containing chloride ions, and the fatigue properties of the above mentioned materials [2].

2. Investigated Materials

All corrosion-proof materials under study, i.e., duplex stainless steels X2CrNiMoN 22-5-3 (Uranus 45N) and X2CrNiMoCuN 25-6-3 (Uranus 52N+), austenitic stainless steels X1CrNiMoCuN 25-25-5 (Uranus SB8) and X1NiCrMoCuN 25-20-7 (Uranus B26), and nickel alloys X1NiCrMoCu 32-28-7 (Nicrofer 3127hMo) and NiCr23Mo16A1 (Nicrofer 5923hMo) were delivered in the form

Chemical composition of the alloys under study [3] Tab. 1

Alloy	C	Si	Mn	Ni	Cr	Mo	Cu	N	V	W
UR 45N	0.026	0.356	1.343	5.070	21.800	3.130	–	0.172	–	–
UR 52N+	0.015	0.335	1.130	6.020	24.900	3.740	1.650	0.248	–	–
UR SB8	0.010	0.246	0.936	25.900	25.050	4.730	1.450	0.214	–	–
UR B26	0.009	0.220	0.880	24.750	20.400	6.300	0.860	0.198	–	–
Nicrofer 3127hMo	0.008	0.040	1.510	31.050	26.650	6.340	1.160	0.207	–	–
Nicrofer 5923hMo	0.007	0.040	0.150	60.900	22.500	15.500	0.010	–	0.150	0.010

* **J. Kunz[1], K. Dalikova[1,2], V. Cihal[2]**
[1]Department of Materials, Faculty of Nuclear Sciences and Physical Engineering, Czech Technical University in Prague, Prague 2, Czech Republic, E-mail: jiri.kunz@fjfi.cvut.cz
[2]SVUOM Ltd., Prague 6, Czech Republic

of blank sheets between 4.5 and 10 mm thick. In the text below, the abbreviation UR will be used for the alloys type of Uranus. These sheets were heat treated by solution annealing at about 1050 °C and subsequent rapid water cooling. The microstructure

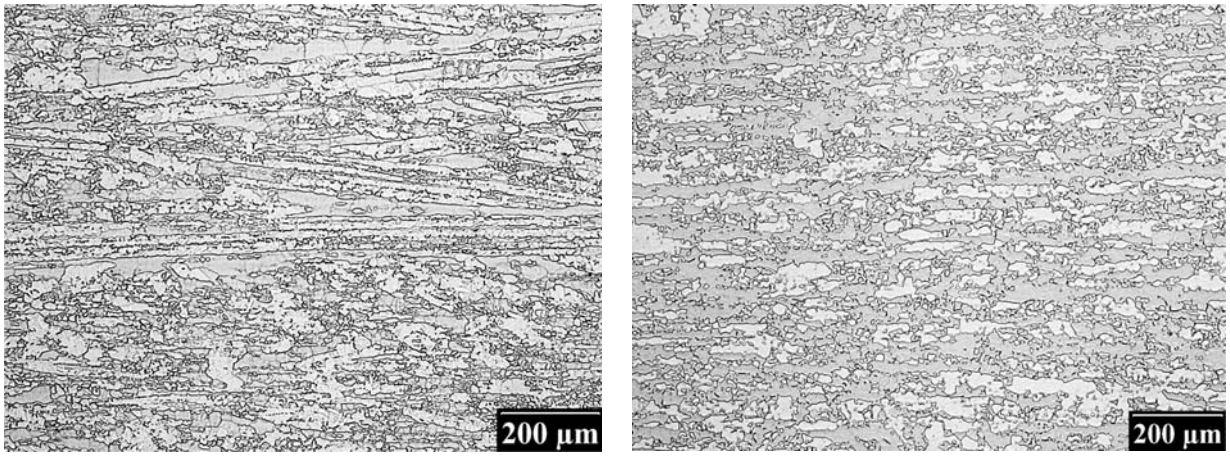

Fig. 1 Microstructure of duplex steels – Uranus 45N and 52N+

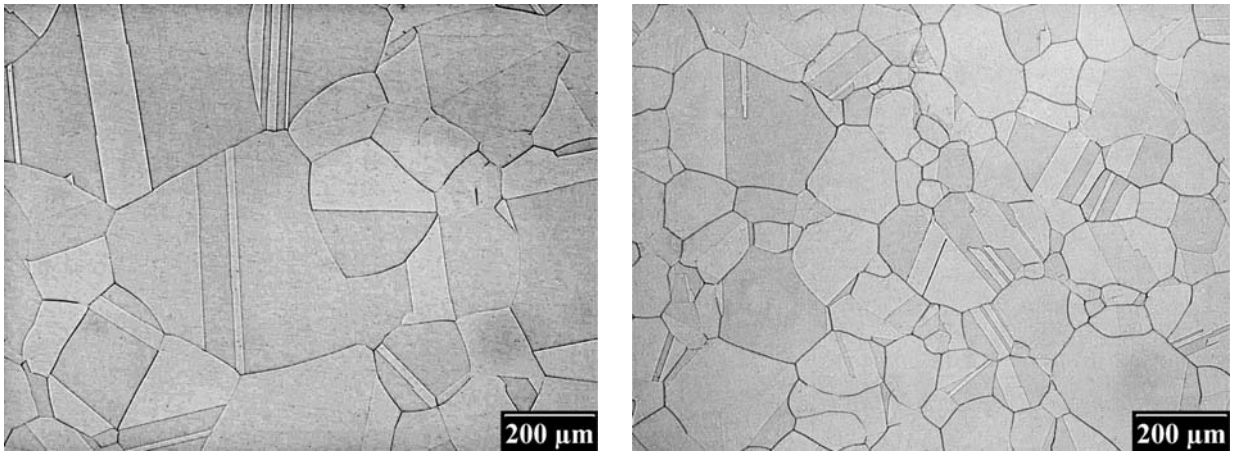

Fig. 2 Microstructure of austenitic steels – Uranus SB8 and B26

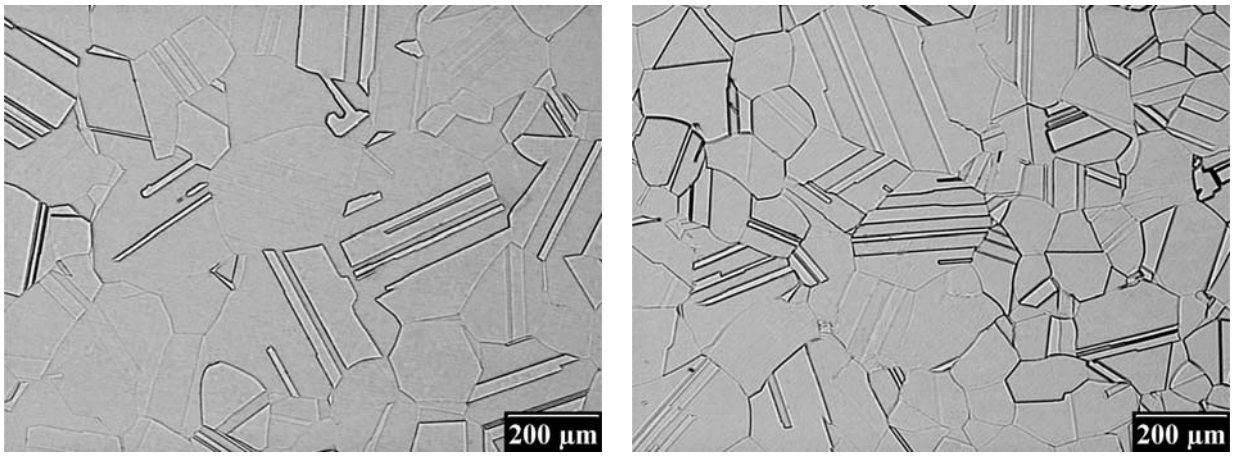

Fig. 3 Microstructure of nickel alloys – Nicrofer 3127hMo and Nicrofer 5923hMo

of the materials studied by means of light microscopy is documented in Figs 1–3. In comparison with both austenitic steels and Ni-alloys, the microstructure of duplex steels is much more fine.

The chemical composition, PRE_N (Pitting Resistance Equivalent Number) and mechanical properties (i.e., yield strength $R_p0.2$ and ultimate tensile stress R_m) of the alloys under study are summarised in Tabs 1 and 2. For this purpose, the following modified formula for PRE_N calculation was used [9]:

$$PRE_N = \mathrm{Cr} + 3.3(\mathrm{Mo} + 0.5\mathrm{W}) + 16\mathrm{N}.$$

PRE_N and mechanical properties of the alloys under study [3] Tab. 2

Alloy	PRE_N	Mechanical Properties		
		$R_p0.2$ [MPa]	R_m [MPa]	$R_p0.2/R_m$
UR SB8	44	300	600	0.50
UR B26	44	320	700	0.46
UR 45N	35	515	700	0.74
UR 52N+	41	560	800	0.70
Nicrofer 3127 hMo	51	348	734	0.47
Nicrofer 5923 hMo	74	429	771	0.56

3. Corrosion Testing

The resistivity to mechanical stress in aggressive media was investigated by *slow strain rate test (SSRT)*. Cylindrical test specimens with a diameter of 2 mm and working part length 10 mm were used. The corrosion media used in the experiments ($CaCl_2$, $CaCl_2 + FeCl_3$, ASTM G28B and the so called "green death" [3]) were selected with respect to the use of these alloys in practice. For comparison, the same tests were carried out in an inert medium (glycerol). Overall, 38 specimens were loaded at strain rate $2.56 \cdot 10^{-6}$ s^{-1} and elevated temperature $T = (60 \div 120)$°C. The time to the specimen failure and corresponding maximum load were observed. As an example of the *SSRT* results, the stress at the specimen failure σ_{max} (relative to the original cross-section) for all alloys under study in various media is presented in Fig. 4. Considerable decrease in σ_{max} due to aggressive media influence is evident especially for both duplex steels, while corrosion resistivity of Nicrofer 5923 hMo is superb even in the most aggressive media, i.e., ASTM G28B and "green death".

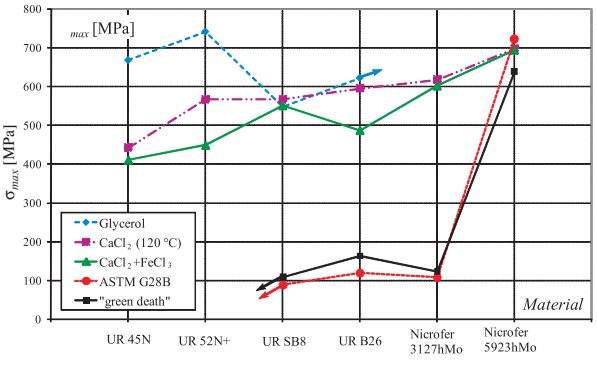

Fig. 4 Maximum stress at specimen failure vs. material in various corrosion media at SSRT

One of the electrochemical methods widely used in laboratory practise is *potentiodynamic measurement*, during which the current response as a function of continuous changes in potential is monitored. Some results of the experiments for austenitic and duplex steels under study tested in 1 mol/l NaCl have been presented previously by Lasek [3].

The *electrochemical impedance spectroscopy (EIS)* is a powerful tool for examining many chemical and physical processes in solutions as well as in solids. By means of this method, it is possible to determine both the range of materials surface damage in terms of the measured change of its impedance and the corresponding electrochemical reactions of the investigated corrosion process.

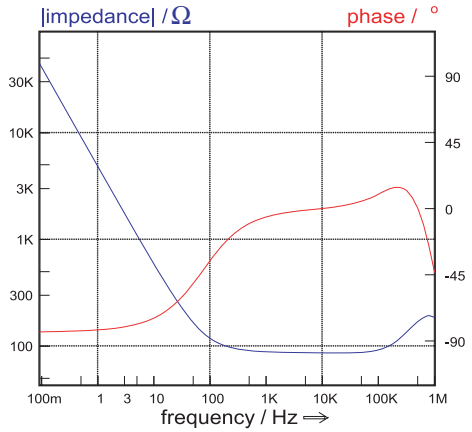

Fig. 5 Bode plot - Uranus B26

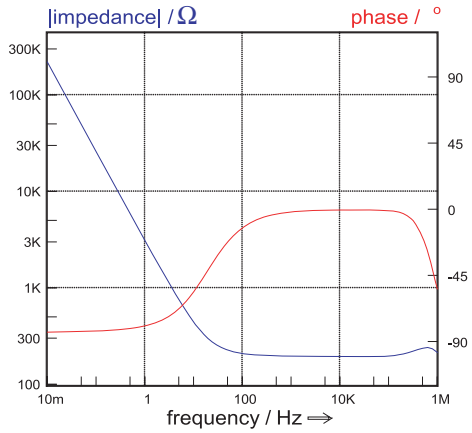

Fig. 6 Bode plot - Uranus 45N

Depending on the shape of the *EIS* spectrum, a circuit model or circuit description code and initial circuit parameters are assumed and input by the operator. Some of the results from *EIS* measurements are presented in Figs 5 and 6 for austenitic steel UR B26 and duplex steel UR 45N in the form of the so called Bode plots. By means of *EIS*, the very good stability of passive layers on the surface of studied materials was proved [5].

The real metal surface with structural defects and chemical inhomogeneities does not establish a true stationary state under a constant value of potential or corrosion current. By using of the sensitive *electrochemical noise analysis (ENA)*, it is possible to evaluate the fluctuations that are the result of instantaneous flow of charge between cathodic and anodic reaction sites. For classification of the character and intensity of the running corrosion processes, the frequency and amplitude of the developed electrochemical noise is analysed. The aim of this experiment is to detect the occurrence of localized corrosion attacks (pitting or crevice corrosion, stress corrosion cracking). *ENA* measurements were carried out in 6 % $FeCl_3$ (according to ASTM G48–76 [4]) at $T = 70 \div 85$°C for the all alloys under study [6] – see Fig. 7. During the experiment, the potential E_{SCE} vs. time t was monitored. This relation gives an objective basis for examining how long the material can survive in this solution (corresponding high potential) before it breaks (drop to the low potentials). From the character of the curves presented in Fig. 7, very good corrosion resistivity of both Ni-alloys is evident.

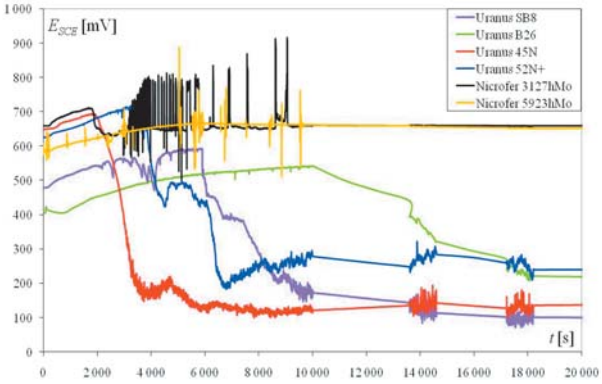

Fig. 7 Results of electrochemical noise analysis of six alloys under study presented in the form of potential E_{SCE} as a function of time t

4. Fatigue Testing

By means of servo-hydraulic machine INOVA ZUZ 50, the fatigue tests of CT-specimens (width $W = 38$ mm, length $L = 45.6$ mm and thickness $B = 4$ mm) at constant stress range were carried out. The fatigue crack growth direction was perpendicular to the rolling direction of material sheets. Initial notch in the specimens was extended and sharpened by electro-spark method. The fatigue tests were carried out at room temperature, at stress ratio $R = 0.1$ and loading frequency $f = 10$ Hz. The crack length vs. the number of applied cycles was monitored simultaneously by both optical and potential method during the fatigue testing. The data obtained were statistically processed into the form of the fatigue crack growth rate $v = da/dN$ as a function of the stress intensity factor range ΔK. The best fitted curves for all six materials under study in the Paris region are presented in Fig. 8.

One set of the specimens was tested until the final fracture. These specimens were subjected to detailed fractographic analysis focused on the study of fatigue failure mechanism. The fatigue tests of the second set of specimens were terminated at the moment the crack of a length of about $a = 21.5$ mm was extended; these CT-specimens will be used for corrosion test at constant load.

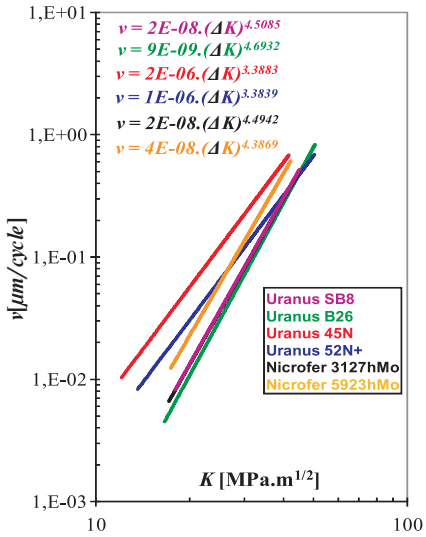

Fig. 8 Results of fatigue tests: crack growth rate v vs. stress intensity factor range ΔK in Paris region for six high alloyed structural materials

5. Fractographic Analysis

The investigation of degradation processes was completed by fractographic analysis of the failed SSRT and fatigue specimens [3]. Fracture micromorphology was studied by means of scanning electron microscope Jeol JSM 840A. The aim of the analysis was to determinate the failure and/or corrosion/fatigue mechanisms, the degradation process type, etc.

By means of qualitative fractographic analysis of fatigued CT-specimens, it was found that the process of fatigue failure could be divided into 3 phases:

- initiation of the fatigue crack in notch root (Fig. 9a),
- transcrystalline propagation of the fatigue crack mainly by striation mechanism (Fig. 9b),
- ductile transcrystalline final fracture (Fig. 9c).

In the lower ΔK range, the cleavage facets were also observed on the fatigue fracture surface of specimens of austenite materials (Fig. 9d) [7].

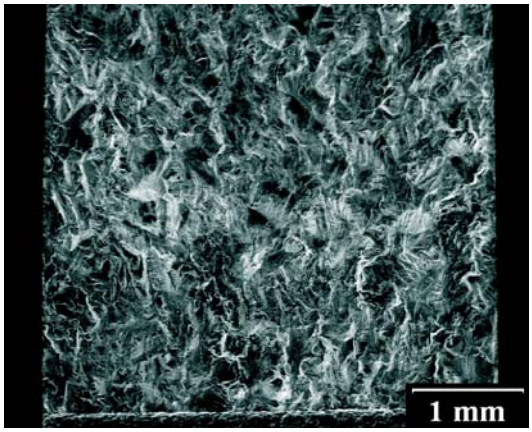

a) fatigue crack initiation

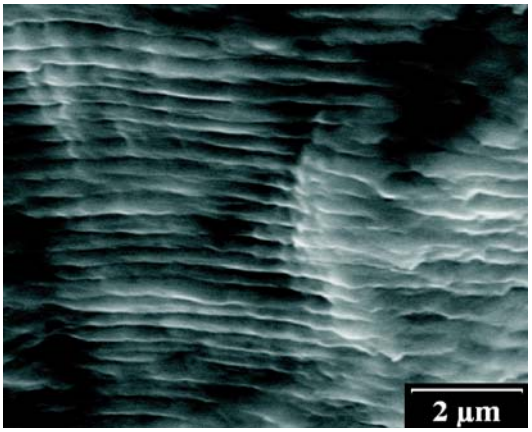

b) transcrystalline ductile striations

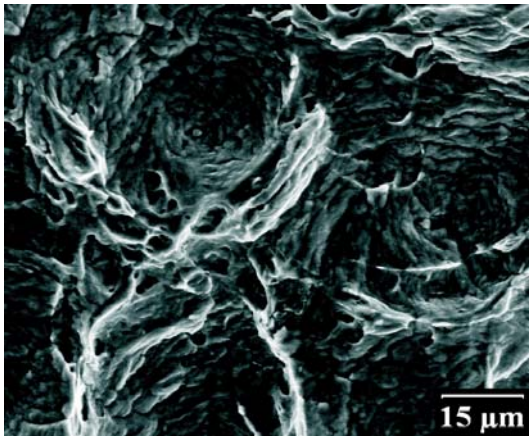

c) transcrystalline ductile final fracture

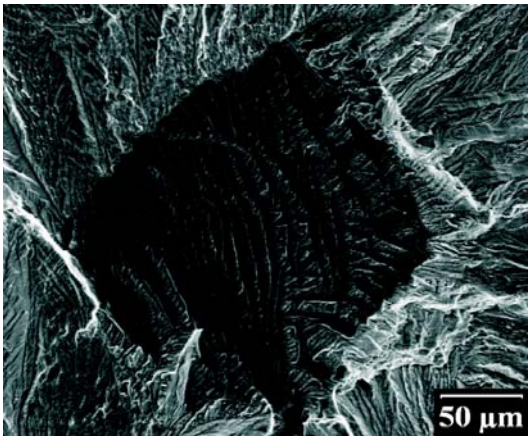

d) cleavage facet in fatigue fracture part

Fig. 9 Austenitic steel Uranus SB8 – typical fracture features of fatigued specimen

6. Results and conclusions

The study of degradation processes in six very noble high alloyed materials used mainly in power and chemical industry was carried out. These alloys differ from each other not only by corrosiveness, static mechanical characteristics, and fatigue resistance, but also by their price. The optimal choice of structural material depends on the specific requirements given by corresponding exploitation conditions and user possibilities.

A summary of our substantial experimental results and retrieval information is given in Tab. 3. In this table, four characteristics are evaluated:

a) ratio yield strength $R_p0.2$/ultimate tensile stress R_m (important performance factor in material specifications, design codes and structural integrity analysis methods),
b) corrosion resistivity in very aggressive media containing chloride ions (based especially on the results of slow strain rate test and electrochemical noise analysis),
c) fatigue endurance in the crack growth period (important factor in the concept of damage-tolerance or fail-safe structure components),
d) material price given especially by the price of alloying elements (Mo, Ni, Cr) on the market at the beginning of 2008.

In Tab. 3, the above mentioned characteristics classified by means of the alloy rank within the material group under study (number 1 represents the best alloy according to the given criterion, number 6 refers to the worst one) are supplemented by some practical output notes. It does not mean that the high alloyed material with excellent corrosion resistivity has also, e.g., excellent fatigue properties, i.e., time variable mechanical loading endurance, etc. The presented data represent an objective information basis for the optimized selection of a suitable structural material for specific applications and they identify some limitations from both the engineering and economic point of view.

Acknowledgement

This research has been supported by reserch project MSM6840770021. Special thanks also to OAD for financial support.

Summary of main experimental results obtained, economic aspects and practical outputs for six high alloyed materials under study Tab. 3

Material	Elastic power supply	Corrosion Properties*	Fatigue Properties	Price	Recommended Application [8]
UR SB8	4	4	2 ÷ 3	3	Process equipment for all but strong reducing and hot sulphuric acids; piping and heat exchangers handling ambient seawater; FGD absorbers and paper bleach equipment operating at moderate Cl-pH-T conditions.
UR B26	6	3	1	4	
UR 45N	1	6	6	1	Pressure vessels, piping, pumps and valves where strength and weight are factors along with resistance to stress corrosion and fatigue; general purpose heat exchanger tubing.
UR 52N+	2	5	4 ÷ 5 **	2	
Nicrofer 3127 hMo	5	2	2 ÷ 3	5	FGD systems; fine chemicals synthesis, phosphoric acid production; organic acids and esters synthesis; waste sulphuric acid recovery; petroleum production and refining sulphuric acid coolers.
Nicrofer 5923 hMo	3	1	4 ÷ 5 **	6	Components inorganic processes in volving chlorides; digesters and bleaching plants in the pulp and paper industry; scrubbers, reheaters; dampers; FGD systems; equipment and components in sour gas service.

Notes:
FGD -FlueGasDesulphurization
*) Corrosionpropertieswere evaluatedintermsof ENA and SSR T resultsinvariouscorrosionmedia withdifferentnumber of Clions (e.g., $CaCl_2$, $CaCl_2$ + $FeCl_3$, "greendeath",ASTM G28B)atelevatedtemperatures105 ÷120 °C.
**) Fatigue properties are markedly depending on ΔK.

References

[1] ANON.: *Fracture Costs US Industry $119 000 Million Every Years.* Int. J. Fatigue, 5, 3/1983, p. 176.
[2] *Stainless Steel Grades. Creusot-Loire Industrie* (Creusot-Marrel) - promotional material.
[3] DALIKOVA, K., KUNZ, J., CIHAL, V.: *Stress Corrosion Cracking at Slow Strain Rate Test of High Alloyed Ni-Cr-Mo Steels and Nickel Alloys,* Proc. of 1st Int. Conf. Corrosion and Material Protection. SVÚOM Praha 2007, p. 6, (CD ROM).
[4] LASEK, S.*: Pitting Corrosion of High Alloyed Stainless Steels (in Czech)*, Dissertation thesis, Ostrava 1999, p. 126, VSB-TU Ostrava.
[5] SILVERMAN, D. C., KENDIG, M.W., SCULLY, J., Eds.: *Electrochemical Impedance: Analysis and Interpretation,* ASTM STP 1188, ASTM 1993, p. 471.
[6] DALIKOVA, K., LINHARDT, P., CIHAL, V., KUNZ, J.: *Corrosion Testing of High Alloyed Structural Materials Used in Power Industry,* Proc. of Workshop 2008, Part A., CTU Prague, 2008, pp. 228–229.
[7] DALIKOVA, K., KUNZ, J., SIEGL, J.: *Fractographic Analysis of Fatigue Fractures of High Alloyed Austenitic and Duplex Steels (in Czech)*, Proc. of Letna skola unavy materialov 2008, IX. rocnik (Oscadnica), Zilinska univerzita, 2008, pp. 147–150.
[8] *High Performance Stainless Steels.* www.stainless-steel-world.net/pdf/11021.pdf, 94 p.
[9] *Calculation of pitting resistance equivalent numbers (PREN).* http://www.bssa.org.uk/topics.php?article=111.

Du Jian-hua – Zhao Yang-dong *

A NOVEL DAMAGE STATE SIMULATION METHOD WITH SHAPE MEMORY POLYMER

Shape Memory Polymer (SMP), a kind of smart materials which can memorize its former shape, has the general character of plastics and rubbers. The paper analyzes the present methods of damage simulation in numerical simulation and model test and performs mechanical test to study SMP's shape memory mechanism as LgE-T. A new thinking is put forward to make the stiffness-controlled specimen according to the deficiency of present simulation methods, which could not simulate the damage process. The validating test proves the stiffness-controlled specimen can simulate the damage process of accumulation and has the value of validating the damage identification and structural safety evaluation algorithms.

Key words: Shape Memory Polymer; damage simulation; stiffness-controlled specimen; safety evaluation

Due to a variety of unforeseen conditions and circumstances, it will never be possible or practical to design and build a structure that has a zero percent probability of failure. Structural aging, environmental impact, and reuse are examples of circumstances that could affect the reliability and the life of a structure [1]. There are needs of periodic inspections to qualify the safety of civil structures in service and take some measures to monitor and evaluate their performance, such as serviceability, reliability, and durability, for the purpose of determining the location, estimating the severity and evaluating the consequences of damage on the structure, if damage has occurred. Since the Aloha Boeing 737 accident [2] that happened on April 28, 1988, such interest has fostered researches in the areas of non-destructive damage identification and structural safety evaluation.

So far, many algorithms have been put forward, such as neural network method, modal flexibility change method, strain energy method and most of these methods have been successfully used to detect the location of certain damage elements, cracks or weld defects, corrosion or erosion [3]. But these algorithms should experience the test of availability verification before they are put into practical application, in which damage state simulation is a key factor. A new thinking of damage state simulation based on Shape Memory Polymer (SMP) is put forward on the analysis of the deficiency of present damage simulation methods, which could not simulate the damage process of occurence and accumulation. The checking result shows this method can regulate the damage degree through temperature adjustment and has the value of practicality.

1. Structural Damage State Simulation

1.1 Description and Consideration of Stiffness as the Damage Factor

To a multi-freedom degree system, its dynamic equation is defined as follows:

$$M\ddot{X} + C\dot{X} + KX = f(t) \tag{1}$$

If damp is ignored, its dynamic eigenvalue is expressed as the following equation:

$$(K - W^2 \cdot M) \cdot \varphi = 0 \tag{2}$$

where M is the mass matrix; C is the damp matrix; K is the stiffness matrix; X is the displacement; $f(t)$ is the input impact; W is the vibration frequency; φ is the vibration modal.

In the process of damage identification, W and φ are tested to judge the severity of damage. Therefore K and M should reveal some change, if damage occurs on the service structure. However when damage forms, such as structural cracks and cross-section cutting occur in real structure, the structural mass distribution generally has minor change, but its stiffness alters greatly, especially to giant structures [4]. Therefore, we always diminish the stiffness of certain parts to simulate the damage state while validating the damage identification and structural safety evaluation algorithms [5].

* **Du Jian-hua[1], Zhao Yang-dong[2]**
[1] School of Transportation, Shijiazhuang Institute of Railway Technology, 18 Sishuichang Road, Shijiazhuang 050041, China, E-mail: sirtdjh@163.com,
[2] First Branch, CCCC First Highway Consultants Co., Ltd 63 Keji 2nd Road, Xi'an 710075, P. R. China, E-mail: hityangdong@163.com

1.2 General Methods of Damage State Simulation

At present, numerical simulation of finite element method and model test are two ways to testify and evaluate the algorithm's validity used in damage identification and structural safety evaluation. To numerical simulation, stiffness-discount is usually used to produce the structural damage state through assuming the decreasing degree of stiffness of certain elements [6]. And during the laboratory or real-structure experiment, some certain kinds of physical methods are adopted to induce the damage state; for example, some parts of a model structure are cut smaller or moved away.

As shown in Fig. 1 and Fig. 2, the cross-section of a bridge model was cut to a certain degree [7] and a vent was introduced in a cantilever bridge model [8], and different degrees of damage state could be created by adjusting the parameters as t_1, t_2 and h. Fig. 3 is the famous I-40 bridge I-40 Bridge over Rio Grande in the Albuquerque, New Mexico damage identification test [9]. NMSU, in 1993, introduced four levels of damage (black part) in the middle span of the north plate girder by making various cuts in the web and the flange of the girder. Six kinds of safety monitoring and assessment algorithms were testified in the real-structure experiment.

1.3 Estimation and Judgment of Simulation Efficiency

Present simulation methods of damage state mentioned above have great meanings in validating and improving the precision of structural safety evaluation algorithms, but they might not be so effective when applied in a real structure and the potential reasons may be as follows besides an economical aspect:

- The simulated damage state appears as a mutation result and the safety evaluation methods can only be testified under pre-damage state and step-damage state, therefore it's unable to validate the algorithms in the process of damage accumulation;
- Input loads, such as wind, wave and fluent, are stopped before the physical damage state is introduced in certain parts of the structure, this breaks the verification process and decreases the degree of reliability.

2. Shape Memory Polymer

SMP is a special kind of functional materials that could memory its former shape and has the characters of plastics and rubbers, and since the first Shape Memory Polymer, Norborene Polymer, was reported in 1984 by the CDF-Chimie Company in France, many polymers have been studied as SMP, such as polyurethane, cross-linked polystyrene [10].

2.1 Shape Memory Effect

SMP could remember its original shape when it is deformed. This means the strain of SMP can be fixed after deformation and then recover almost completely to its original shape under some conditions (i.e. heat, PH value adjustment, ionic concentration, etc), which is called Shape Memory Effect (SME). Thermally-stimulated SMP is a common kind of shape memory materials.

It is regarded that SME reckons on the specially physical components of SMP, for containing a fixing phase (hard domain) and reversible phase (soft domain).The fixing phase can be chemical and physical cross-links, imparting a level of rigidity, dimensional stability, and thermal resistance, while the reversible phase can be either crystalline or amorphous, and provide properties of elastomers-primarily recovery and energy absorption.

2.2 Experimental test of Shape Memory Effect

The SME of SMP materials can be explained by their elastic modulus (E)-service temperature (T) character, therefore property test is designed to obtain and classify the relation curve between E and T.

Firstly, a II mechanical specimen of 50-mm gauge length is processed with a kind of thermally- stimulated SMP material guided by GB1040-1992 and polished to reduce the influence of stress concentration. Then, the tension test of normal temperature is carried out with testing machine as assistor and electronic extensometer memorizing the transmutation of specimen's gauge at 18.1° and 20.3°. Then the caloric test is practised from normal

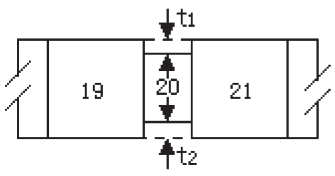

Fig. 1 Cross-section cutting method

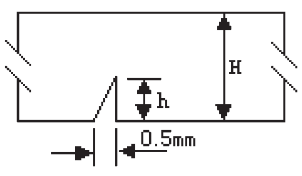

Fig. 2 Vent or crack method

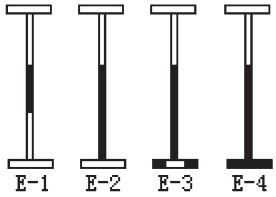

Fig. 3 Four levels of damage state induced in I-40 bridge test

temperature to about 80°. In this process, heat source is provided by thermal wind with infrared thermo scope registering temperature coordinates. It's noticed that SMP specimen becomes too soft to get précised data with the current instruments when the temperature reaches 60° or higher, and since the main intention is to measure the vitrification point high level of transmutation of used SMP, and ascertain at which temperature the SMP specimen could be considered to lose its stiffness. Therefore, the reference values manufacturing plant provide are used to describe the relation between E and T when the heated temperature is above 60°, and only five representative points of temperature coordinates are recorded in test.

2.3 Result Analysis

It can be seen from Fig. 4, the relation graph between LgE and T that the elastic ratio of SMP decreases more than two orders of magnitude when heated to the vitrification transition point where the stiffness of SMP could be considered lost. In consequence, we can make a kind of SMP structure and adjust the structure's stiffness to simulate the damage degree by controlling its service temperature and testify the validity of algorithms or programs used for damage identification and safety evaluation.

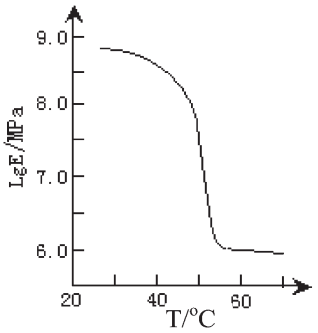

Fig. 4 Test graph of LgE and T

3. Facture of Stiffness-Controlled Specimen

3.1 Basic Theory Expression

For a structure in service, damage only appears in some parts, therefore a certain part of damage is required to reproduce, so SMP can be cut into pieces and glued to the fundal material, such as a polymethy methacrylate (PMMA) pipe. Fig. 5 is the integrated model of SMP and PMMA, whose stiffness is defined as follows:

$$EA = E_1A_1 + E_2A_2 \tag{3}$$

where E_1 and E_2 are the elastic modulus of SMP and PMMA; A_1 and A_2 are corresponding cross-section areas.

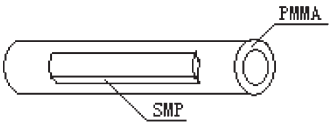

Fig. 5 Glued model of SMP and PMMA

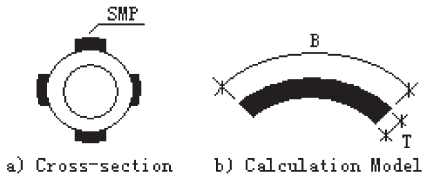

Fig. 6 Width calculation model of SMP

3.2 Length Calculation of SMP

Elastic modulus of PMMA, E_2, varies little when heated to a higher temperature known from its mechanical test result, so its stiffness could be assumed to remain the same at a heated state, and only the stiffness of SMP needs to be considered and regulated.

A kind of thermally-stimulated SMP is cut into four pieces, and B, the needed length with a fixed damage degree, could be calculated out from Fig. 6. According to physical and geometric knowledge, B is determined by the following equation:

$$\frac{4E_1BT}{E_2\dfrac{\pi(R^2 - r^2)}{4}} = K \tag{4}$$

Where R and r are the outer and inner diameters of PMMA; T is a fixed value defined by the thickness of SMP ply; K is a function of the damage degree, λ which sticks to the following equation:

$$K = \frac{\lambda}{1 - \lambda} \tag{5}$$

Suppose the thickness T of *SMP* ply is 8 mm, R and pipe wall of PMMA pipe are 34 mm and 3 mm, so the corresponding B is as Tab.1 shows.

Length calculation of SMP responding to damage degree Tab. 1

Volume	Corresponding value							
Damage degree λ/%	5	10	15	20	25	30	40	50
Length of SMP B/mm	1.4	3.0	4.7	6.7	8.9	11.4	17.7	26.6

3.3 Facture of glued specimen

Here we choose a thermally-stimulated kind of 3.46 mm-thick *SMP* ply and the fundamental material is a PMMA pipe with 25 mm outer diameter and 2 mm thickness pipe wall. Four pieces of SMP are cut into 200 mm-wide and 14 mm-long rectangles. The paste area is granulated to raise the paste force with sand paper and a kind of heat-proved glue water is used to integrate SMP and PMMA pipe together.

Fig. 7 is the picture of stiffness-controlled specimen, whose decreases to 30.9 % when heated to above 60°.

Fig. 7 Picture of glued joint specimen

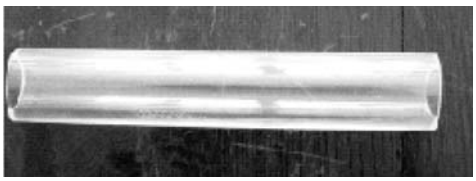

Fig. 8 Poured specimen of futher research

4. Feasibility Verification

The cured specimen has been stationed in the room temperature for about 24 hours before its stiffness is measured at a normal state and a heated state and five groups of data have been registered. Tab. 2 is the comparison between the academic analysis value and the test result.

The test damage degree of the SMP specimen is obtained as 29.7 % and it proves a higher precision compared with the academic analysis, but there still exist some relative errors. The possible reasons may be as follows:

- The influence of damp is ignored and it generally increases enhancing the stiffness of SMP specimen at a higher temperature state;
- The SMP material could not lose all the stiffness when heated to the above vitrification transition temperature and the altering of PMMA's stiffness value is not considered;
- The technical conditions, such as heat provision with a heat blower and glued joint need to be enhanced as well as the service precision of test instruments.

5. Conclusion

A considerable amount of experience was gained through developing a simulation method of damage state for verifying the validating the feasibility of damage identification and safety evaluation algorithms. The experience has led to the following recommendations:

1. As a kind of smart materials, SMP can memory its former shape which could be explained by its E–T character and the relation graph between LgE and T is established through tension test, which shows 60° is the vitrification transition temperature where to lose the whole stiffness;
2. A new thinking is put forward to feature the stiffness-controllable specimen with SMP affixed to fundus and the verifying test shows the specimen has a more precise ability of damage state simulation;
3. Further research mainly lies in reducing of the vitrification transition temperature of SMP, improving the technique of heatfeature and paste. The poured specimen, as Fig. 8 shows, is worth of particular research.

Comparison of experimental and analysis result Tab. 2

Test state	Theoretical result/GPa×mm^2			Test result/GPa×mm^2					
	EASMP	EAPMMA	EA	EA					Average
Normal	33.55	299.42	433.62	466.74	457.64	451.58	445.52	470.78	458.5
Heated	0	299.42	299.42	325.30	328.84	315.20	311.16	331.36	322.37

References

[1] CHEN, C. Z., LUO, Y. G., BAI, B. S.: *Structural Damage Inspection and Intelligent Diagnosis* [M], Bei Jing, Science Press, 2001

[2] OTT JET al. 737 *Fuselage Separation Spurs Review of Safeguards* [J], Journal of Aviation Week and Space Technology, 1988, 5, 92–95

[3] ROESSET, M. R, JAMES, T., YAO, P.: *Application of Structural Health Monitoring and Damage Detection to Marine Systems* [C], For Present at the Second World Conference on Structural Control (IWCSC) in Kyoto, Japan, 1998

[4] SHI, Z. Y, LUO, S. X, ZHANG, L. M. et al: *Detection of Location and Magnitude of Structural Damage Using Measured Model Data* [J], Journal of NUAA, 1997, 29(1), 71–78

[5] WANG, Z. G, PEI, Y. L., ZHAO, Y. D.: *Vibration-Based Damage Detection with Structural Modal Characteristics* [J], The Baltic Journal of Road and Bridge Engineering, 2008, (1), 21–28
[6] WANG, S. Q, ZHANG, S. G., LI, H. J.: *Study on the Structural Damage Identification Based on the Finite Element Model and Modal Parameters* [J], Journal of Ocean University of Qingdao, 2003, 33(4), 650–656
[7] ZHANG, Q. W., SHI, J. J., XIANG, H. F.: *Study on the Structural Damage Identification Methods of Bridges* [J], Shanghai Municipal Engineering, 1998, 2,1–8
[8] LI, G. Y., ZHENG, H. W.: *Study on the Modal Flexibility Analysis of Damage Structure* [J], Journal of Vibration, Measurement and Diagnosis, 2002, 22(2),136–152
[9] FARRAR, C. R., BAKER, W. E., BELL, T. M.: *Dynamic Characterization and Damage Detection in the I-40 Bridge over Rio Grande* [R], Rep, No: LA-12767-MS, Los Alamos National Laboratory, Los Alamos, NM87544
[10] LI, F. K., ZHU, W., ZHANG, X.: *Shape Memory Effect of Ethylene-VinyI Acetate Copolymers* [J], Journal of Applied Polymer Science, 1999, 71, 1063–1070.

Du Jian-hua – Ouyang Zhiwei – Zhao Yangdong *

DAMAGE IDENTIFICATION METHOD WITH STRUCTURAL FREQUENCY DATA FROM MODAL TEST

Testing and analysis technology based on vibration mode is a common method to structural health monitoring and checking. This paper deduces the damage factor used for structural damage evaluation based on test frequency of structure, makes a finite element numerical simulation using ANSYS software and model test to a pressure pipe. Here a stiffness reduction method is utilized to reproduce the damage state of a single-point and multiple-point, damage identification is carried out with a FEM model of redundant pipe. Meanwhile, a model experiment system is designed to validate the efficiency of damage factor with cutting-groove to simulate damage states. Numerical and experimental results show the proposed damage factor is theoretically breviate, simple realization and high-accuracy performance, therefore, it has a good usage prospect in the implementation of structural damage monitoring and identification.

Key words: Vibration mode; Structural damage evaluation, Damage factor, Damage state

1. Introduction

Technology of structural experiment modal analysis is an important measure for structural damage evaluation, which is based on a modal analysis, predicts and evaluates a variation of physical parameter according to the variation of a modal characteristic of pre-damage and post-damage of the structure [1]. The development and application of technology of structural experiment modal analysis is restricted because the modal data beyond all freedoms can not be measured in view of incompleteness of test data on spot. The measure of structural frequency is much easier and precise relative to the collected data of a vibration mode, and high frequency can be measured [2]. This paper deduces the evaluation method based on the variation ratio of squared frequency and the validity is checked from a numerical simulation and model experiment test validation. Numerical and experimental results show the proposed damage factor is theoretically breviate, simple realization and high-accuracy performance; therefore, it has a good usage prospect in the implementation of structural damage monitoring and identification.

The variation of structural physical parameters must result in the variation of structural modal parameters. Damage at a specialized position has different effect on each modal characteristic, and the difference is just the basis to detect the damage position. The relationship of damage and variation in a modal parameter can be found with the perturbation theory and structure equation of motion on the basis of structural damage of a certain degree [3, 4].

For a multiple-degree structural system, ignoring the effect of damp, vibration eigenvalue equation is

$$(K - \lambda \cdot M) \cdot \varphi = 0 \tag{1}$$

where M is the system mass matrix, K is the system stiffness matrix, λ is the eigenvalue and φ is the normalized vibration mode.

While the parameters of stiffness and mass of the structure have a little variation of ΔK and ΔM, from perturbation theory Eq. (1), we obtain

$$\left[(K + \Delta K) - (\lambda + \Delta\lambda) \cdot (M + \Delta M)\right] \cdot (\varphi + \Delta\varphi) = 0 \tag{2}$$

Generally, structural damage was induced by crack or corrosion and has little effect on mass distribution of an integral structure, that is to say $\Delta M \approx 0$. On expanding Eq. (2) and ignoring the effect of $\Delta M \cdot \Delta\varphi$ and $\Delta\lambda \cdot M \cdot \Delta\varphi$, we obtain

$$\Delta\lambda = \frac{\varphi^T \cdot \Delta K \cdot \varphi}{\varphi^T \cdot M \cdot \varphi} \tag{3}$$

For the i-th mode of vibration, Eq. (3) may be written as follows

$$\Delta\lambda_i = \frac{\varphi_i^T \cdot \Delta K \cdot \varphi_i}{\varphi_i^T \cdot M \cdot \varphi_i} \quad (i = 1, 2, \ldots n) \tag{4}$$

Using ΔK_n to donate the stiffness variation in the nth element, the Eq. (4) changes into

$$\Delta\lambda_i = \frac{\sum_n \varphi_i^T \cdot \Delta K_n \cdot \varphi_i}{\varphi_i^T \cdot M \cdot \varphi_i} \tag{5}$$

Eq. (5) is similar with Rayleigh Quotient in shape, which indicates the relationship between strain energy and structure eigenvalue [5]. Only when damage occurred on the nth element

* **Du Jian-hua[1], Ouyang Zhiwei[2], Zhao Yangdong[3]**
[1]School of Transportation, Shijiazhuang Institute of Railway Technology, Shijiazhuang, China, E-mail: sirtdjh@163.com
[2]School of Civil Engineering, Harbin Institute of Technology, Harbin, China, E-mail: 5903098@163.com
[3]First Branch, CCCC First Highway Consultants Co., Ltd, Xi'an, China

$$\Delta\lambda_i = \frac{\varphi_i^T \cdot \Delta K_n \cdot \varphi_i}{\varphi_i^T \cdot M \cdot \varphi_i} \tag{6}$$

The eigenvalue of variation, λ can be defined as the function of damage location n and damage degree ∂_n

$$\Delta\lambda_i = \lambda_i(\partial_n, n) \tag{7}$$

Then $\Delta K_n = \partial_n \cdot K_n$, and Eq. (6) can be reduced to the following expression

$$\Delta\lambda_i = \frac{\partial_n \varphi_i^T \cdot K_n \cdot \varphi_i}{\varphi_i^T \cdot M \cdot \varphi_i} \tag{8}$$

From Eq. (8) we know that the variation in eigenvalue is the function damage position and damage degree. Assuming the two-order variation eigenvalue $\Delta\lambda_i$ and $\Delta\lambda_j$ which correspond to two modes and the corresponding frequency variation ratio is

$$\frac{\Delta\lambda_i}{\Delta\lambda_j} = \frac{\dfrac{\varphi_i^T \cdot K_n \cdot \varphi_i}{\varphi_i^T \cdot M \cdot \varphi_i}}{\dfrac{\varphi_j^T \cdot K_n \cdot \varphi_j}{\varphi_j^T \cdot M \cdot \varphi_j}} \tag{9}$$

Eq. (9) shows that the variation ratio of squared frequency of any two modes is only the function of damage position, and damage of element in different position is corresponding to a set of variation ratio of squared frequency. The damage position can be identified and damage degree can be evaluated according to the variation ratio of squared frequency of each mode.

2. Numerical simulation

A pressure pipe with one end fixed and the other end simply supported is shown in Fig. 1 and Fig. 2 gives its corresponding FFM model.

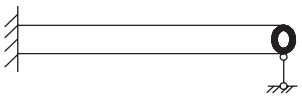

Fig. 1 Schematic of the structural model

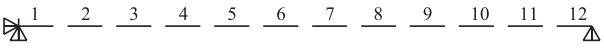

Fig. 2 Meshing of the structure

For the purpose of making a dynamic analysis to the structure using FEM software ANSYS, the finite element model of the structure consists of 12 elements and 13 nodes. The values for the geometric properties are assigned as follows: (1) the length of the pipe l = 2400 mm; (2) the outer diameter D = 70 mm; and (3) the thickness of the pipe t = 25 mm. Values for the material properties of the beam elements are assigned as follows: (1) the elastic modulus E = 72 GPa; (2) Poisson's ratio v = 0.3; and (3) the linear mass density ρ = 2800 kg/m^3. Using stiffness reduction to simulate the damage of the structure member, the nine kinds of cases of pre-damage and post-damage are: – undamaged– – damage at a single-point (the stiffness of element three, six, eight and eleven decreases by 10 % respectively); – damage degree increases in turn (the stiffness of element five decreases by 10 %, 15 % and 20 % respectively); – damage at a multiple-point (the stiffness of element three and eleven decreases by 10 % at the same time), the results are shown as Table 1.

Making a comparison of cases of pre-damage and post-damage, letting the variation ratio of squared frequency be $\eta = \Delta\lambda_j/\Delta\lambda_i$ (the variation ratio of first five mode and the first mode), using the vibration number n as the horizontal coordinates and η as the vertical coordinates, the results are shown in Fig. 3.

From the figures we know that damage in different positions has different effect on the variation ratio of squared frequency of the structure and relates with the connection conditions of the structure with other structure. With the damage position away from the fixed end, the value of the variation ratio of squared frequency η decreases gradually and then increases again at the simply supported end. Damage at a multiple-point contains the information of damage at a single-point and the variation rule is similar with the above conditions. When the damage degree increases, η also gradually decreases. It shows that the different damage degree has a multiple relation with the damage index ∂_n. Damage can be located and damage degree can be evaluated preliminarily using

The frequency (Hz) of FEM modal analysis — Table 1

Mode	Damage cases								
	Undamaged	Damage at single-point Element/degree				Damage degree increases gradually Element/degree			Damage at multiple-point Element/degree
		3/10%	6/10%	8/10%	11/10%	5/10%	5/15%	5/20%	3, 11/10%
1	39.306	39.272	39.113	38.993	39.228	39.223	39.176	39.123	39.194
2	127.27	127.00	126.84	126.99	126.58	126.35	125.83	125.26	126.31
3	265.22	263.45	264.08	264.22	263.14	265.07	264.98	264.88	261.39
4	452.94	450.19	450.37	449.58	449.33	449.96	448.30	446.49	446.59
5	528.60	524.26	525.85	527.09	528.41	525.24	523.30	521.13	524.08

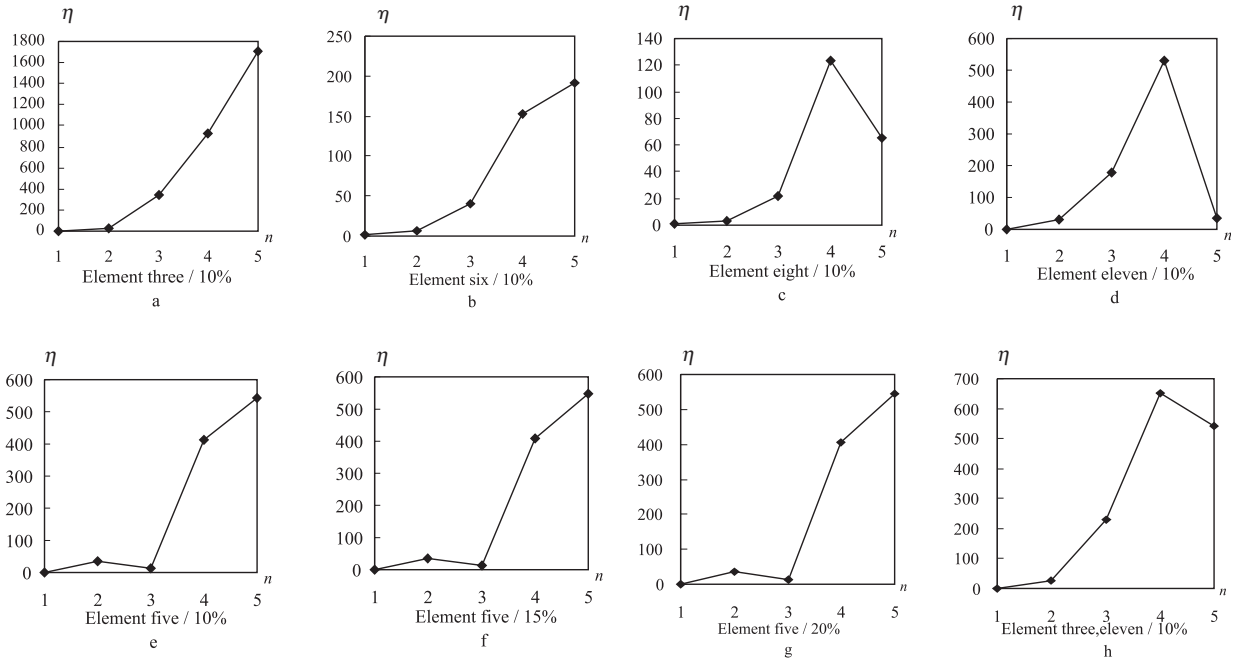

Fig. 3 Variation ratio of squared frequency

the variation ratio of squared frequency because the information of the whole structure can be expressed by the information of the elements [6].

3. Model test

3.1. Test system

The test system and model are shown in Fig. 4.

The modal test is made using a pressure pipe model. The beam is divided into twelve elements from the fixed end evenly.

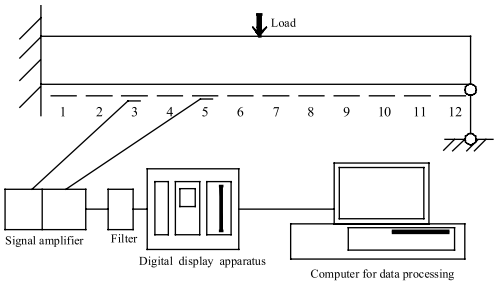

Fig. 4 Schematic of test system

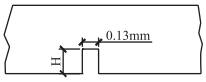

Fig. 5 Damage state

A foil electric resistance strain gage of 120±0.5 Ω is pasted at the middle location of each element along the axis on the beam.

The structure makes free vibration at the pulsed excitation. After the strain response the signal is picked by a strain sensor, the strain response signal is amplified via YD-15 dynamic stain gauge, by entered dynamic signal digital display apparatus NICOLERT-2090, amplified again and filtered, at last turned into a digital signal, input into the computer and processed with ITDM (Ibriham Time Domain Method) program. The modal parameters such as natural frequency, strain modal characteristic and damp ratio can be identified.

2.2. Damage simulation

First, at the undamaged state of the beam structure, the vibration modal characteristic of the structure can be obtained using a single point impulse. The modal characteristic analysis is made after an impulse and response signal entered the dynamic stain gauge. The first five modal characteristics are obtained through the test, and the coherent function is quite good. The damage state on a beam section is simulated by cutting a groove which has a width of 0.13mm, varies with depth and is eroded by a thread with a diameter of 0.1mm, and the vibration test is performed.

Three cases of vibration test are performed: – undamaged; – damage at a single-point (damage occurs at element three, eleven; damage occurs at element five using the increasing thickness of 2 mm, 4 mm and 6 mm in turn to simulate the damage state of the structure); – damage occurs at a multiple-point (damage occurs at

element three and element eleven using the thickness of 2 mm to simulate the damage).

3.3. Data processing and result analysis

Table 2 is the experiment test data. After making an analysis of the test results, the relationship drawing can be worked out as shown in Fig. 6 a~f .

From the results of data processing we know that the structural frequency which is related with the characteristic of the structure such as restraint conditions except for the damage position and damage degree shows a definite variety rule under damage at a single-point and multiple-point.

4. Conclusion

(1) There has been the function relationship between the variation ratio of squared frequency of pre-damage and cases of damage at multiple-point and between the variation ration of squared frequency of pre-damage and different damage degree.

(2) The analysis results show that the damage evaluation can be performed if only the former two rank variation ratio of squared frequency is acquired, but the method can not make damage state identification for symmetrical elements of the structure. The shortage can be made up with the vector data, while the damage of actual structure will not be symmetrical absolutely.

(3) The damage of a great number of structures can be denoted by using scalar quantity $\Delta K_n = \partial_n \cdot K_n$ to express the reduction of

The frequency (Hz) of model test — Table 2

Mode	Damage cases						
	Undamaged	Damage at single-point Element/H		Damage degree increases gradually Element/H			Damage at multiple-point Element/H
		3/2mm	11/2mm	5/2mm	5/4mm	5/6mm	3, 11/2mm
1	40.81	40.75	40.74	40.73	40.68	40.64	40.71
2	132.12	131.83	131.43	131.17	130.66	129.87	131.08
3	275.28	273.49	273.16	275.12	275.01	274.87	271.23
4	470.18	467.22	466.46	467.11	465.31	463.86	463.46
5	548.8	544.16	548.53	545.17	543.13	540.68	544.04

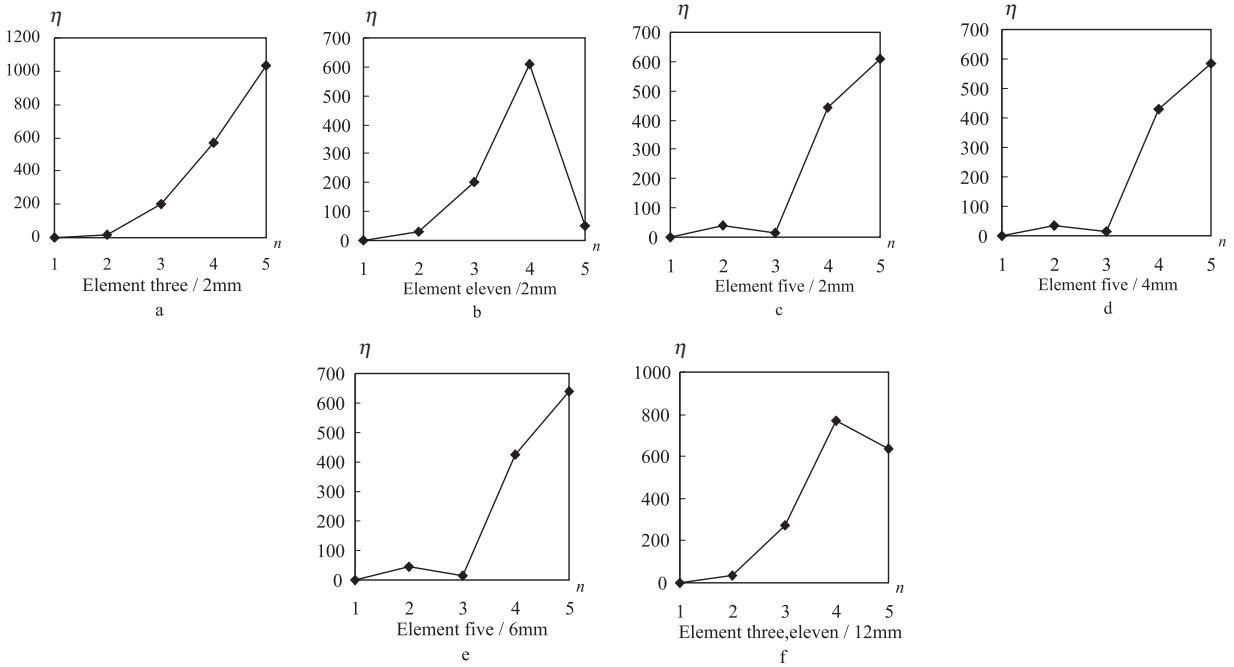

Fig. 6 Variation ratio of squared frequency of damage at single-point and multiple-point of the test

the element stiffness in the field of civil engineering, so does this paper in which damage state of the structure is simulated by the method of stiffness reduction. When applied in actual engineering, due to a high level of noise in a modal test, the measured frequency and vibration modes actually show much difference from the actual condition, and the effect of identification is affected [7]. The damage identification algorithm and checking measure which can eliminate the effect of noise should be studied further.

Acknowledgement

Here we wish to acknowledge the National High Technology Research and Development Program of China under granted number 2001AA602023-1 and my workmates with latent capacity in the Institute of Traffic Engineering, HIT, for their fund sustentation, warm support, precise comments and detailed helps, which lead to the belief that their dedication is certainly a contributing factor to this research work and it would not have been feasible without their support.

References

[1] MA, H. W., YANG, G. T.: *Methods and Advances of Structural Damage Detection,* Advances in mechanics, 29 (4): 513-527, 1999
[2] LI, G. Q., LOU, G. B.: *The Identification of Stiffness Parameter of Frame Structure Using Frequency of Local Vibration*, Journal of Vibration, measurement & Diagnosis, 21(3): 196–201, 2001.
[3] HEARNG, TESTARB: *Modal Analysis for Damage Detection in Structures*, Journal of Structural Engineering, 117(11): 3042-3063, 1991.
[4] WANG, Y. G., PEI, Y. L., ZHAO, Y. D.: *Vibration-Based Damage Detection with Structural Modal Characteristics*, The Baltic Journal of Road and Bridge Engineering, 3 (1): 21–28, 2008.
[5] SONG, Y., XIANG, Y. Q., XU, X.: *Damage Identification of Bridges Based on Vibration of Structure*, Journal of Vibration, measurement & Diagnosis, 25(3): 222–226, 2005.
[6] BYUNG, O., HWAN, H., JUNG, B. S.: *Structural Assessment with Combined Data of Static and Modal Tests*, Journal of Structural Engineering, 124 (8): 956–965, 1998.
[7] CAWLEY, P., ADAMS, R. D.: *The Location of Defects in Structures from Measurements of the Natural Frequencies*, Journal of Strain Analysis, 14(2), 49–57, 1979.

Andrzej Popenda *

THE DFM CONTROL SYSTEM BASED ON PLL

A specific structure of control system with double fed machine (DFM) is studied in the paper. The DFM is assumed to be a generator with stator winding connected to the power grid and it produces active and reactive powers. A command vector controlling DFM is transformed to the rotor-oriented coordinate system using angle of transformation. The angle of transformation is estimated in the system by applying a phase locked loop (PLL).

Moreover, an example of application of pulse phase locked loop for estimation of voltage vector components is presented in the paper. In conclusion the properties of proposed PLL-based control systems are compared with properties of systems known from radio engineering and telecommunications described in the first chapter of the paper.

1. Introduction

The doubly fed induction machine (DFM) is suitable for generating systems working with variable rotor velocity. Shaft generators on ship and wind power systems are examples of application of DFM.

A specific structure of control system with DFM is studied in this paper. The DFM is assumed to be a generator with stator winding connected to the power grid and it produces active and reactive powers. The current regulated voltage source inverter (CRVSI) supplies the rotor winding. A command vector controlling DFM is transformed to rotor-oriented coordinate system using angle of transformation. The angle of transformation is estimated in the system with application of a phase locked loop (PLL). An application of PLL in considered control system allows omitting rotor position sensor (encoder). Examples of application of PLL to estimate the angle of transformation are given in papers [1, 2].

The phase feedback known from radio engineering and telecommunications as phase locked loop (PLL) is conventional solution applied for synchronization of single-phase periodical signals [3, 4]. PLL equalizes frequency of voltage-controlled oscillator (VCO) with standard frequency. It is useful e. g. in demodulation of frequency-modulated signal (FM) as well as in frequency multiplication.

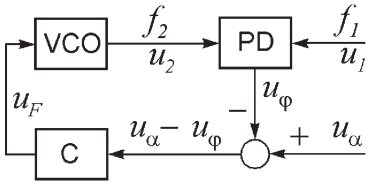

Fig. 1 The block diagram of circuit with PLL [3], where VCO is voltage-controlled oscillator, PD is phase detector, C is controller, u_φ is PD output voltage (controlled voltage), u_α is reference voltage, $u_\alpha - u_\varphi$ is control error, u_F is command voltage (control voltage), f_1 is standard frequency

The block diagram of the circuit with PLL is depicted in Fig. 1. The control voltage u_F changes VCO output frequency in the neighbourhood of rest frequency f_0. Phase detector gives output voltage dependent on phase shift φ between VCO output voltage (u_2) and standard voltage (u_1). The specific feature of the circuit shown in Fig. 1 is astatic character of controlled system (VCO together with PD). Thus, the phase shift φ increases proportionally to time without limit if frequency f_2 differs from the standard frequency f_1. Therefore, a difference in frequency should approach zero.

The block diagram of PLL with application of multiplier as a phase detector is depicted in Fig. 2. The output voltage of the multiplier contains a high-frequency component and a low-frequency component. Abovementioned high-frequency is equal to the sum of basic frequencies f_1 and f_2, whereas low-frequency is equal to difference of both basic frequencies.

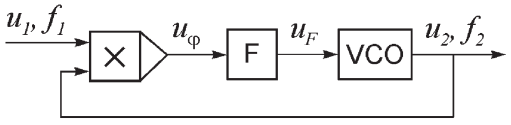

Fig. 2 The block diagram of PLL with multiplier as phase detector [4]

* **Andrzej Popenda**
Institute of Industrial Electrical Engineering, Faculty of Electrical Engineering, Technical University of Czestochowa, Poland, E-mail: popenda@el.pcz.czest.pl

A low-pass filter (F) is applied in order to eliminate the high-frequency component from PD output voltage. The output voltage of low-pass filter which controls VCO is expressed as follows:

$$u_F = \frac{AV}{2}\cos\left[\int_0^t(\omega_1 - \omega_2)d\tau - \varphi\right]. \quad (1)$$

In steady state ($\omega_1 = \omega_2$) a value of voltage u_F is constant:

$$u_F = \frac{AV}{2}\cos\varphi\,. \quad (2)$$

Operating range of PLL, i. e. allowable deviation of standard frequency from rest frequency ($\Delta f = f_1 - f_0$) for which the circuit shown in Fig. 2 still reaches synchronism, is limited by maximal and minimal value of voltage u_F. As it results from dependence (2), in the circuit shown in Fig. 2 mentioned values are determined for arguments φ equal to 0 and π while the rest value of angle φ amounts to $\pi/2$.

The phase shift between two voltages may also be detected through sample-and-hold circuit sampling actual value of voltage u_1 in the moments when voltage u_2 crosses the zero level in direction of positive values. The block diagram of PLL with S&H circuit as phase detector as well as transient responses of the PLL explaining principle of operation are shown in Fig. 3 and 4.

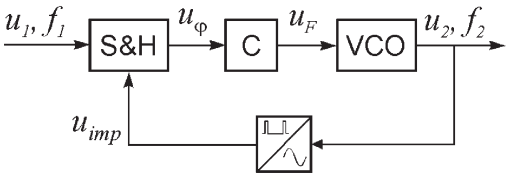

Fig. 3 The block diagram of PLL with S&H circuit as phase detector [3]

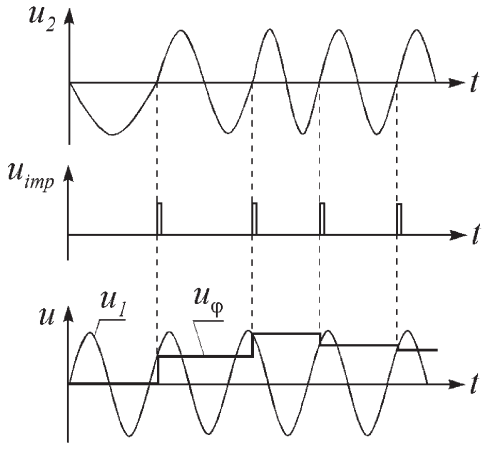

Fig. 4 Transient responses of the system shown in Fig. 3

Operating range of PLL depends on amplification in main circuit of considered structure working with unlocked loop (amplification of input-actuated control system). There is no possibility of unlimited increase in value of amplification due to decrease of stability margin of the PLL. Therefore, operating range of PLL shown in Fig. 3 is not large (a few percent in comparison to the rest frequency f_0).

2. PLL-Based Synchronization of Inverter Current in DFM Control System

An application of nonlinear element (multiplier) as a phase detector causes distortion of the output signal (u_φ). The low-pass filter is applied in order to decrease the distortion. The application of the low-pass filter causes a slower operation of PLL. A control of spatial vector position angle is used in poly-phase systems instead of synchronization of single-phase signals. A filtration of the angle calculated with application of vectors' calculus is unnecessary. Controlled variable (u_φ) obtained as vectors' calculus product is proportional to the angle φ. Thus, maximal and minimal values of the control variable (u_F) are determined by arguments $\varphi = \pm\pi$, whereas the rest value of u_F appears when $\varphi = 0$ provided that the reference variable (u_α) is equal to zero. The control systems with electric machines based on vector methods are examples of poly-phase (three-phase) systems.

From the above analysis it follows that operating range of PLL in the poly-phase systems is wider than in the single-phase system shown in Fig. 2. Moreover, the phase shift φ between u_1 and u_2 is equal to zero in a steady state when the PI controller is applied. A block diagram of DFM control system with PLL is depicted in Fig. 5. An application of PLL allows adjusting the frequency of the inverter current depending on power grid frequency and rotational speed of DFM rotor.

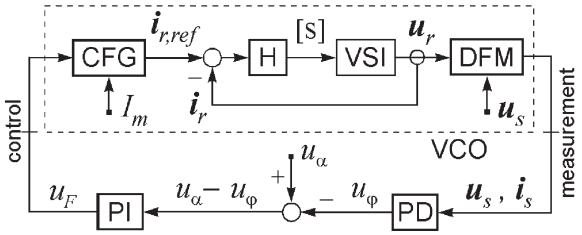

Fig. 5 The block diagram of DFM control system with application of PLL, where CFG is generator of current frequency, H are current controllers, VSI is voltage source inverter, PI is angle controller, u_s is stator voltage vector, i_s is stator current vector, u_r is rotor voltage vector, i_r is rotor current vector, [S] is vector of command signals controlling the inverter switching

The DFM working with stator winding connected to the power grid and rotor winding fed via a current regulated voltage source inverter (CRVSI – locked circuits containing VSI together with controllers H) is considered as a controlled system (plant). The current controllers (H) allow keeping phase currents of the

rotor in a required range. A generator of current frequency (CFG) provides the current controllers with set values of controlled currents. Nonlinear CFG transforms set amplitude and set frequency to actual set currents in the three-phase system. The angle controller (PI) produces the set frequency of rotor current, while the phase detector (PD) produces a signal proportional to the angle φ between the rotor current vector in stator terms and the stator voltage vector. A phase shift φ as well as the ratio of active power p and reactive power q generated to the grid depend on the actual value of reference voltage u_α.

A simple dependence may be used for approximation of the angle φ [1, 2]:

$$\varphi = \operatorname{arctg}\frac{q - q_0}{p} + n\pi,\ n = -1, 0, 1,\ -\pi \le \varphi \le +\pi \quad (3)$$

where $p = u_{s\alpha}i_{s\alpha} + u_{s\beta}i_{s\beta}$, $q = u_{s\beta}i_{s\alpha} + u_{s\alpha}i_{s\beta}$ are active power and reactive power of the stator, $q_0 \approx u_s^2/\omega_s L_s$ is reactive power connected with magnetizing current of the induction machine. The application of the above dependence allows skipping a transformation of rotor current to the coordinate system connected to the stator voltage vector. Thus, a rotor position sensor (encoder) is omitted in the structure of the considered DFM control system. This is the most valuable advantage resulting from the application of PLL in the DFM control systems.

In the system shown in Fig. 6, PLL replaces the encoder and estimates the rotor position angle. The DFM power p, q controllers produces set components $i_{rp,ref}$, $i_{rq,ref}$ of the rotor current vector. The components are transformed to the rotor-oriented coordinate system 0xy and control the CRVSI. Moreover, the components $i_{rp,ref}$, $i_{rq,ref}$ allow calculating the reference angle α. The controller of the angle φ estimates difference ω in angular velocity between the rotor and stator voltage vector. The angle γ

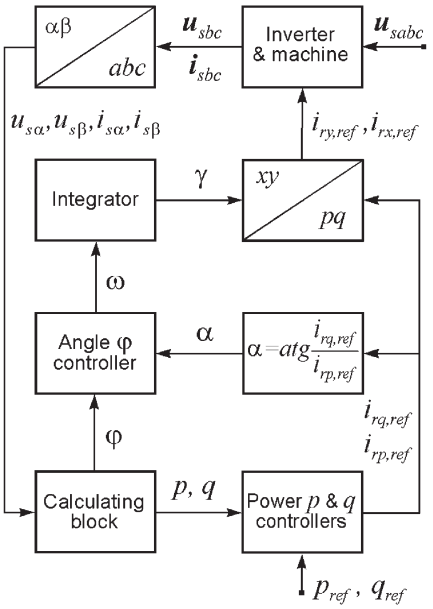

Fig. 6 The DFM power control system with PLL [2], where atg(.) is arc-tangent function

of rotor position in the coordinate system 0pq connected to the stator voltage vector is obtained as a result of integration of variable ω and allows transforming the set current components from 0pq to 0xy coordinate system.

Transient responses of the control system shown in Fig. 6 are given in Fig. 7. As it follows from the diagrams the considered system with PLL (Fig. 6) controls the active power p and reactive power q in short time without coupling between p and q, similarly to the DFM control systems with an encoder [1, 5].

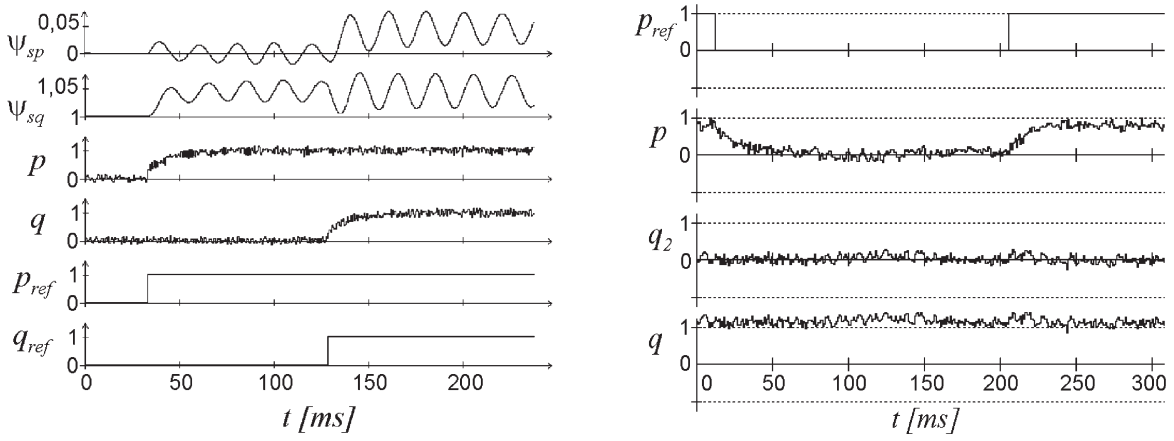

Fig. 7 Transient responses of control system shown in Fig. 6 obtained from digital simulations (left diagram) and experimental investigations (right diagram), where p, q are active and reactive power generated to the power system from DFM stator winding, p_{ref}, q_{ref} are reference values of active and reactive power, q_2 is reactive power of rotor, ψ_{sp}, ψ_{sq} are components of stator flux vector in coordinate system connected to the stator voltage vector; the variables are given in non-dimensional units

In designing the supply systems for electrical machines and electrical equipment it should not be omitted that the machines and equipment exert an influence on power grid and local electric power systems. The mains voltage drops and oscillations as well as the harmonics generated by electric machines and other disadvantageous phenomena from power quality point of view occur as a result of this influence [6 – 9]. The author of [10] pays attention to mentioned phenomena and he proposes a number of predicting analyses concerning power demand for individual consumers or groups of consumers. He also proposes predicting analyses concerning areas connected with work of selected sets of local consumers in power systems.

3. An Estimation of Spatial Vector Position Using Pulse PLL

The author used the pulse phase locked loop depicted in Fig. 8 to estimate the phase of stator voltage (power voltage) during experimental investigations. Estimated phase of stator voltage allows obtaining the components of stator voltage vector in an immovable coordinate system when the voltage amplitude is known.

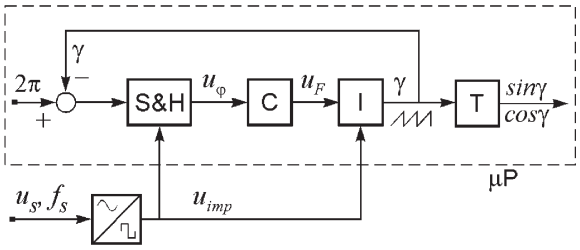

Fig. 8 The system with pulse PLL estimating phase of stator voltage, where S&H is sample-and-hold circuit, I is integrator, T are look-up tables of sine and cosine as a function of angle γ, μP is microprocessor system

The advantages resulting from the application of pulse PLL are as follows. Only one binary input is required to load the pulses of voltage u_{imp} into a microprocessor system instead of two analogue inputs. Moreover, time-dependences of the estimated stator voltage vector components are undistorted in steady state.

A principle of system operation is described below. Quasi-sinusoidal single-phase voltage u_s of power grid (standard voltage) is converted into square-wave voltage u_{imp} having the same frequency through the analogue comparator. Leading edges of square-wave voltage generate synchronizing pulses which initiate S&H circuit. The phase 2π is compared with the actual value of the signal γ generated by integrator. A quickness of γ increase depends on an abruptly changing variable u_F as the signal γ comes from u_F integration. Moreover, the synchronizing pulses reset integrator and thereupon signal γ begins increasing again. The values of sine and cosine functions are read from look-up tables in microprocessor system for actual value γ. The values are used in order to approximate the voltage vector components $u_{s\alpha} = u_{sm} \cos \gamma$ and $u_{s\beta} = u_{sm} \sin \gamma$, whereas amplitude u_{sm} is known.

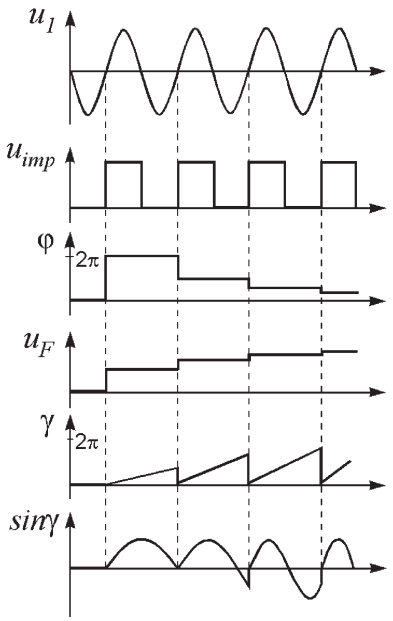

Fig. 9 Time-dependences in the system shown in Fig. 8

A discrete controller C provides integrator I with abruptly changing variable u_F in determined intervals $\Delta t = t_j - t_{j-1}$ when synchronizing pulses occur in the system. Output signal of controller is changed in accordance to the following formula:

$$u_{F(j)} = u_{F(j-1)} + k u_{\varphi(j)}, \tag{4}$$

where $u_{F(j)}$, $u_{F(j-1)}$ are values corresponding with actual and previous synchronizing pulse, respectively, k is controller amplification.

The time-dependences explaining a principle of system operation are shown in Fig. 9. The variable γ is constant if signal u_F is equal to zero, i. e. the rest frequency of oscillator is also equal to zero. Even significant deviation of standard frequency from rest frequency is followed by synchronization of presented system. Thus, operating range of considered PLL is limited only by microprocessor parameters.

4. Conclusion

Two examples of application of phase locked loop in control system with double fed machine are presented in the paper. First example concerns synchronization of inverter current generated to the rotor winding depending on power grid frequency and rotor velocity. The second example concerns estimation of power grid voltage vector components. Comparing properties of proposed

systems containing PLL and properties of systems known from radio engineering characterized in the first chapter of the paper, it may be concluded that:

1. In the PLL circuit using multiplier as phase detector the controlled variable is distorted. The low-pass filter is applied in order to minimize the distortion. It is a reason of slower operation of considered circuit. In the poly-phase systems, e. g. DFM control systems, the control of spatial vector position angle replaces synchronization of single-phase signals. A controlled variable proportional to angle is undistorted. Thus, filtration is unnecessary.
2. An application of PLL for synchronization of inverter current with power grid frequency and rotor velocity allows omitting the rotor position sensor in DFM control system. Properties of proposed by author DFM control system with PLL are similar to the system with encoder.
3. The pulse PLL used for estimation of power grid voltage components allows reducing a number of analogue inputs and simplifies meter circuits. Moreover, it possesses filtering properties and it does not cause a phase shift between standard (grid) voltage and estimated voltage.
4. Operating range of structures proposed by author is wider than those known from radio engineering and telecommunications.

References

[1] POPENDA, A.: *Decoupling control of doubly fed induction machine without rotor position measurement,* Proc. of Conf. PCIM'95, Nuremberg, 1995, pp. 561–571.

[2] POPENDA, A.: *Control of double fed asynchronous machine using digital signal processor,* Proc. of Conf. EDPE'99, High Tatras, 1999.

[3] TIETZE, U., SCHENK, CH.: *Semiconductor Control Systems (in Polish),* Warszawa WNT, 1997.

[4] KUDREWICZ, J.: *Phasing loops dynamics (in Polish)*, Warszawa WNT, 1991.

[5] BOGALECKA, E.: *Control problems with double-fed machine operating as a generator in electric power system (in Polish)*, Prace Naukowe Wyzszej Szkoly Morskiej w Gdyni, Gdynia, 1997.

[6] RUSEK, A., POPENDA, A.: *Transient states of polymerizer drive including real load of specially designed induction motor*, Proc. of Conf. on Electrical Machines (ICEM), Crete Island, 2006.

[7] RUSEK, A.: *The mathematical model and selected transient states of polymerization reactor drive supplied with frequency converter,* IVth Int. Sc. Symp. Elektroenergetika 2007, 19.-21. 9. 2007, Stara Lesna, in press.

[8] POPENDA, A., RUSEK, A.: *The impact of magnetic circuit saturation on properties of specially designed induction motor for polymerization reactor,* ISEF 2007 – XIII Symposium on Electromagnetic Fields in Mechatronics, Electrical and Electronic Engineering, Prague, 2007, in press.

[9] POPENDA. A., RUSEK. A.: *Mathematical model and selected transients states of main drive for polimerization reactor taking into consideration operating parameters of mixer chamber (in Polish)*, VI Sc. Symp. PTETiS "Wybrane Zagadnienie Elektrotechniki i Elektroniki (Selected Problems of Electrical and Electronic Engineering) WZEE'2006", Lublin – Kazimierz Dolny, 2006, pp. 220–229.

[10] POPLAWSKI, T.: *Application of the Takagi-Sugeno (TS) fuzzy logic model for load curves prediction in the local power system*, IIIrd Scientific Symposium Elektroenergetika 2005, Stara Lesna, 2005.

Lena Weick *

THE CHALLENGES OF MARKET RESEARCH IN CHINA

This article analyses the challenges of current market research activities in China. A country that achieved remarkable economic development since the late 1970s and that is still continuing to grow.

*Firstly a picture of the **market research industry** in China is provided. Based on the history of market research, the leading companies and the most important types and aims of research are highlighted. The development of the market research industry in the framework of the Chinese market in general leads to challenges in primary and secondary research. **Primary research** in China is dominated by regional disparities, particularly in terms of language and culture. A continuous trend to urbanisation leads to a massive accumulation of individuals and enterprises in 'mega cities'. Even so, the challenge of providing solid data quality seems to be still considerable. On the other hand, **secondary data** is still lacking in many ways. The availability is still sporadic and the quality remains inadequate. Furthermore the validity in general appears to be questionable.*

As discretionary income increases, the type and amount of products being consumed has changed significantly. Chinese customers are therefore confronted with a growing range of buying decisions. The rate of which the Chinese market is changing underlines the importance of research being up-to-date.

1. Introduction

In recent years China has become an important market for foreign investment. Overseas companies feel strongly attracted to China due to its strong economic growth and the size of its market. Since entering the World Trade Organisation, trades barriers have been reduced and new sectors of the economy have opened up to foreign firms [8, 15, 22]. As the result of rapid market growth and development, Chinese per capita gross domestic product (GDP) has quadrupled over the past two decades, growing at an annual average rate of 10%. Apart from differences in purchasing power, China has emerged as the second largest economy in the world [19].

Notwithstanding the tremendous progress on economic reforms and modernisation, it is essential to understand that the Chinese market has many specifics making it challenging for foreign companies doing business there [22]. Moreover, reliable and comprehensive market information is important for accurate market evaluation and the development of successful marketing strategies. In order to occupy a leading position in a keen market, companies must understand Chinese market structures and specifics. They need information that can help them develop a clear picture of the market and avoid costly mistakes that might lead to inadequate strategies or lost opportunities [1]. Different challenges and obstacles must be overcome when gathering information in emerging markets like China. As Walters and Samiee (2003) and Trinh (2004) state, the lack of information is a key reason for the absence of planning activities in many developing markets [22]. In this regard, China is no exception. In addition, the limited market transparency, the diversity of the country and the cultural and linguistic barriers complicate opportunities for collecting information and carrying out effective market research [21, 23].

2. The Chinese Market Research Industry

With a history of about 25 years, the market research industry in China is relatively young. In 1979 with the start of the open policy in China, the requirements for a free market economy and market research were born. Research firms based in Hong Kong started their exploration of the Chinese market and carried out first market research projects. A few years later, the first state-owned consulting companies in mainland China emerged. Particularly since the Chinese economy has become more market orientated with increasingly discerning customers, the demand for market research services has increased and with it the number of market research companies has grown significantly [23].

The total number of *market research agencies in China* is uncertain. The Chinese Market Research Association (CMRA) quoted that over 1200 such companies are active in the country. This number includes medium and large-sized companies as well as smaller market research providers. The CMRA [27] classifies the market into seven tiers, according to the companies' turnover in China. AC Nielson, CTR (a joint venture between TNS and a state-owned research company CVSC) and CSM (a CTR subsidiary) achieved the highest turnover with close to $26.8 million

* **Lena Weick**
Faculty of Economics, University of Applied Sciences Darmstadt, Germany, PhD-Student, Faculty of Operation and Economics of Transport and Communications, University of Zilina, Slovakia, Email: lenaweick@web.de

in 2006. Tier two and three includes many of the most famous companies in research like Research International, Synovate, Ipsos China and Sinotrust (a Chinese company) as well as GfK China, Gallup China, TNS, and Millward Brown. Most of the large agencies have an office in each of the three major cities: Beijing, Shanghai and Guangzhou.

Over the past years, some of those large general research companies have increased their business-to-business focus, and also foreign B2B research specialists have arrived in China. In terms of B2B research capabilities, two Chinese agencies are noteworthy: Sinomonitor and All China Market Research (ACMR). The latter is a subsidiary of the State Statistical Bureau of China and benefits from its access to legislators and regulators.

A high number of smaller Chinese research companies with a turnover less than 5 million RMB are largely provincial rather than based in Beijing, Shanghai and Guangzhou. Their research activities mainly focus on fieldwork to collect information outside the big cities, on behalf of larger agencies. Around half of the foreign research agencies are subsidiaries or joint ventures and provide full services including fieldwork and desk research. Most of their research is commissioned by western clients, together with a small number of Chinese clients. The latter are especially interested in conducting export studies in western countries, a trend that is expected to increase over time [9].

In 2006 the *value of market research* commissioned in China was worth about $US 636.1 million. The market was growing at 20 % per annum. With about 25–30 % of the overall industry value the proportion of *business-to-business research* was relatively high. By contrast, the proportion of B2B research in the Western market amounts to 10 % of the overall industry value. Large-scale business-to-business research is developing rapidly in China as foreign companies invest further in a better understanding of how they may enter new and expand current market audiences. *Business-to-consumer research* is already well developed in China with a wide range of international and domestic providers. While the Chinese market for consumer research was estimated to be growing at 17–18 % per annum, the business-to-business research with a value of $US50 million was even estimated higher, growing 25% per annum [9, 16].

The *focus of market research* in China differs from that in Europe and North America. In western countries research reflects the objectives of companies operating in mature markets wanting to e.g. monitor the satisfaction of their costumers; segment their target groups and establish customer loyalty. Therefore typical research projects are customer satisfaction studies, branding and segmentation studies. The clients generally seek information that will help them to progress in existing markets. Conversely, in China about 60% of research projects are focussed on market entry and market assessment studies, in which clients ask for information about market size and structure [9].

In terms of *industry sectors* in which organisations conduct most research, the level of commissioned research in 2006 can be ranked as follows: automotive, followed by petrochemical, information technology (IT), telecoms, pharmaceutical/ medical and finally financial [9].

The *development of a marketing research infrastructure* is comparably fast as is the Chinese market environment in general. The history of China's market research industry reveals that the sector is relatively young and has a fluctuating growth rate. Access and quality of information are still not the same as in western countries [26]. With the increasing spread of mobile radio and internet, the communication barriers between the economic centres have largely ceased, though this affects some western parts of China only in part [11]. China's research environment is changing and the quality of market research is improving. More and better information is available [5, 14, 26], though challenges in producing data in China still arise. These are related to the implementation of primary research in China, as well as the identification and analysis of secondary sources.

3. Secondary data availability, quality and validity

"An identifying and analysing secondary data source is more of an art than a science." [16] As China is a growing economy, the identification and analysis of secondary sources is difficult yet critical in terms of the availability and reliability of information. A comparative approach of diverse sources seems most appropriate in order to maximise usefulness.

In the past, the *availability of secondary data* in China, was limited and it was hard to get hold of accurate and relevant market research information. Whereas in Western countries a wide variety of market intelligence is provided through industry associations or government agencies, in China less information is published [23]. But, during the last years, this situation has improved and more industries within China have at least one association providing information on industry activities. Usually, these associations are closely related to the government [12]. Harrison (2006) states: *"For industry statistics and details of regulations, it is doubtful that any country makes more information available than China does."* [9].

Historically collecting adequate data in China has not been facilitated by economic reforms. Before the reforms were introduced in the late 1970s, agricultural production was divided into communes. For these small production units, it was easy to collect the necessary data. The data was then passed through the ranks of the communist regime and collected at the highest level statistical bureau. However, with decollectivisation the rural economy became divided into much smaller segments. Additionally, the number of private enterprises and the number of self-employed workers increased. Services also entered the production structure. Thus, collecting adequate data became much more complex in the 1980s. China's National Bureau of Statistics (NBS) had to adjust to these changes, but only managed to do so gradually. Since opening the economy to the rest of the world in 1978, a lot of progress has been made in collecting data. The quality of Chinese data has improved significantly. Data falsification has been reduced, variables are more consistently defined and data is evaluated by a greater number of better-trained personnel [12]. Nowadays most indus-

tries within China have at least one association providing information on industries activities. These associations are closely related to the government [9].

It is hard to get hold of market data. Access to such information is complicated by language issues, making desk research into Chinese markets a difficult task for western companies. Increasingly however, information is provided in English or other European languages [10].

Data quality and reliability secondary sources need to be analysed critically as *"...secondary information [...] is often old, questionable, or inaccurate..."* [16] Whether data is attained from the government itself, from research companies or from other organisations, much of it is actually governmental in origin. This means that secondary information is often compromised by a need to rely heavily on data that are reported by regional and local authorities. On a yearly basis, the National Bureau of Statistics (NBS) publishes the Statistical Yearbook of China. This is an important secondary source. Each province has its own Statistical Yearbook which does not necessarily contain the same information as the Yearbook of China. The yearbook figures are very often not up-to-date. And because of political pressures to inflate performance, it is widely argued that most of the Chinese official statistics are inaccurate and figures are manipulated to the favour of provincial authorities [16, 22, 23].

4. Primary research in the context of regional disparities, urbanisation and the challenge of data quality

"Primary research is typically the most extensive, reliable, useful, time consuming, and costly. Though this is true anywhere in the world, it is especially true in China. Data that comes through primary research in China can be valuable, but it can also be incomplete, misleading or even false." [16]

This is caused by *cultural differences* as well as the geographic scale, *size and diversity of the Chinese markets* (with about 70 regions, 56 ethnical groups and more than 80 languages, the Chinese market is much more complex than the European market). It results in challenges of research capabilities and techniques. Because of disparities in economic development, purchasing power and cultural factors both between and within regions, attitudes and patterns of behaviour can vary sharply across mainland China and lead to differences in answers and in the interpretation of responses [22]. Knowing and understanding these differences will facilitate the research work [18].

Interviews are a good example of how to gain authentic information on the Chinese market [23]. But unlike western countries, company representatives are often hesitant to speak negatively of themselves or positively of their business competitors. Hence, interviewers must read between the lines and cross-check as much as possible (for example, to ask the same question two ways at different points in the interview). It is advisable to use mainland Chinese interviewers for business research, as their sensitivity to cultural specifics enables them to communicate more effectively [16].

A great problem in conducting research in China is the *language* [26]. The language issue is compounded by the existence of various dialects that are somewhat similar but exist as separate entities. In terms of the script, different dialects are exactly the same, but the phonetic usage as well as the accent could affect the usage. Chinese characters can not simply be translated with a dictionary; moreover a native speaker should translate the words in consideration of the cultural traditions [14, 17, 18]. These differences could be approached by targeted primary research that is conducted differently for each region, for example with local research agencies or partners.

Besides cultural differences, country size and diversity, *urbanisation* is a special case in China [20]. Conducting research is easier in countries with a higher percentage of people living in urban areas. A higher degree of urbanization means that even if there are no good lists for sampling, the respondents can be contacted through other instruments. In economic theory, high growth rates and high urbanisation rates go hand in hand [5]. However, the experience in China has been different. Although the country has been continuously boasting high growth rates in 2005, the urban population only made up 43 per cent of the population [2]. Especially outside China's big cities, the *level of infrastructure* makes it hard to identify and select representative samples for survey research. Reliable and comprehensive lists that could form the basis for sampling frames are often not available and even when good sampling frames can be delineated, it is often necessary to obtain permission from the relevant authorities before collecting data [22]. On the other hand, the need for data from rural areas is questionable, especially in B2C research. China shows an extreme inequality in income distribution. Besides overall inequality in general, the differences between rural and urban areas in particular should be considered when collecting market research data. The urban areas are likely to reach income (and consumption) levels comparable to developed countries, the widespread income distribution remaining in urban areas. On the other hand, the rural areas of China are still at the level of a developing country, with average incomes lower than 1$ per day and consumption levels similarly low [3, 24]. Therefore, depending upon the aim of the research, a separation of approaches may be necessary between rural and urban areas.

5. Conclusion

In recent years, China's economy has undergone significant changes and continues to grow. It follows therefore, that China's research environment is also changing. The quality of market research is improving as more information is available. However, market research in China is dominated by dynamic and rapidly changing country specifics including language and culture. This leads to challenges in obtaining reliable, accurate, and up-to-date information on market conditions in China at micro and macro

levels. Primary data collection and secondary research both have a number of advantages and limitations in China, particularly regarding costs, availability, reliability and appropriateness.

An important step for foreign companies wishing to effectively research projects in China is to examine the challenges of doing so. Firms should identify key regions of China and focus their research efforts on these areas. Moreover, they should choose partners for their market research who are familiar with the Chinese culture and ideally understand both the western and the Chinese business environments.

References

[1] BAI, F.; PING, G. (2004): *Helping the Clients Succeed in China's B2B Market,* ESOMAR Asia Pacific Conference, Shanghai 2004.
[2] BEIJING RUNDSCHAU (2008): *China erlebt schnelle Urbanisierung* (01.04.2008), Beijing, Retrieved August, 2008, from: http://www.bjrundschau.com/nachrichten/txt/2008¬04/01/content_108401.htm
[3] BOROOAHA, V.K.; GUSTAFSSONB, B.; LIC, S. (2006): *China and India: Income Inequality and Poverty North and South of the Himalayas,* Journal of Asian Economics, Vol. 17, No. 5, pp. 797-817.
[4] BROCK, S. E. (1989): *Marketing Research in Asia: Problems,* Opportunities, and Lessons, Marketing Research, 9/1989, pp. 44–51.
[5] CRAIG, C.S.; DOUGLAS, S.P. (2005a): *International Marketing Research*, 3rd. edition, Chichester 2005.
[6] DATAMONITOR (Ed.) (2004): *Market Research in China,* Industry Profil, Retrieved June, 2008, from: http://www.marketresearch.com
[7] DIPPL-HENS, G.; ZENG, L. (2006): *Konstruktive Einblicke – B2B Marktforschung in China,* Research & Results, Vol. 2, 2006, pp. 28–29.
[8] EBEL, B. et al. (2007): *The Rise of the Dragon,* Hofer, M. B.; Ebel, B. (Ed.): Business Success in China, Berlin 2007.
[9] HARRISON, M. (2006): *Learning the Language*, Marketing research, winter 2006, pp. 11–16
[10] HARRISON, M. (2006a): *Business-to-Business Market Research in China*, whitepaper, Retrieved 26. 08. 2008 from http://www.b2binternational.com/library/whitepapers/whitepaper20.php
[11] HILGER, A. (2001): *Erfolgsfaktoren fur Internationalisierungsstrategien – Dargestellt am Beispiel des Engagements deutscher Unternehmen in der VR China,* Doctoral dissertation, Frankfurt amMain 2001.
[12] HOLZ, C. A. (2004): China's Statistical System in Transition: Challenges, Data Problems, and Institutional Innovations, Review of Income and Wealth, 50(3), 2002, pp 381-409.
[13] HUSSEN, H.-P.; MAURER, J. (2000): *Marktforschung VR China/ Hongkong/ SVZ,* Bundesagentur fur Außenhandelsinformationen (ed.), Koln, 2002.
[14] KUMAR, V. (Ed.) (2000): *International Marketing Research*, Upper Saddle River, New Jersey 2000.
[15] LIEBERTHAL, K.; LIEBERTHAL, G. (2004): *The Great Transition*, Harvard Business School Press: Harvard Business Review on Doing Business in China, Boston, 2004.
[16] OLIVER, C.; COULTER, J. E. (2004): *China Market Research Strategies,* China Business Review, May-June 2004, pp. 54–59.
[17] ROTHER, K. (1991): *Das internationale Geschaft: Ziele*, Marktforschung, Strategien, Marketing, Munchen 1991.
[18] SHENG, T. (2004): *Understanding China – An automotive bamboo shoot,* Proc. in ESOMAR Conference in Automotive Marketing 2004, Lausanne, 2004.
[19] SHENKAR, O. (2007): *Chinas Jahrhundert*, Munchen 2007.
[20] SMALL, K. A.: *Chinese Urban Development: Introduction,* Retrieved August, 2008, from: http://www.socsci.uci.edu/˜ksmall/chineseurban.pdf
[21] TRINH, T. (2004): *Foreign Direct Investment in China – good prospects for German companies?* China Special, Deutsche Bank Research, Frankfurt 2004, Retrieved June, 2007, fromhttp://www.dbresearch.com
[22] WALTERS, P.; SAMIEE, S. (2003): *Marketing Strategy in Emerging Markets: The Case of China,* Journal of International Marketing, Vol. 11, 1/2003, pp. 97-106.
[23] WOLFF, B. (2007): *Market Research as a Module in Market Strategies in China,* Hofer, M. B.; Ebel, B. (Ed.): Business Success in China, Berlin 2007, pp. 151–167.
[24] WU, X.; PERLOFF, J. M. (2005): *China's Income Distribution, 1985-2001*; Retrieved August, 2008, from: are.berkeley.edu/˜perloff/PDF/china.pdf
[25] YIXING, Z.; MA, L.J.C. (2003): *China's Urbanization Levels: Reconstructing a Baseline from the Fifth Population Census,* The China Quarterly, 173, 2003, pp. 176–196.
[26] ZABE-BRECHTEL, C. (2005): *Marktforschung, Scharrer,* B.; Neeff, U. (Eds.): So kommen Sie nach China – Der Wirtschaftswegweiser fur den Mittelstand, Munchen 2005.
[27] http://www.cmra.org.cu

Gerhard Braunmiller – Peter Horbaj – Natalia Jasminska *

GEOTHERMAL ENERGY AND POWER GENERATION IN GERMANY

The EU is the world's largest energy importer, relying on imports for 50 % of its energy needs. With an energy demand forecast likely to grow by 1–2 % a year, that figure will over the coming 20–30 years rise to 70 %.

The Geothermie is an inexhaustible energy source. With the supplies, which are stored in our planet, in principle the world-wide power requirement could be covered. The Geothermie, or terrestrial heat, is the warmth stored in the upper (accessible) part of the earth's crust. It covers the energy, as far as it can be extracted and used, stored in the earth, and ranks among the regenerative energies. It can be used both directly, approximately for heating and cooling in the heating market, and for the production by electric current or in a force heat coupling.

Production of heat using geothermal energy can be obtained in two very distinct ways. The first consists of directly exploiting subterranean water tables whose temperatures are included between 30 °C and 150 °C (so-called medium and low temperature applications). The second makes use of geothermal heat pumps that come under the heading of so-called very low temperature applications.

1. Introduction

The EU is the world's largest energy importer, relying on imports for 50 % of its energy needs. With an energy demand forecast likely to grow 1–2 % a year, this figure will rise within the coming 20–30 years up to 70 %. Yet Europe's energy needs are growing relatively slow in comparison to other parts of the world. Therefore it has to compete increasingly for energy resources. Climate change has also put renewable energy on the agenda and Europe is investing in renewable energy sources.

The total installed capacity of worldwide geothermal power plant from 1975 up to end of 2007 (estimated) is given in Table 1.

Installed capacity from worldwide geothermal power plant — Table 1

Year	Installed Capacity (MWe)
1975	1 300
1980	3 887
1985	4 764
1990	5 832
1995	6 833
2000	7 972
2005	8 933
2007	9 732
2010	10 993

Binary plant technology is playing a very important role at the modern geothermal electricity market. The economics of electricity production are influenced by the drilling costs and resource development (typical quota is 30 % for reservoir and 70 % plant); the productivity of electricity per well is a function of reservoir fluid thermodynamic characteristics (phase and temperature), and the higher the energy content of the reservoir fluid, the lesser is the number of required wells.

Geothermal Energy provides approximately 0.4 % of the world's global power generation, with a long term stable growth rate of 5 %. At present the largest markets are in the USA, the Philippines, Mexico, Indonesia, Italy and Iceland [1].

Table 2 Largest markets for geothermal power generation. We see that Germany is far behind this capacity due to different geo-

Largest markets for geothermal power generation — Table 2

Country	Installed Capacity (MWe)
USA	2 690
PHILIPPINES	1 970
INDONESIA	970
MEXICO	950
ITALY	810
ICELAND	420
GERMANY	8.9

* **Gerhard Braunmiller[1], Peter Horbaj[2], Natalia Jasminska[2]**
[1] Miesbach, Germany, E-mail: g.braunmiller@eb-ing.com
[2] Faculty of Mechanical Engineering, Technical University of Kosice, Slovakia

logical circumstances. Future developments are limited to certain areas worldwide, particularly under current technologies. Research and Development is required to develop potential for the other areas [2].

2. Present Technology for geothermal electricity generation

For generating electricity a direct usage of steam would seem to bet he thing to do with hydrothermal heat – and dry steam deposit with temperatures over 150 °C. One of the first plants in this field wwas put into operation in Italy at the beginning of the last century. Experience in commercial operations has been gained worldwide for approximately 40 years. If the enthalpy content of thermal water is too low for fluid to relax directly in the turbine, systems with secondary cycles will be used. The soil heat will be transferred via one or several heat exchanger into a closed power station process. Such systems are also used if the thermal fluid has an extraordinary high quantity of non-condensable gases construction and operation of the turbine would require technically complex solutions that are even more costly than the usage of secondary fluids or if the thermal fluid is very aggressive, i.e. strong mineralisation or high quantity of hydrogen sulphide. The heat source is cooled down noticabley during the heat transmission to the secondary cycle. Whereas the water depression will probably undergo only a small temperature increase during heat transmission from the power station processs [3].

2. Technology Systems for low enthalpie power generation

In principal, two systems are available for the low enthalpy power generation. Since the 1930s the Organic Rankine Cycle (ORC) has been used in different geothermal power stations. In the 70s, Alexander Kalina developed a new heat exchange technique to produce vapor at a low temperature level. In the so called Kalina cycle a mixture of ammonia and water is used to generate a vapor cycle at low level temperatures around 100 °C as a power source for turbines. It is expected to gain an increase of efficiency with this binary system in comparison to the ORC cycle that may be up to 25 %. The reason for this supposition is the boiling of binary ammonia – water mixture at a variable temperature unlike pure water or other fluids which boil at a constant temperature. Variable temperature of boiling permits the working fluid to maintain a temperature closer to that of hot combustion gases in the boiler, thus, improving the exergy efficiency, a fact which has been well known among engineers. The first European geothermal power plant with Kalina technology with 2 [MWel] () was installed in 2002 in Husavik, Iceland [1].

2.1 ORC-Process

Fig. 1 *ORC-Process* (**O**rganic – **R**ankine – **C**ycle) shows a schematic structure of the simple geothermal driven ORC. Thermal water is brought out of the production well to the power station through a feed pump. There it sends heat through a vaporizator and preheater to the equipment before it is conducted back into the subsoil through the injection well. In the secondary cycle – the ORC – the equipment is running through the preheater and vaporizator after a pressure increase by the feeding pump. The steam relaxes within the turbines. Organic – Rankine – Cycle has () been installed and operated for more than 20 years worldwide. The turbine power can reach from a few hundred kW up to more than five MW. In Germany, only few plants of this type are () operating. One of them is the geothermal driven power station in Neustadt-Glewe, Mecklenburg – Vorpommern that was first put into service in November 2003 [1 and 6].

2.2 Kalina-Process

In principle, the Kalina cycle (Fig. 2) corresponds to a Clausius – Rankine – Process with a high degree of internal heat recovery as well as additional destilation units. The union of the internal heat transmitter and the addition or reduction of destilation units allows good adjustment to a wider temperature range of possible heat sources. One of these systems was realised in Husavik, Island. This system is described in [4].

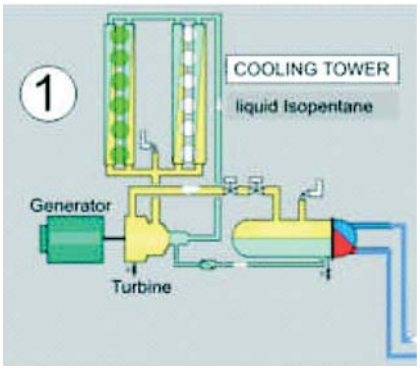

Fig. 1 ORC - Process

The geothermal heat is transferred to the main dissolving that is preheated in high temperature (High Temperature, HT-Rec()uperator) and low temperature heat recovery (Low Temperature, LT-Rec()uperator). Ammonia – rich steam and ammonia – poor dissolving are divided in a sepearator. The ammonia – poor dissolving is transferred directly to the HT-Rec()uperator where it heats the main dissolving. The steam relaxes within the turbine and drives the generator. Afterwards both substances are united again in the mixer.

2.3 Pros and cons of the process

()Comparing() both processes for thermal water temperatures from 100 °C to 200 °C and considering air cooling and fresh water cooling it can be said that Kalina plants are superior in the

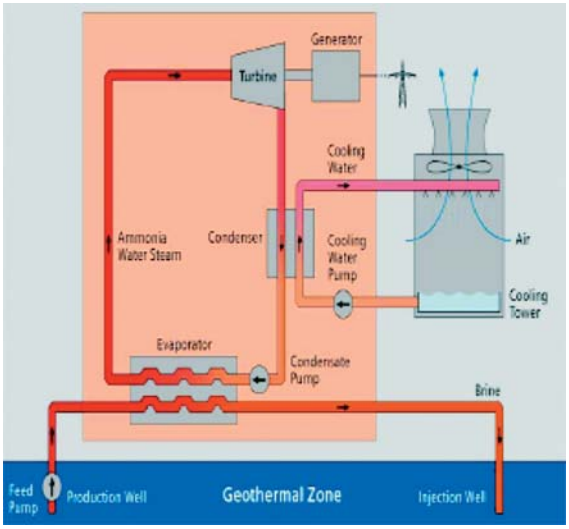

Fig. 2 Kalina-Process

lower temperature range, especially with air cooling, whereas ORC plants reach higher mains within the higher temperature range. Kalina plants do not extract () as much heat from thermal water as ORC plants do, but they convert this heat with a much higher thermal effectivenesss into electric energy. In contrast to ORC plants, with Kalina plants the point of maximum efficiency changes with the temperature increase of the heat source to a higher return temperature of thermal water [5].

Consequently, with thermal water temperature of 150 °C, the effectiveness of cooling is a lot lower in Kalina plants than it is in ORC plants. Remedy could be found by modifying the process. On the other hand, it is the little cooling that makes further usage of thermal water possible. It can be used for combined heat and power stations [7].

Contrastingly, ORC plants suffer from this low thermal effectiveness that leads to high energy needs for the process, especially with cooling. Estimated cost of investments depends on temperature and velocity of flow of geothermal medium, first of all [8].

Summary

For geothermal electricity production, the highest concentration of resource on the European continent is located in Italy, Iceland and Turkey; the present exploited value is only 0.3 % of the whole renewable market. The possibilities for geothermal energy to expand its penetration in Europe is mainly from the Enhanced Geothermal System (EGS); whereas the drilling technology is already in a mature stage, and efforts can only be done to reduce the drilling costs. The stimulation technologies are still in the pilot stage [9].

There are many geothermal prospects with high temperature, but they either lack fluid in the formation or the rock permeability is too low for permitting fluid circulation. These systems can be enhanced by engineering the reservoir through stimulation activities: acidizing and hydraulic fracturing. Due to the development of these technologies a huge geothermal potential will be available.

We should consider the new binary plants of Austria and Germany, proving the possibility of producing some geothermal electricity also from low temperature resources as very good and positive signals.

The present worldwide installed capacity of 9.7 GWel will increase up to 11 GWel in 2010. It has medium investment costs, depending on resource quality (temperature, fluid chemistry and thermodynamics phase, well productivity,...), ranging approximately from 2 to 4.5 /MW, and with very attractive generation costs, from 40 to 100 /MWh. It is a resource suitable for base load power. It can be considered as broadly cost-competitive, despite its relatively high capital costs for the development of the geothermal field (resource evaluation, mining risk, drilling and piping) for its very high availability and the stability of energy production. For the next generation it is expected to see the implementation of the Enhanced Geothermal System production and an intensive increase of low-to-medium temperature applications through binary cycle and cascade utilizations.

References

[1] RUGGERO, B.: *World Geothermal Generation in 2007*, Proc. of European Geothermal Congress, 2007.
[2] BUONASORTE, G. et al.: *Geothermal Development in Italy: From Present to Future,* Proc. of European Geothermal Congress, Unterhaching, Germany, 2007.
[3] KNAPEK, E., KITTL, G.: *Unterhaching Power Plant and Overall System,* Proc. of European Geothermal Congress, 2007.
[4] KALINA, A.: *ASME Journal of Engineering for power*, 4/1984.
[5] KOHLER, S.: *Geothermisch Angetriebene Dampfkraft Prozesse,* Dissertation, Fakultat III – Prozesswissenschafen der Technischen Universitat Berlin, 2005.
[6] PERNECKER, G.: *Low enthalpy Power Generation with ORC - Turbogenerator*, The Altheim Project, Upper Austria, GEO – Heat Center, Bulletin, 1/2003.
[7] RYBAR, P., RYBAR, R., TAUS, P.: *Alternatively Power Sources (in Slovak)*, TU FBERG Kosice, 2001, p. 121.
[8] JANDACKA, J.; MALCHO, M.; MIKULIK, M.: *Technologies for Development and Energy Exploitation of Biomass (in Slovak)*, ES ZU Zilina, 2007, p. 222.
[9] BRAUNMILLER, G., HORBAJ, P.: *Comparison Germany-Slovakia Utilisation Geothermal Energy*, Acta Mechanica Slovaca, 4-D/2007, pp. 523–528.

COMMUNICATIONS – Scientific Letters of the University of Zilina
Writer's Guidelines

1. Submissions for publication must be unpublished and not be a multiple submission.
2. Manuscripts written **in English language** must include **abstract** also written in English. The submission should not exceed **10 pages** with figures and tables (format A4, Times Roman size 12). The **abstract** should not exceed 10 lines.
3. Submissions should be sent: **by e-mail** (as attachment in application MS WORD) to one of the following addresses: *komunikacie@uniza.sk* or *holesa@uniza.sk* or *vrablova@uniza.sk* or *polednak@fsi.uniza.sk* **with a hard copy** (to be assessed by the editorial board) **or on a CD** with a hard copy to the following address: Zilinska univerzita, OVaV, Univerzitná 1, SK-010 26 Zilina, Slovakia.
4. Abbreviations, which are not common, must be used in full when mentioned for the first time.
5. Figures, graphs and diagrams, if not processed by Microsoft WORD, must be sent in electronic form (as GIF, JPG, TIFF, BMP files) or drawn in contrast on white paper, one copy enclosed. Photographs for publication must be either contrastive or on a slide.
6. References are to be marked either in the text or as footnotes numbered respectively. Numbers must be in square brackets. The list of references should follow the paper (according to **ISO 690**).
7. The author's exact **mailing address of the organisation where the author works, full names, e-mail address or fax or telephone number,** must be enclosed.
8. The editorial board will assess the submission in its following session. In the case that the article is accepted for future volumes, the board submits the manuscript to the editors for review and language correction. After reviewing and incorporating the editor's remarks, the final draft (before printing) will be sent to authors for final review and adjustment.
9. The deadlines for submissions are as follows: September 30, December 31, March 31 and June 30.

COMMUNICATIONS

SCIENTIFIC LETTERS OF THE UNIVERSITY OF ZILINA
VOLUME 11

Address of the editorial office:
Zilinská univerzita
Office for Science and Research
(OVaV)
Univerzitna 1
SK 010 26 Zilina
Slovakia
E-mail: komunikacie@nic.uniza.sk,
polednak@fsi.uniza.sk

Each paper was reviewed by two reviewers.

Journal is excerpted in Compendex

It is published by the University of Zilina in
EDIS – Publishing Institution of Zilina University
Registered No: 1989/98
ISSN 1335-4205

Published quarterly

Single issues of the journal can be found on:
http://www.uniza.sk/komunikacie